

AD-A122 143

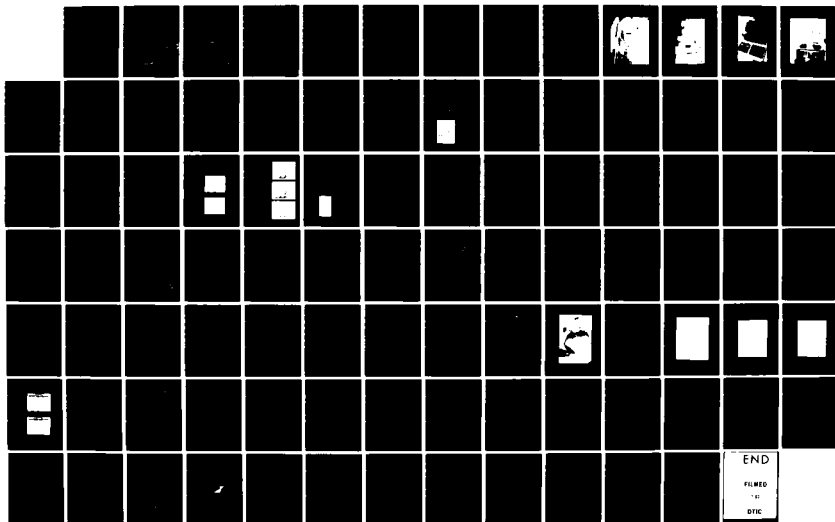
HIGH EFFICIENCY FREE ELECTRON LASER(U) TRW DEFENSE AND  
SPACE SYSTEMS GROUP REDONDO BEACH CA G R NEIL ET AL.  
31 JUL 82 N00014-80-C-0580

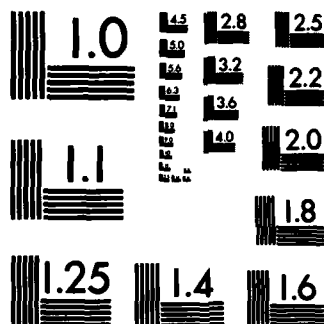
1/1

UNCLASSIFIED

F/G 20/5

NL





MICROCOPY RESOLUTION TEST CHART  
NATIONAL BUREAU OF STANDARDS-1963-A

# TRW

ADA 122143

DTIC

DEC 7 1982

H

DTIC FILE COPY

DEFENSE STAFF  
Approved for public release  
Distribution Unlimited

TDW

DEFENSE

One Space Park

17

FINAL REPORT  
HIGH EFFICIENCY  
FREE ELECTRON LASER

G.R. Neil, H. Boehmer, M.Z. Caponi, J. Edighoffer,  
S. Fornaca, J. Munch, B. Saur, C. Shih

**TRW**

DEFENSE AND SPACE SYSTEMS GROUP  
ONE SPACE PARK REDONDO BEACH, CA 90278

CONTRACT NO. N00014-80-C-0580

For the Period Oct. 1, 1981 to July 31, 1982

SPONSORED BY: Office of Naval Research  
Branch Office  
1030 East Green Street  
Pasadena, CA 91006

DTIC  
DEC 7 1982  
H

DISTRIBUTION STATEMENT A  
Approved for public release:  
Distribution Unlimited

## CONTENTS

	Page
FORWARD	i
I. Executive Summary	1
II. System Description	3
III. Diagnostic Development	10
IV. Results	25
V. Theory	40
VI. Summary	50
Acknowledgement	52
References	53
Appendix I: Time Structure of the FEL Output	54
Appendix II: Definition of Gain and Power Out of the FEL	56
Appendix III: A Fully Time Resolved High Resolution Optical Fiber Profile Montior	58
Appendix IV: Emittance Measurement Technique	66
Appendix V: Accelerator Development	69

# FOREWARD

This work was performed under ONR Contract No. N00014-80-C-0580, administered by ONR, Pasadena Branch Office. The TRW FEL team would like to thank the Scientific Officer, Dr. R. Behringer, ONR, and Lt. Col. R. Benedict, DARPA, for their advice and encouragement.

Accession For	
NTIS SPAN	<input checked="" type="checkbox"/>
DTIC TAB	<input type="checkbox"/>
Unannounced	<input type="checkbox"/>
Justification <i>for</i>	
<i>FL-182 on file</i>	
By _____	
Distribution/ _____	
Availability Codes	
Dist	Avail and/or Special
<i>f</i>	



## I. EXECUTIVE SUMMARY

→ The results of an experimental program to investigate the free electron laser (FEL) are presented. The FEL system used was developed under a previous phase of this contract. It utilizes a 25 MeV linac operated by EG&G in Santa Barbara to produce amplification of 10.6 micron light from a high power CO<sub>2</sub> laser. The system operates at a pulse rate of 60 Hz.

At the commencement of this phase of the program, the TRW FEL had already demonstrated deceleration and trapping in agreement with theory. The uncertainties that remained were twofold: first, the emittance of the electron beam appeared to be influencing the trapping, suggesting that the emittance was larger than previously measured; second, it had not been demonstrated that the energy lost from the electrons had appeared in radiation (although this had been demonstrated for the low energy spread case of the constant wiggler<sup>1</sup>). Measurement of these quantities required the development of new diagnostics. The requirements on these diagnostics are not trivial: the emittance measurement system must be capable of responding quickly enough so that changes due to shifts in accelerator tuning do not affect the measurement. Moreover, the focusing system of the electron beam transport system should be altered as little as possible so that re-focusing of the electron beam into the wiggler system can be accomplished quickly.

A device to meet these requirements was developed based on an array of optical fibers. Cerenkov radiation from electrons striking the fibers converts the electron profile to an electrical signal in a photo detector. The array was used to measure electron density radial profile as a function of magnetic quadrupole focussing to determine the emittance of the electron beam. Use of this diagnostic uncovered large changes in the day to day emittance of the electron beam. The sensitivity of the FEL to changes in the emittance appeared to be large.

These effects were observed during single pass gain measurements that were performed on the system. The requirements on the gain diagnostics were even more severe than on the emittance diagnostic. The anticipated gain was on the order of 1%. To accurately measure a change that small is difficult enough but compounding the difficulty was the fact that

gain only appears during the 30 ps duration of the electron beam pulse. When averaged over the response time of the detector, the signal increase due to the FEL interaction was predicted to be .02%. An etalon system was developed to discriminate against the background signal. It was successful in rejecting the high power input while retaining the gain signal. The high repetition rate of the system allowed the use of signal averaging techniques to produce a threshold sensitivity of .3% peak gain. Small signal gain of the FEL with a constant wiggler was measured with this system to be 1.5%. Large signal gain with a tapered wiggler was found to be less than 3%.

→ The experimental results indicate that to the limits of the present sensitivity the FEL is behaving in accordance with theoretical models. This suggests that improving the current and emittance of FEL accelerators will have a profound effect on improving the performance of FELs. To this end accelerator development has been performed at the Boeing Aerospace Company linear accelerator. Effort has centered on designing critical accelerator system components to produce an electron beam which meets the stringent FEL requirements for high beam quality, high current, and a long, stable macropulse.



## II. SYSTEM DESCRIPTION

The experiments described below were performed on the system built during the previous phase of this contract. The apparatus is described briefly below. Further detail may be found in the references<sup>1</sup>. A schematic of the three main subsystems (linac, optical system, wiggler) is shown in Figure 1.

The electron beam source is the rf linear accelerator located at EG&G Santa Barbara Operations. It has an energy range of 1-30 MeV, with 25 MeV being the nominal operating point. Firing at a repetition rate of 60 Hz, the linac produces single beam pulses of 30 ps duration with a 1% full width at half maximum (FWHM) energy spread, 15 A peak current, and an emittance of  $4.3\pi$  mm mrad. The electron energy analyzer consists of a  $45^\circ$  analyzer magnet and an electron profile monitor. The linac is pictured in Figure 2 before the addition of the transverse electron transport system.

The optical system consists of a laser driver, beam propagation optics, and a spectrometer with a detector. The laser beam pulse of 20 MW peak power and 3 nsec FWHM is produced in a two stage CO<sub>2</sub> laser system using an electro-optical switch<sup>7</sup> for pulse-length control. The system is designed to run at high repetition rates to allow the use of signal averaging techniques.

Figure 3 shows the first stage injection laser with the Pockels cell switch. The mode-locked power oscillator is shown in Figure 4. Reflective optics were used to propagate the output beam to the FEL and fit the beam to the proper size, waist position, and polarization. Overlap of the electron and photon beams was assured by observing a colinear HeNe beam on fluorescent screens inserted into the beam line before and after the wiggler. Remote television cameras could simultaneously observe the HeNe beam and the electron beam striking the screen.

The tapered wiggler is constant in wavelength ( $\lambda_w = 3.56$  cm) but varies axially in field amplitude. It consists of a pair of linear arrays of SmCo<sub>5</sub> permanent magnets with the magnetization vectors oriented as shown in Figure 1. The field at the symmetry axis is given by  $B = A \cos(kz) \times \exp(-kh)$ ;  $k$  is the wiggler wave number equal to  $2\pi/\lambda_w$ ,  $h$  is the half-

# TRW TAPERED WIGGLER FEL EXPERIMENT

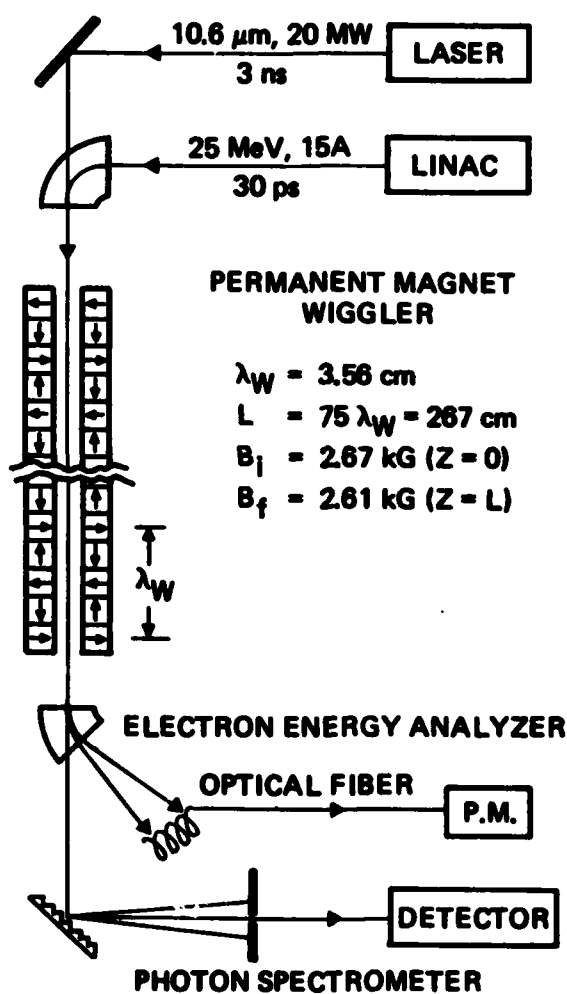


Figure 1. Schematic of the TRW Tapered Wiggler Free Electron Laser



Figure 2. EG&G 25 MeV Linac. Injector is at upper right, the accelerator cavities at center, rear, and injection to the FEL transport system takes place in the center, foreground.

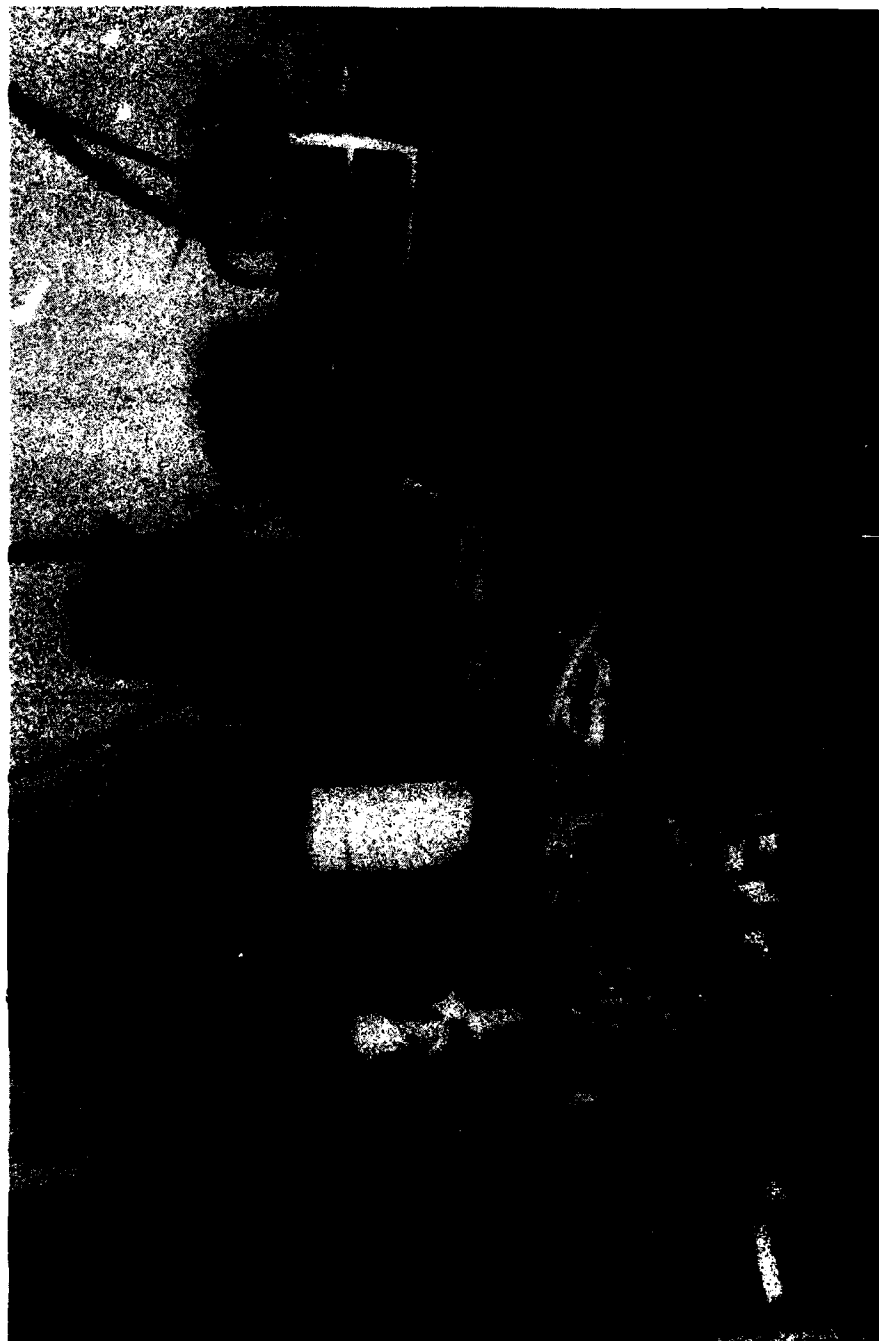


Figure 3. Quasi CW Injection Laser with Pockels cell for injection modelocking the power oscillator.



Figure 4. GenTec Power Oscillator



Figure 5. SmCo Magnet Adjustable Taper Wiggler System.

separation of the two magnet planes, and  $A$  is a factor that depends on the magnet material and geometrical factors. Variation of the field strength is accomplished by making  $h$  a function of  $z$ . Additional end tapers are necessary for unperturbed beam propagation. Figure 5 shows the wiggler mounted in position. A unique feature of the design is that adjustment of the taper to any desired value may be accomplished quickly and easily by insertion of shims between the supporting rods; this allows a taper change during a half hour of down time.

These three systems combine to form the FEL. An understanding of the operation of these system requires sensitive diagnostics. Several developed specifically for this program are described in the next section.

### III. DIAGNOSTIC DEVELOPMENT

The key to understanding free electron lasers and interpreting the results of the experiments is in quality diagnostics. The importance of good meaningful diagnostics can not be overstressed. The free electron laser has stringent requirements for the electron beam and has unique optical output properties, both of which require that good diagnostics be developed to observe and measure this parameter space. For the electron beam it is necessary to measure very accurately the energy, the energy spread, the emittance and position before and after the free electron laser interaction. The optical diagnostics fall into two classes: those which measure the spontaneous radiation and those which measure amplification of the injected laser pulse.

Three unique diagnostics have been developed to meet these requirements. A high resolution spectrometer was built that measures the complete electron energy distribution on each electron micropulse. A fast and accurate emittance measuring system was also designed and developed. An optical gain measurement system able to measure gain as low as .3% lasting 30 psec superimposed on a 3 nsec input pulse was built and tested. These and other diagnostics made the experimental program a success.

#### Electron Beam Diagnostics

The electron beam line (see Figure 6) had several diagnostics installed. A Faraday cup was used to measure the current from the linac. Since it has a very fast risetime it was used to set up the subharmonic buncher for the narrowest micropulse making sure there were no satellite pulses, i.e. pulses that fell into adjacent RF buckets. An adjustable collimator was used in the first  $90^\circ$  bend (where the energy dispersion is large) to select the energy spread to be allowed into the free electron laser system. It was set to allow a 1% energy spread into the system. Next, there was an insertable stopping block at the position of the dashed line in Figure 6. This was used to measure the amount of current that made it through the energy slits. Following this, the electron beam was transported through five quadrupole magnets to the



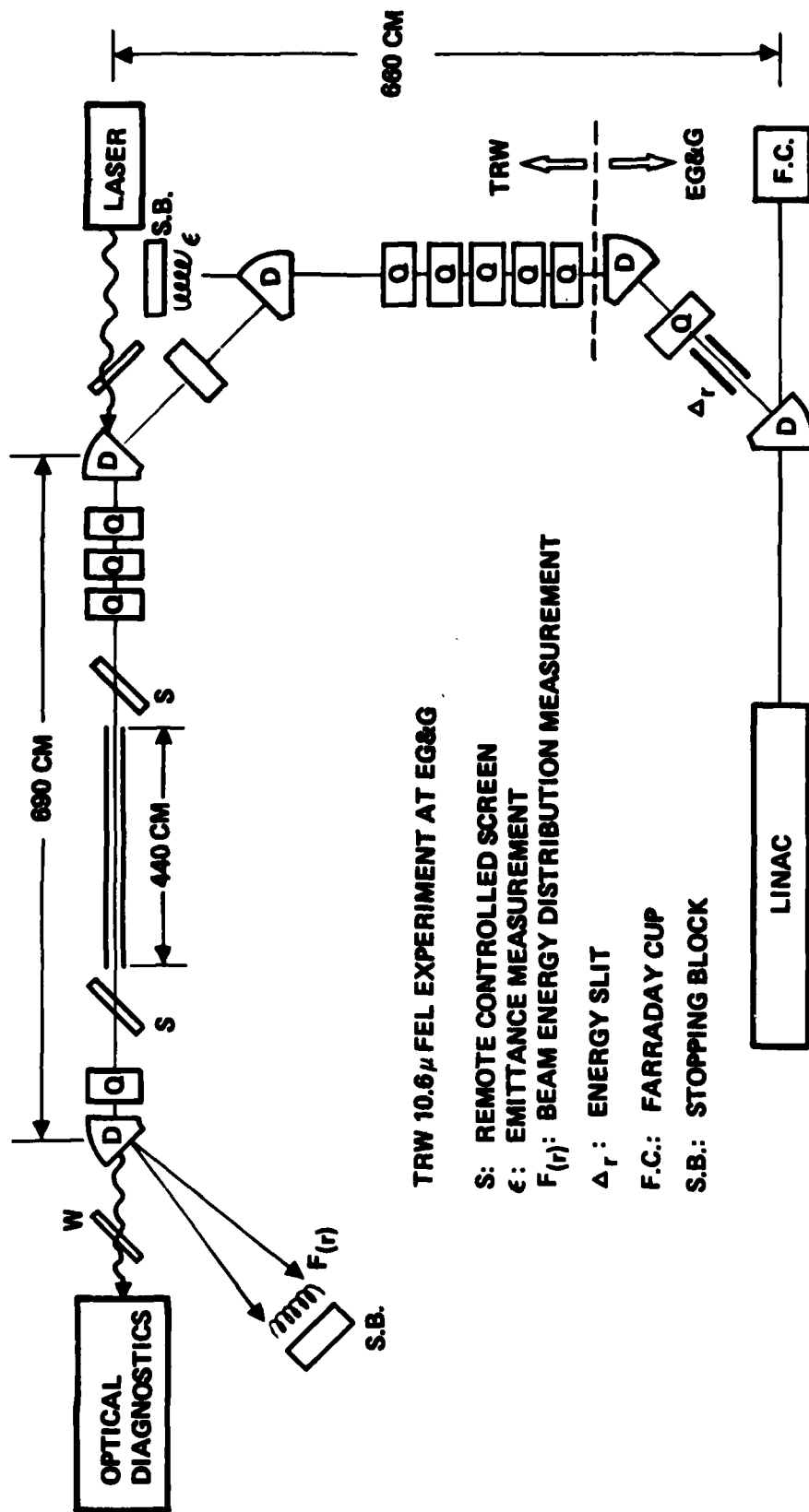


Figure 6. FEL Experimental Setup

second  $90^\circ$  bend. A straight through port on the first bending magnet allowed the current and the emittance at this point to be measured. The current was measured by a stopping block which captured the charge of the electron beam. The emittance was measured by varying the current on the last quadrupole of the five quadrupoles in the transport line and using a profile monitor made of a coil of optical fibers. This measurement will be discussed in detail below. The electron beam is then bent around the corner and focused into the wiggler system. Insertible fluorescent screens are used immediately before and after the wiggler to properly position and focus the electron beam. These screens are also used to align the  $\text{CO}_2$  laser through the system. After passing through the wiggler the electron beam is bent  $45^\circ$  to a profile monitor made of optical fibers to form a high resolution spectrometer. A stopping block at this point is used to measure the current through the wiggler.

The profile monitor used in the emittance and energy spectrometer consists of a novel application of optical fibers. This monitor was developed during the experimental program. The monitor consists of a single polysilicate optical fiber wound on a mandrill to form a ribbon of sixty tightly packed loops (see Figure 7). One section of the circumference of this ribbon is placed to intercept the electron beam with the rest of the ribbon bent out of the way. This section of the ribbon is oriented at the Cherenkov angle with respect to the electron beam. In this way, Cherenkov radiation produced by the passage of the electrons through the fibers is bunched. As the electron pulse is short compared to the optical transit time around the loop, the ribbon forms a delay line. Thus light from one side of the coil gets to the phototube before that from the other side. The instantaneous profile of the electron beam is converted to an oscilloscope trace. Appendix III gives a detailed description of this device.

By using this profile monitor in conjunction with a quadrupole magnet, a fast, reliable, and very accurate emittance measurement can be done (see Figure 8). The profile as a function of the current in the quadrupole is dependent on the emittance. From the shape of this function the emittance can be accurately inferred. This is based on electron transport assuming the electron beam is a Gaussian profile. This technique

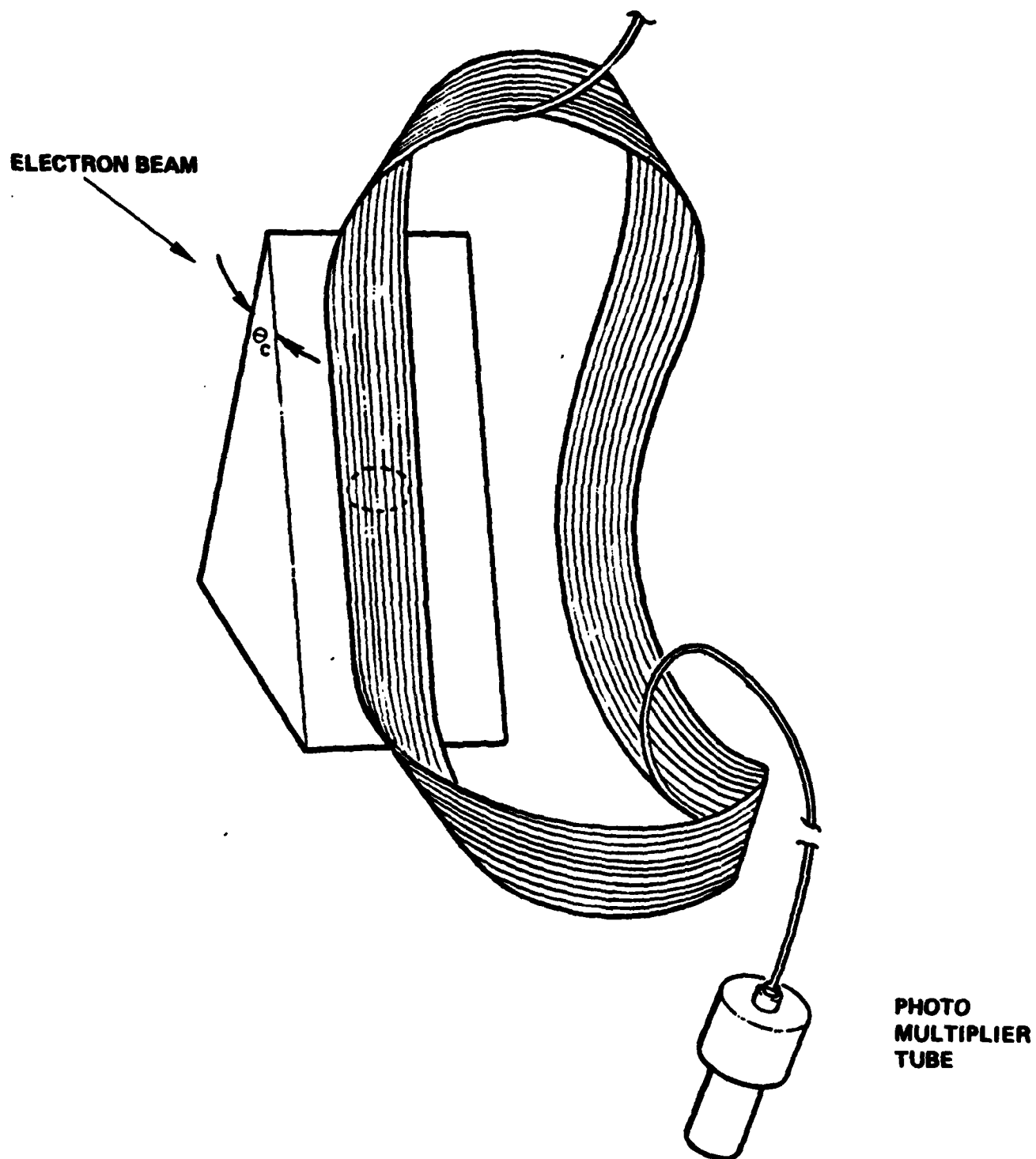


Figure 7. Optical Fiber Electron Profile Monitor

ON LINE BEAM EMITTANCE DIAGNOSTIC

BASED ON THEORY BY ROGER MILLER, SLAC.

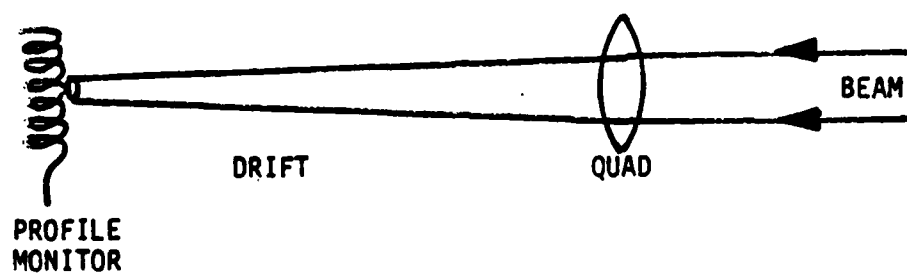


Figure 8. Schematic Representation of Emittance Diagnostic

was developed by Roger Miller at SLAC. Appendix IV has a detailed derivation of the applicable equations. This method requires that the profile be measured for at least three settings of the quadrupole magnet as three unknowns in the transport equation must be solved for. These are the emittance, the waist size and the position of the waist. More than three settings allow an error bar to be assigned to this measurement. To measure five or six profiles takes less than ten minutes, so that this measurement can be repeated as often as desired, allowing it to be used to tune the accelerator for good emittance.

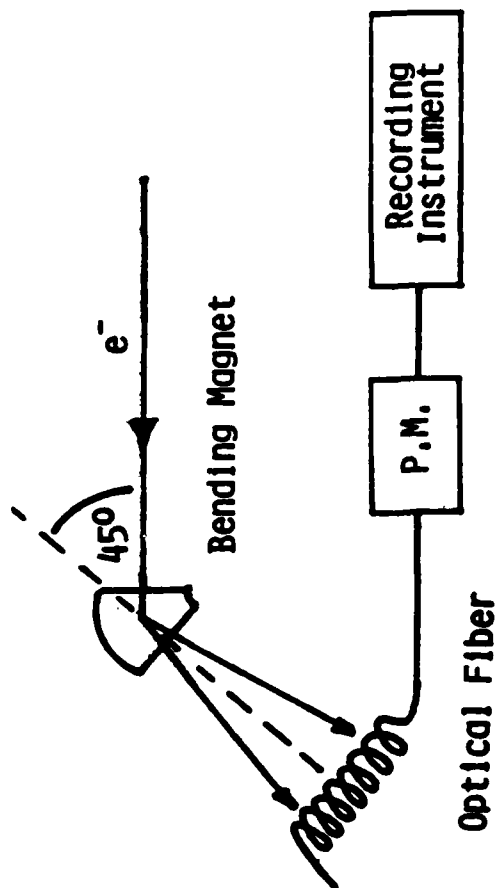
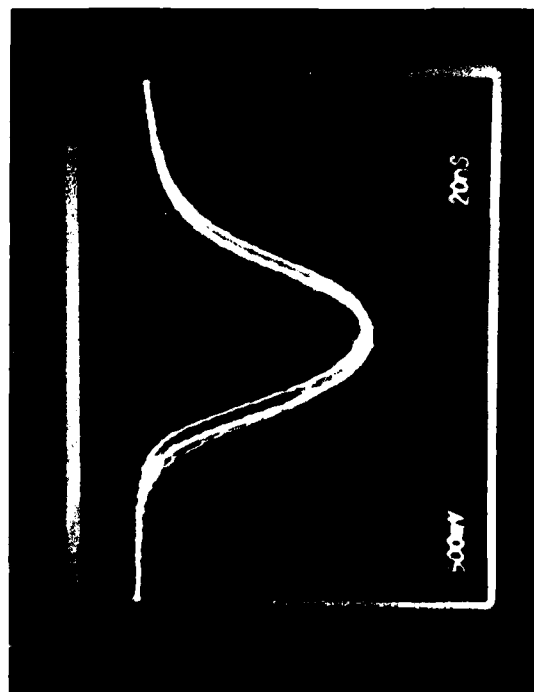
The optical fiber profile and position monitor in conjunction with a bending magnet forms a very accurate pulse resolved electron spectrometer (see Figure 9). In this case, the position at which the electron passes through the fiber is correlated with its energy. Changes in the electron energy of as little as .18% can be measured allowing a very accurate measure of the electrons energy exchange with the input CO<sub>2</sub> laser pulse.

These two novel electron beam diagnostics were developed and used very successfully during the experimental program giving significant improvement in the knowledge of the electron beam and its interaction in the free electron laser. The data obtained will be presented below following a discussion of the optical diagnostic system.

#### Optical Diagnostics

A major complication in measuring instantaneous optical gain arises from the fact that the gain occurs only for the duration of the electron beam micropulse, which because of the RF nature of electron accelerators is about 30 psec long. The unamplified CO<sub>2</sub> laser signal is 3 ns long, limited by the speed of the Pockel cell switch, forming an essentially CW (on the ps timescale) background (see Figure 10). To complicate matters even further, the fastest IR detectors have a rise time of around 300 psec which reduces the amplitude of the optical gain signal by a factor of 10 (see Figure 11). For these reasons, it was necessary to develop an optical gain measurement system which discriminates against the input laser pulse. Such a system was developed which could measure instantaneous optical gains as low as .3%.

LOW COST, HIGH RESOLUTION, SINGLE PULSE  
ELECTRON ENERGY ANALYZER



- RANGE:  $\Delta E/E = 4\%$       BEAM: 25 MEV
  - DISPERSION: 1% / 40 NS      1% ENERGY SLIT
  - RESOLUTION:
    - MAGNET 0.2%
    - FIBER < 0.08%
- RESULT: 0.75% FWHM

Figure 9. Electron Energy Analyzer

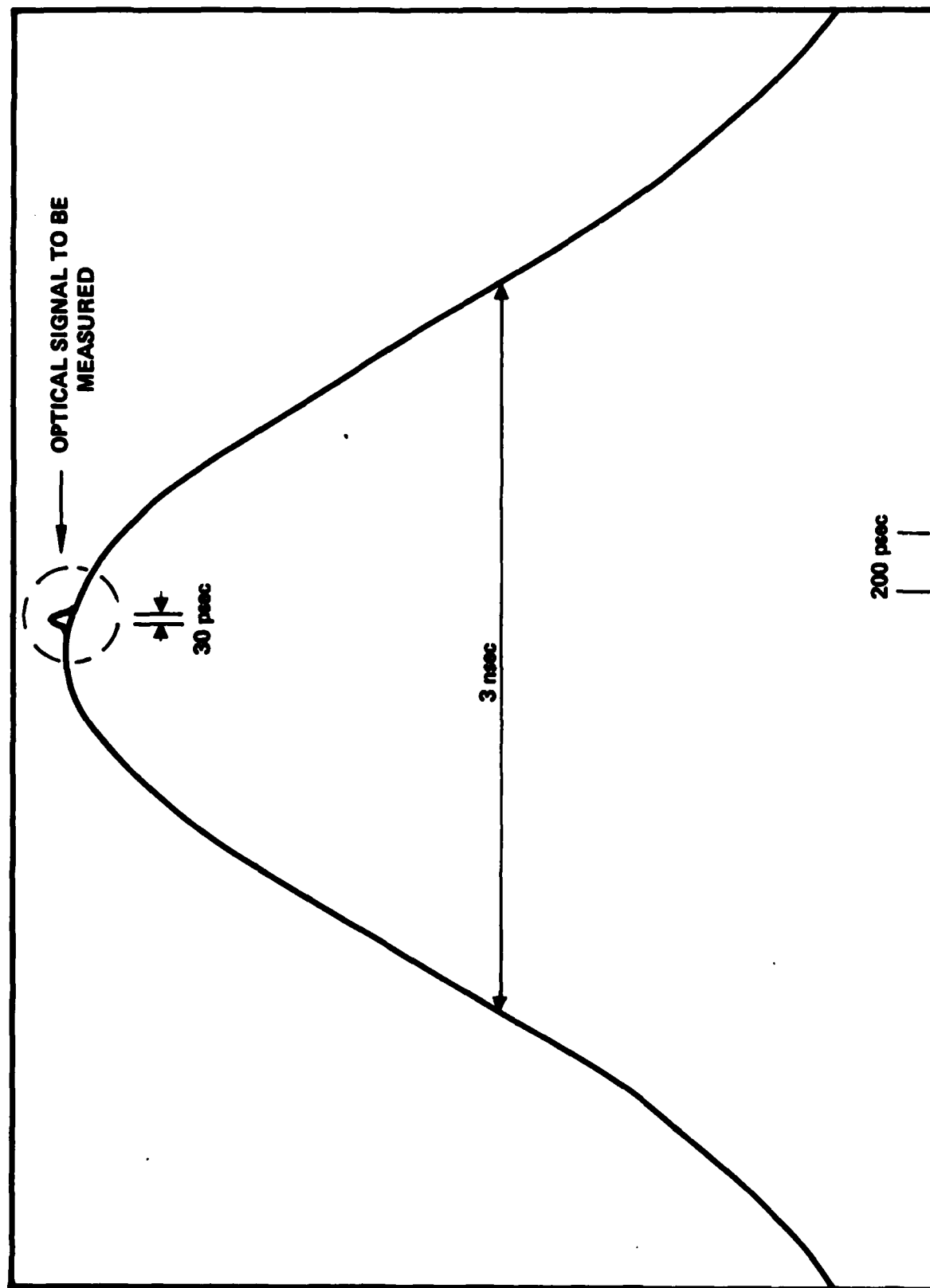


Figure 10. Representation of Gain Signal on Input Pulse

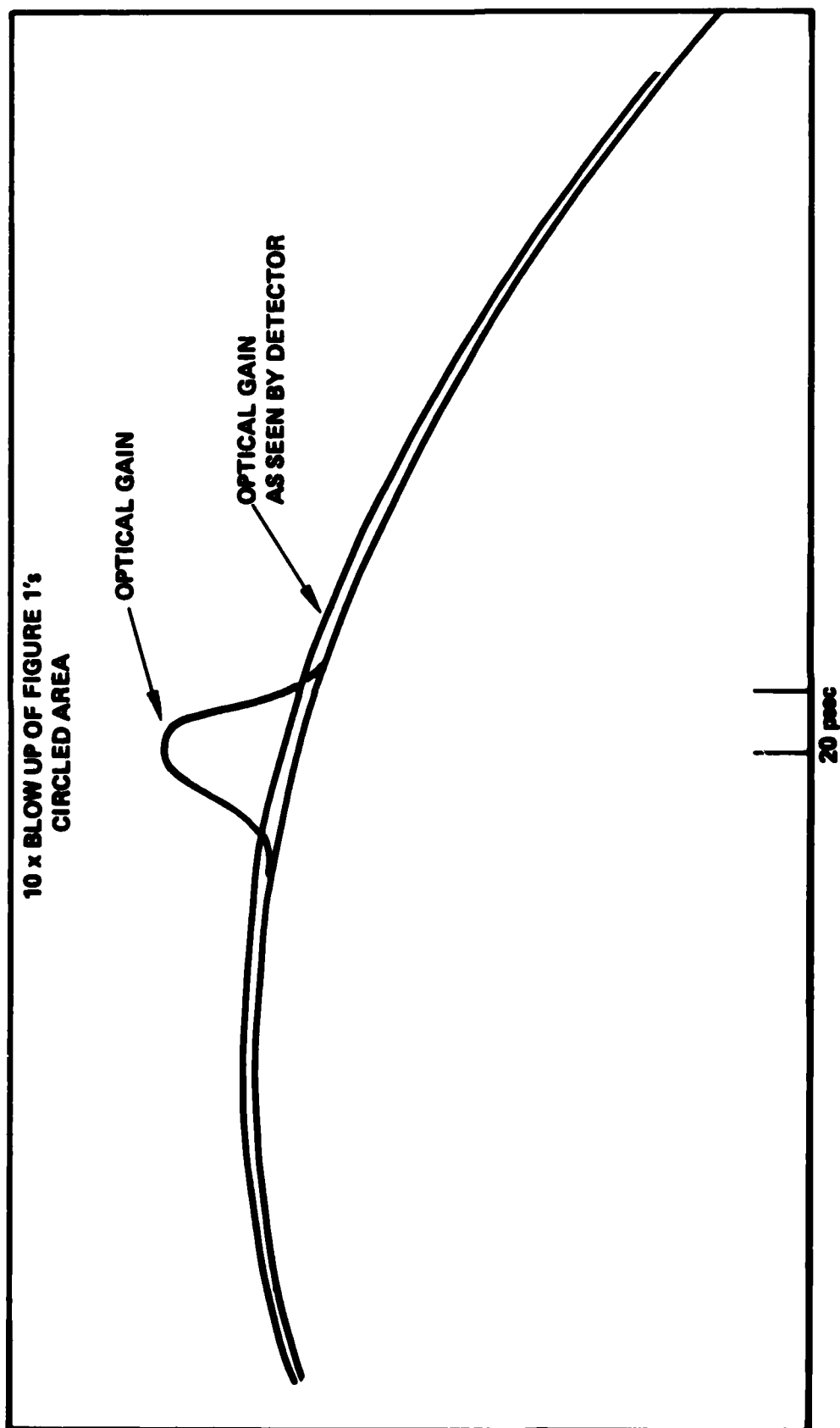


Figure 11. Enlargement of Representation of Gain Signal



First, though, it is useful to describe the optical gain system without input laser discrimination. A great deal of signal to noise enhancement can be done by taking advantage of the high repetition rate of the experiment (60 Hz) using signal averaging methods. This was done by sampling and holding the amplified laser signal from the fast detector. The sampling of the signal is done at a time corresponding to the peak of the spontaneous radiation pulse. This technique makes sure that the sampled signal was coincident with the electrons traveling through the wiggler. This signal was input into a lock-in amplifier and averaged over several hundred samples. To take advantage of the lock-in amplifier, the electron pulse was switched off every other pulse and the lock-in referenced at half the laser firing frequency; thus, the signal from the lock-in was the difference in gain with and without electrons so that background fluctuations are automatically averaged out. Using the same setup, but blocking the input laser light the spontaneous radiation could be measured and subtracted from the gain signal. The sampling window was 75 psec wide set to within 50 psec of the peak spontaneous radiation signal. A jitter of less than 50 psec between the laser signal and the spontaneous signal was observed. A detectability threshold equivalent to 1.5% instantaneous gain was measured with no input laser pulse discrimination. This was determined by replacing the detector signal with a calibrated pulse to simulate the input and the gain spike. The gain spike was attenuated until the lock-in reading was equal to the noise level. The optical gain predicted by the electron distribution measurements indicated the tapered wiggler had a gain of 1.7%.

Considerable effort was made to increase the sensitivity of the optical measurement by preferentially attenuating the unamplified laser signal. The discrimination of optical pulses relies on the fact that the pulse durations are drastically different for the optical gain signal and the input laser pulse; or equivalently, the bandwidth of the input laser is much less than the gain pulse.

If the laser pulse is much longer than the electron pulse, the optical gain signal is very close to the same width as the electron pulse (see Appendix I for detailed calculation). This means that the gain, the spontaneous radiation (both regular and enhanced due to bunching) and

the electron pulse have the same time structure.\*

The power emanating from the free electron laser consists of four terms (see Appendix II). The first term is the power of the input laser and has a long time structure. The other three terms are derived from radiation by the electrons, have a short time structure, and can be separated due to their different bandwidths. This was done by using a Fabry-Perot. It is essentially a notch filter which eliminates the narrow band input laser signal while passing most of the fast terms.

A number of methods were considered before settling on the Fabry-Perot for preferentially attenuating the unamplified laser signal by known amounts. One optical method commonly suggested for enhancing the sensitivity of the gain measurement is to rotate the polarization vector of the  $\text{CO}_2$  beam an angle  $\theta$  with respect to the gain axis of the free electron laser. As there is gain only for the component of the electric field along the gain axis, there is a rotation of the total field vector and this rotation is detected at the output by an analyzing polarizer oriented at  $90^\circ$  with respect to the input laser polarization. The problem is that this is a second order effect in gain. Therefore this does not measure gain but the gain can be inferred by making certain assumptions. What is measured is the third term mentioned in Appendix II. In practical terms, the extinction ratio of the polarizer must be greater than the reciprocal of the gain squared. To measure a 1% gain the extinction ratio would have had to be better than  $10^4$ , and still the gain must be inferred. With a practical polarizing system, the enhancement of this method was only a factor of 2. The lack of a dramatic increase in sensitivity, coupled with concern about the interpretation of the gain measurement led to the

---

\*Note that gain and enhanced spontaneous radiation cannot be separated by time or frequency filtering techniques, so that neither hot  $\text{CO}_2$  or Fabry-Perot techniques, can measure, by themselves enhanced spontaneous and not gain or visa versa. This can only be done by polarization effects.

abandonment of the polarization discrimination technique in favor of pulse length discrimination.

A low reflectivity Fabry-Perot interferometer can be used to discriminate against the slowly varying narrow bandwidth CO<sub>2</sub> laser input signal. The principle of this device is based on the interference of successive reflections between two parallel partially reflecting surfaces. Constructive interference of the slowly varying wave amplitude occurs when there is an integral number of optical wavelengths between the surfaces, so the reflected power is at a minimum. When the contributions of all the interfering waves are summed the resultant reflected power is

$$P_r(t) = P_0 \frac{R}{(1-R)^2} \left[ A f(t) - \tau \frac{df(t)}{dt} \right]^2 \quad (1)$$

with

$$P_{in}(t) = P_0 f^2(t).$$

R is the reflectivity of a surface, A is the net absorption of the beam in traversing the gap between the surfaces and  $\tau$  is the round trip time for the light.

On the other hand, if the duration of the pulse is less than  $\tau$  interference can not occur and the power reflects from each surface and the reflected power is

$$P_r = P_{in} (R + (1-R)^2 R + (1-R)^2 R^3 + (1-R)^2 R^5 + \dots)$$

where each term in the series is separated in time by  $\tau$ . The reflected power of the fast pulse is insensitive to large changes in the pulse length.

The device in its simplest form is a solid flat of uncoated ZnSe, approximately 3 mm thick, mounted on a rotating stage. The index of refraction of ZnSe at 10.6  $\mu\text{m}$  is 2.4, so for near-normal incidence  $R = 0.17$ . The bulk absorption is  $6 \times 10^{-4} \text{ cm}^{-1}$  and the round trip time is 48 ps. The power reflected from the fast pulse is independent of the angle of incidence

$$P_f = .29 P_{in}.$$

This power is reflected in a time short compared to the risetime of the detector and only first reflections from the front and rear surfaces contribute. As far as the fast pulse is concerned, the etalon is a 29% reflecting mirror. The reflected fraction of the slow pulse varied between 1/2 and the minimum, which can be evaluated using Eqn 1. A Gaussian slow pulse time profile with a distance between 1/e points equal to 3 ns has a reflectance of  $10^{-4}$  and a 500 ps wide region centered near the peak of the input pulse where the reflectance is less than  $10^{-5}$ .

The device is aligned by adjusting the orientation of the etalon until the transmission of the CO<sub>2</sub> laser signal is maximized; the reflected signal is minimized by making final angular adjustments of the order of a milliradian.

In practice, factors other than absorption (primarily surface parallelism of the solid etalon, but also flatness, surface quality) can increase the reflectance of the slow signal, but the reflectance of the fast signal is insensitive to all of this.

Figure 12 shows the optical setup used to measure the gain with the etalon as a pulse length filter. The light from the free electron laser is extracted from the high radiation environment through a shielding wall to the optical diagnostic setup. The light is collimated by a telescope before impinging on the etalon. The majority of the CO<sub>2</sub> laser pulse is transmitted through the etalon. The reflected signal off the etalon is focussed on a mercury teluride detector after reflecting off a grating. The grating is in the system, so the spectrum of the gain pulse could be measured, as well as the spectrum of the spontaneous radiation from the free electron laser. The electronic signal processing is the same as described earlier.

A more common two-plate Fabry-Perot system, consisting of two plates with AR coated outer surfaces and uncoated inner surfaces, could have been used to relax the parallelism requirement, but the limiting factor for the slow signal reflectivity is the AR coating on the first surface. Typically this reflectivity is about .3-.5% at 10.6  $\mu$ m. Thus, a solid etalon was chosen.

A ZnSe etalon was purchased to test this scheme. The etalon with the best surface parallelism (11 arc seconds) was selected from the manufacturer's stock; better parallelism is certainly achievable, but for testing purposes it was better to avoid the long lead time associated with the manufacture of a better etalon. The wedge angle was such that constructive interference criterion could not be met over the entire surface of the etalon; it was estimated that for a beam with 15 cm diameter the total power rejection of the slow signal would only be a factor of 30, although local portions of the beam would have much larger rejections. The predicted behavior of the etalon was verified with a dc CO<sub>2</sub> laser. The rejection over the full beam area was only 26, although the center portion of the beam had rejection in excess of 200.

The performance of the etalon not only bore out predictions sufficiently to warrant further interest, but was good enough to reduce the gain detection threshold to  $\sim .3\%$

The system developed to measure spontaneous emission is shown in Figure 12. The radiation, used for timing, alignment and energy calibration is collected by a exit mirror subtending from the FEL a half angle adjustable from .5 to 4 milliradians. The radiation thus collected exits the radiation cell by means of a shielded pipe and is focussed on a diffraction grating blazed for 10 microns. The dispersed spectrum is limited by a small aperture before landing on the HgCd<sub>2</sub>Te detector. The assembled system exhibited a resolution of better than .05 microns. Signal processing consisting of a high speed amplifier and a lockin unit at the linac pulse frequency was used to enhance the signal sensitivity. Peak power levels during the 30 ps pulse as low as 6 microwatts could be detected. Moreover a risetime of as short as 300 ps was observed through the fast amplifiers. The results of using the system will be discussed below.

# OPTICS FOR SPONTANEOUS SPECTRUM AND FEL GAIN MEASUREMENTS

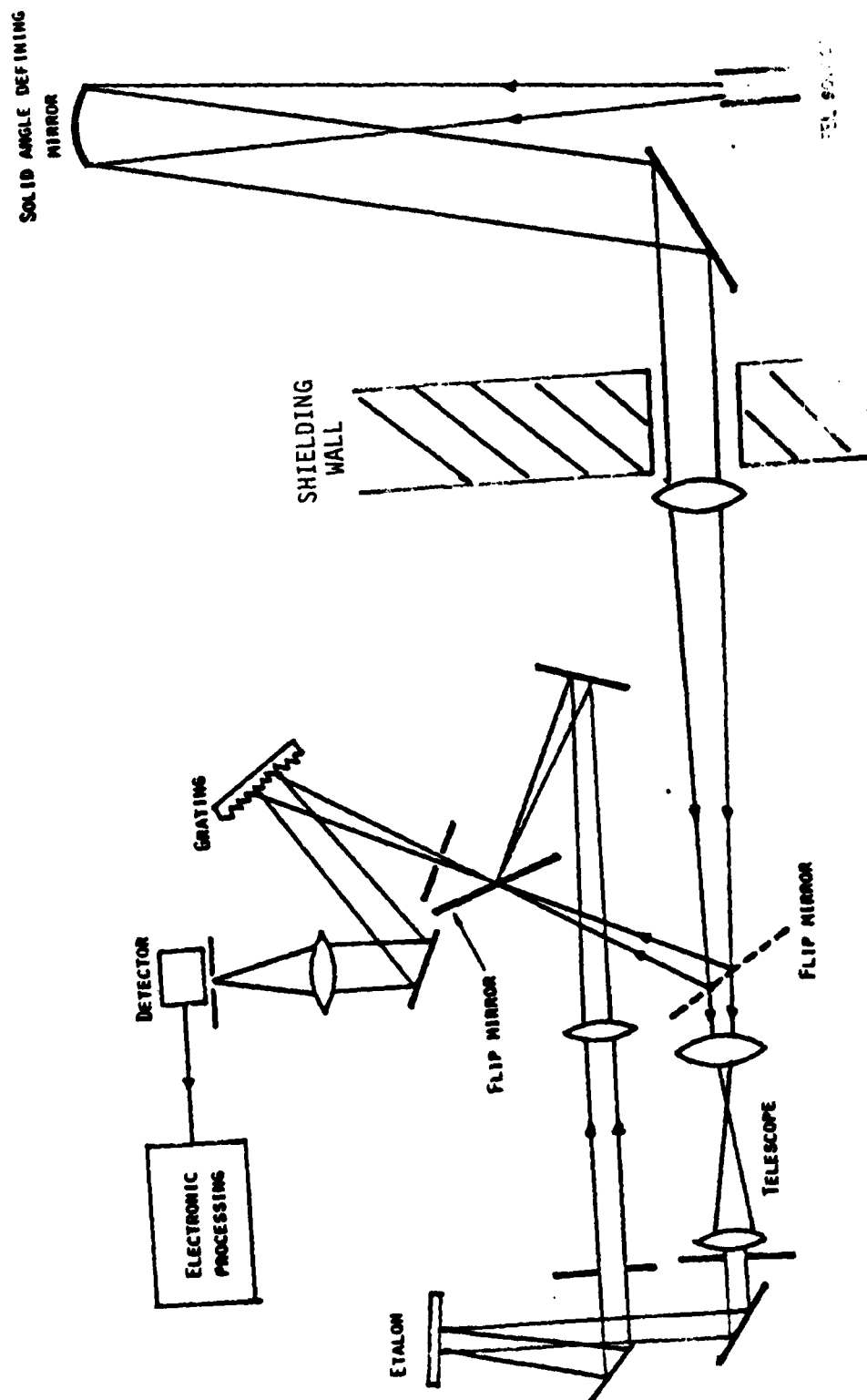


Figure 12. Detection System

#### IV RESULTS

The TRW free electron laser program has accomplished the following major goals:

- 1) Demonstrated electron deceleration consist with theory (Figure 15).
- 2) Direct optical measurement of gain from a free electron laser.
- 3) Measured the spontaneous radiation spectrum and determined its functional dependence on
  - energy
  - energy spread
  - emittance
  - taper of wiggler
  - collection aperture
  - steering of electron beam
- 4) Developed sensitive and fast electron beam emittance measurement system.
- 5) Developed high resolution very fast electron energy distribution monitor.
- 6) Developed an ultra-sensitive optical gain measurement diagnostic.
- 7) Measurement of the upper limit on large signal tapered wiggler gain.

The electron energy distribution was measured using an optical fiber profile monitor at the magnetic spectrometer's focal plane, as described previously. Figure 13 shows typical experimental data, in which the three traces represent the electron energy distribution with and without the injected laser pulse and the displayed difference. The data displayed was accumulated over a series of 5000 samples of the interaction. The narrower distribution is the energy distribution without the laser input, while the wider one is with the laser input.

Figure 14 shows the raw signals from the spectrometer, where each trace represents the energy distribution of a single electron beam pulse. The apparent jitter is due to small fluxuations in the beam energy from shot to shot,  $\sim .1\%$ . The top photo shows the electron distribution without the laser input. The second photo displays the distribution with the laser interaction. The last photo exhibits both together on the same picture. This

## FEL INTERACTION

### ELECTRON ENERGY DISTRIBUTION WITH AND WITHOUT LASER INTERACTION AND DIFFERENCE (AVERAGED)

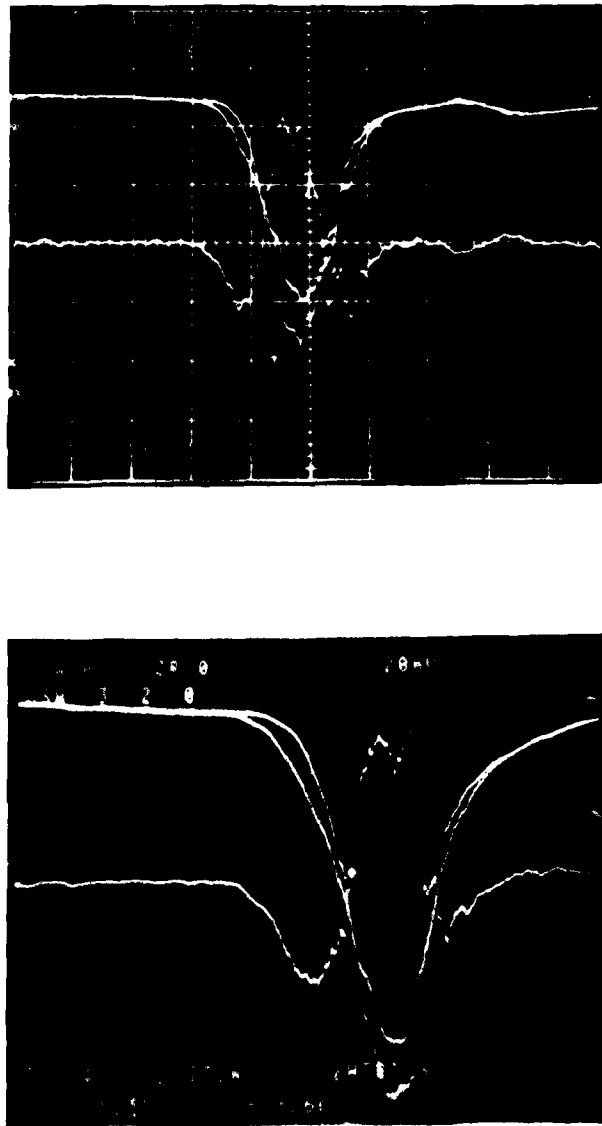
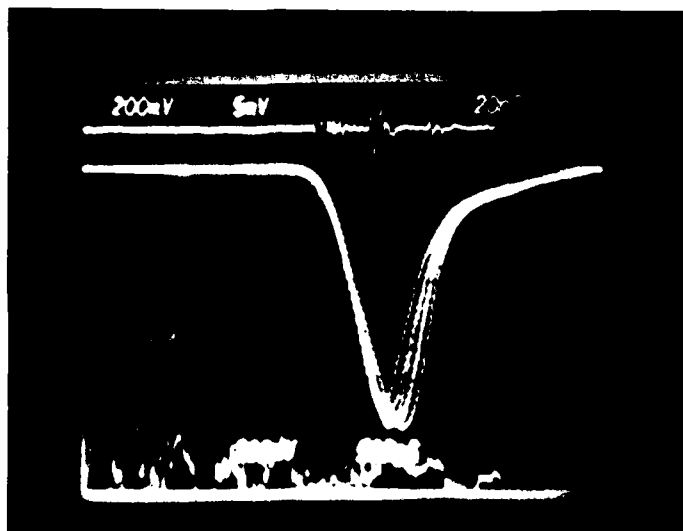


Figure 13. Two examples of FEL interaction. The two upper traces are the electron distribution with and without the injection laser. The bottom trace is the difference between them times 2.5.

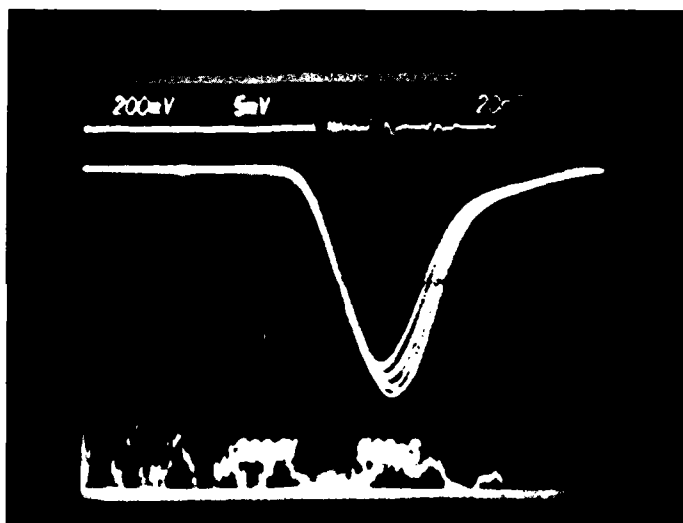


# SINGLE PULSE ELECTRON ENERGY DISTRIBUTIONS

WITHOUT  
INPUT  
LASER



WITH  
INPUT  
LASER



BOTH  
WITH & WITHOUT  
INPUT  
LASER

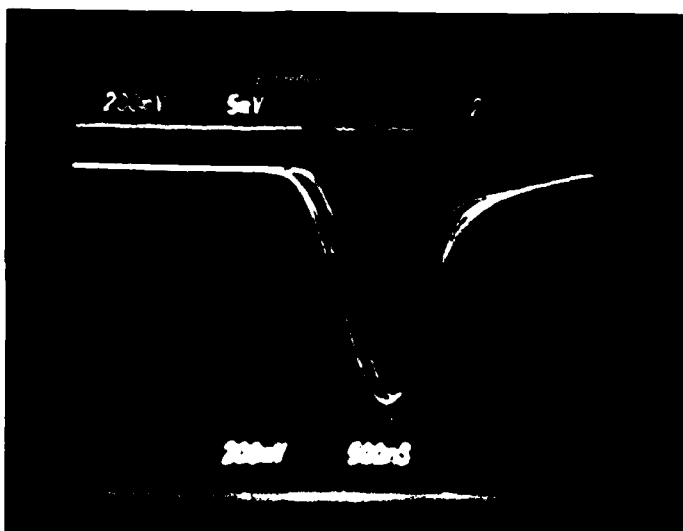
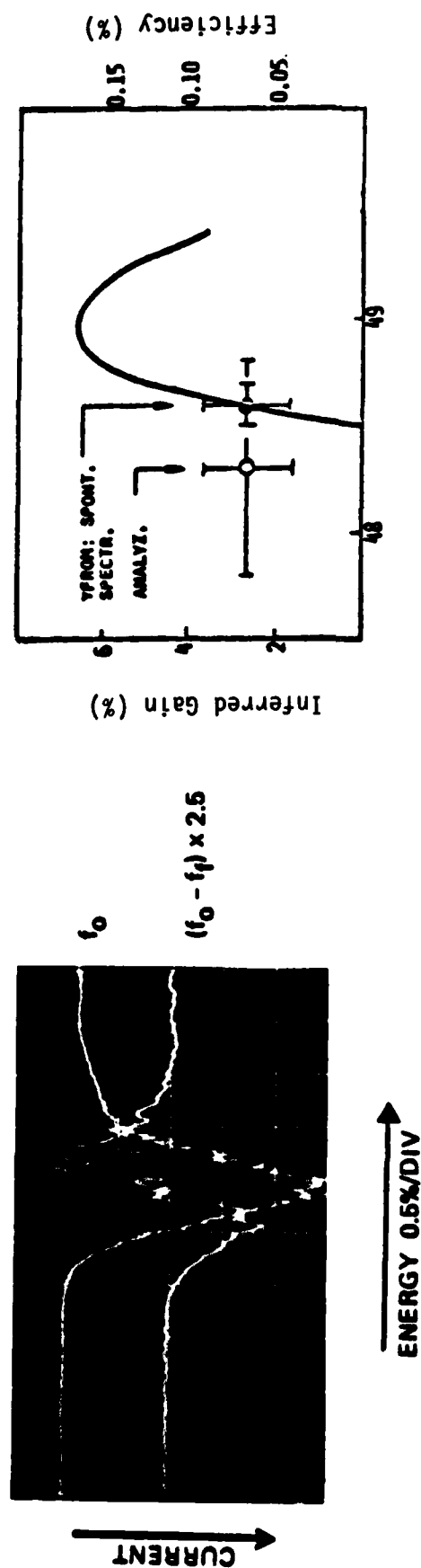


Figure 14. Electron Energy Distributions

# FEL INTERACTION: ELECTRON BEAM ENERGY LOSS



Wiggler:	2.25% taper rate corresponding to expected deceleration of 0.6%
Result:	$12.6 \pm 4.1\%$ of beam electrons decelerated by 0.6%
Efficiency:	0.7%
Gain:	2.7%

Figure 15. Analysis of the FEL Interaction

demonstrates the interaction plainly with the two distributions discernible by their different widths.

Figure 16 shows experimental changes to the electron beam energy distribution caused by the interaction with an input laser. The wiggler is set with a .6% taper. The first graph has the electrons being both accelerated and decelerated in about the same numbers, so that in this example the electron energy distribution was increased with little change in the average energy. In the second graph, there were many more electrons decelerated than those which were accelerated. The last graph in this figure displays one of the best examples of average deceleration with almost no electrons being accelerated by the interaction. In this case, about 10% of the electron were decelerated a little more than 1/2%, corresponding to an efficiency of about .06% and a gain of about 1.2%. It is believed that the interaction was largely limited by the emittance of the accelerator which averaged around  $8\pi$  mm-mrad, but with a large variance as illustrated in Table 1. Figure 17 shows the gain predicted as a function of emittance and energy spread, in this case without any taper. It also shows an experimental measurement of the gain, which will be described below. The sensitivity to emittance is such that going from  $8\pi$  mm-mrad to  $2\pi$  mm-mrad caused the gain to increase more than 10 fold, underscoring the requirement that accelerators used for free electron lasers need to have superb emittance and energy spread parameters. This is due to the physical principle that the free electron laser cannot be brighter than the electron source which drives it.

Direct optical measurement of small signal gain with a constant wiggler was measured using the optical measurement setup described in the previous section. The small  $\text{CO}_2$  laser was used directly as input to the free electron laser instead of being used to injection mode lock the high energy  $\text{CO}_2$  laser. The laser signal varied from 1 to 10 mW. The energy of the electron beam was varied about 25 Mev. The data was taken subtracting off the spontaneous signal by measuring the detector level with the laser input blocked. The gain was roughly invariant over the range of input powers, and scale roughly with current over the 5-10 Amp range. The error bars are significant, so small deviations from expected behavior were unmeasurable. Figure 17 shows the experimental gain

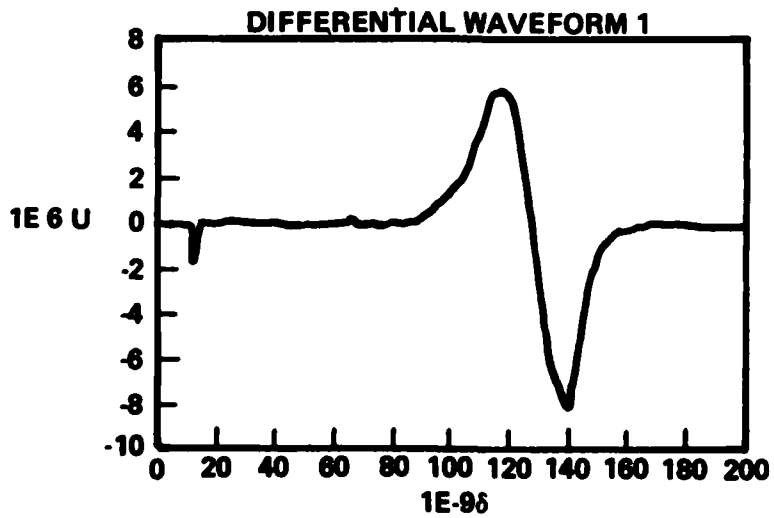
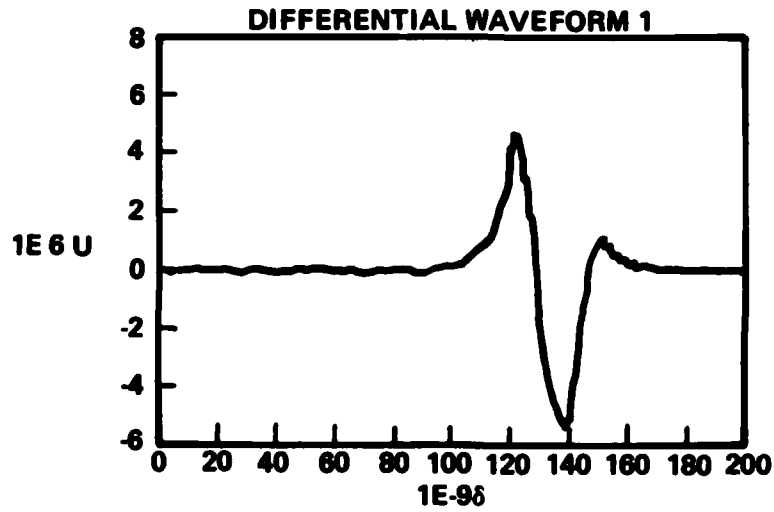
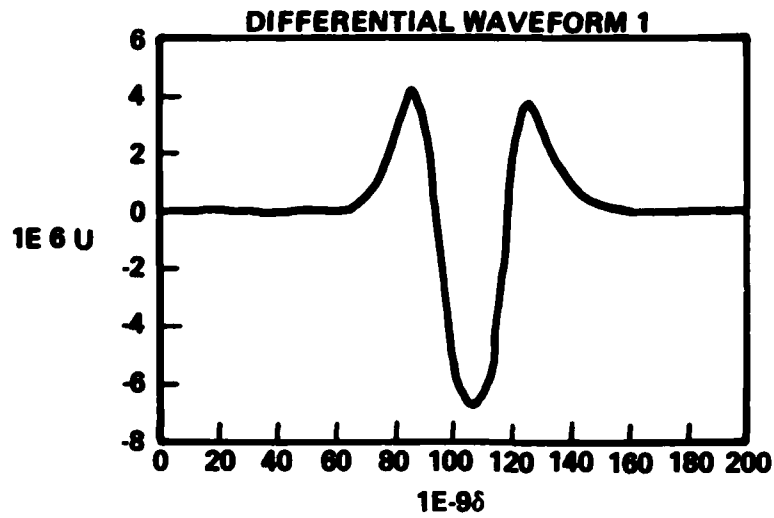


Figure 16. FEL INTERACTION  
Laser Induced Changes in the Experimental Electron Beam Energy Distribution

TABLE 1

SAMPLING OF THE MEASURED EMITTANCE  
AT THE BEGINNING OF A SHIFT

4.4 $\pi$ mm mrad	14.9 $\pi$ mm mrad
2.5 $\pi$ mm mrad	13.4 $\pi$ mm mrad
2.9 $\pi$ mm mrad	8.9 $\pi$ mm mrad
8.4 $\pi$ mm mrad	8.7 $\pi$ mm mrad
5.7 $\pi$ mm mrad	7.4 $\pi$ mm mrad
7.5 $\pi$ mm mrad	6.8 $\pi$ mm mrad
7.3 $\pi$ mm mrad	7.0 $\pi$ mm mrad
4.3 $\pi$ mm mrad	4.6 $\pi$ mm mrad
8.0 $\pi$ mm mrad	13.9 $\pi$ mm mrad
10.0 $\pi$ mm mrad	19.2 $\pi$ mm mrad
18.7 $\pi$ mm mrad	7.0 $\pi$ mm mrad
4.0 $\pi$ mm mrad	6.7 $\pi$ mm mrad

The values represent the instantaneous emittance of the linac at the beginning of each shift before any attempt was made to improve the phase space.

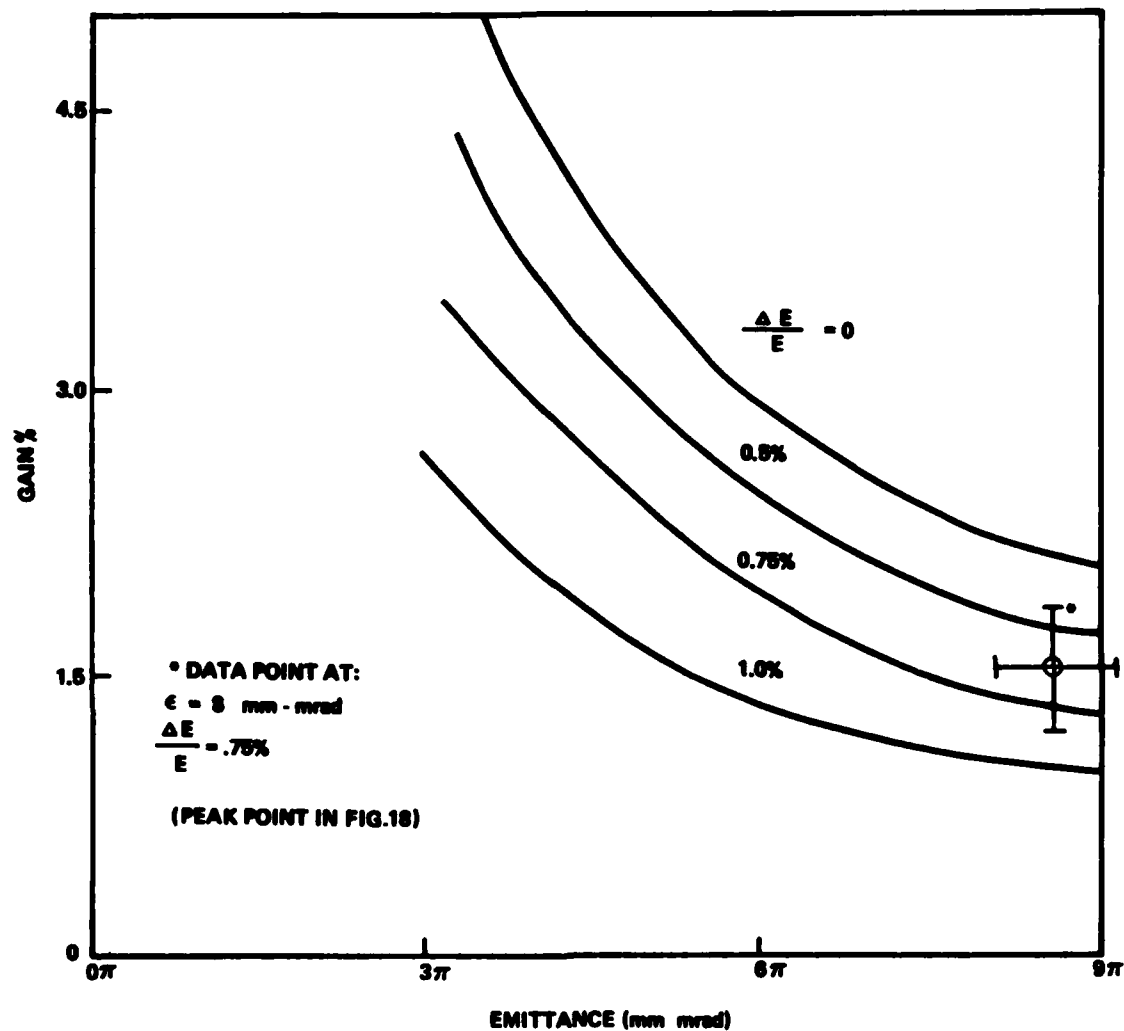


Figure 17. Peak Small Signal Gain Versus Emittance and Energy Spread for an Untapered Wiggler

agrees very well with the modeling. Gain was measured at four different energies, allowing a rough approximation to the energy behavior of the gain to be displayed in Figure 18. This curve was not reproducible due to emittance fluctuations, so it is only shown to indicate that the general character of the interaction is as expected. Note that this measurement was of the actual optical gain signal, not a derived quality, so there is no recourse to theory to extract the gain value. It is of value to note that when comparing this data to others, care must be taken, the above gain includes the radiation extracted as enhanced spontaneous radiation in systems with crossed polarizers.

The radiation emitted by the electron beam passing through the wiggler was found to be very useful as a diagnostic, in that the spectrum of the radiation gives a large amount of information about the electron beam. Experimentally, we have observed the effect of the energy of the electrons on the wavelength of radiation, the effect of energy spread and emittance changes on the width of the spectrum, the effect of changing the wiggler taper on both the width and the wavelength of the spectrum, the effect of collection solid angle on the spectrum and intensity, and the effect of missteering on the spectrum. In addition, the spontaneous radiation was used as a timing reference during the gain experiments.

Figure 19 illustrates the spectral shift of the spectrum with a change in the electron energy. The position of the spectral peak is a very good absolute calibration of the electron energy. Thus, by measuring the spectrum, the energy of accelerator could be adjusted up or down to match the desired operation condition.

Figure 20 illustrates the change in the spontaneous radiation caused by changes in the width of the electron beam's energy distribution. It is not surprising that the width of the radiation increases with increasing electron beam energy spread. Very similar behavior is observed with emittance increases.

Figure 21 shows that increasing the taper of the wiggler system decreases the wavelength of the spontaneous radiation and broadens the distribution.

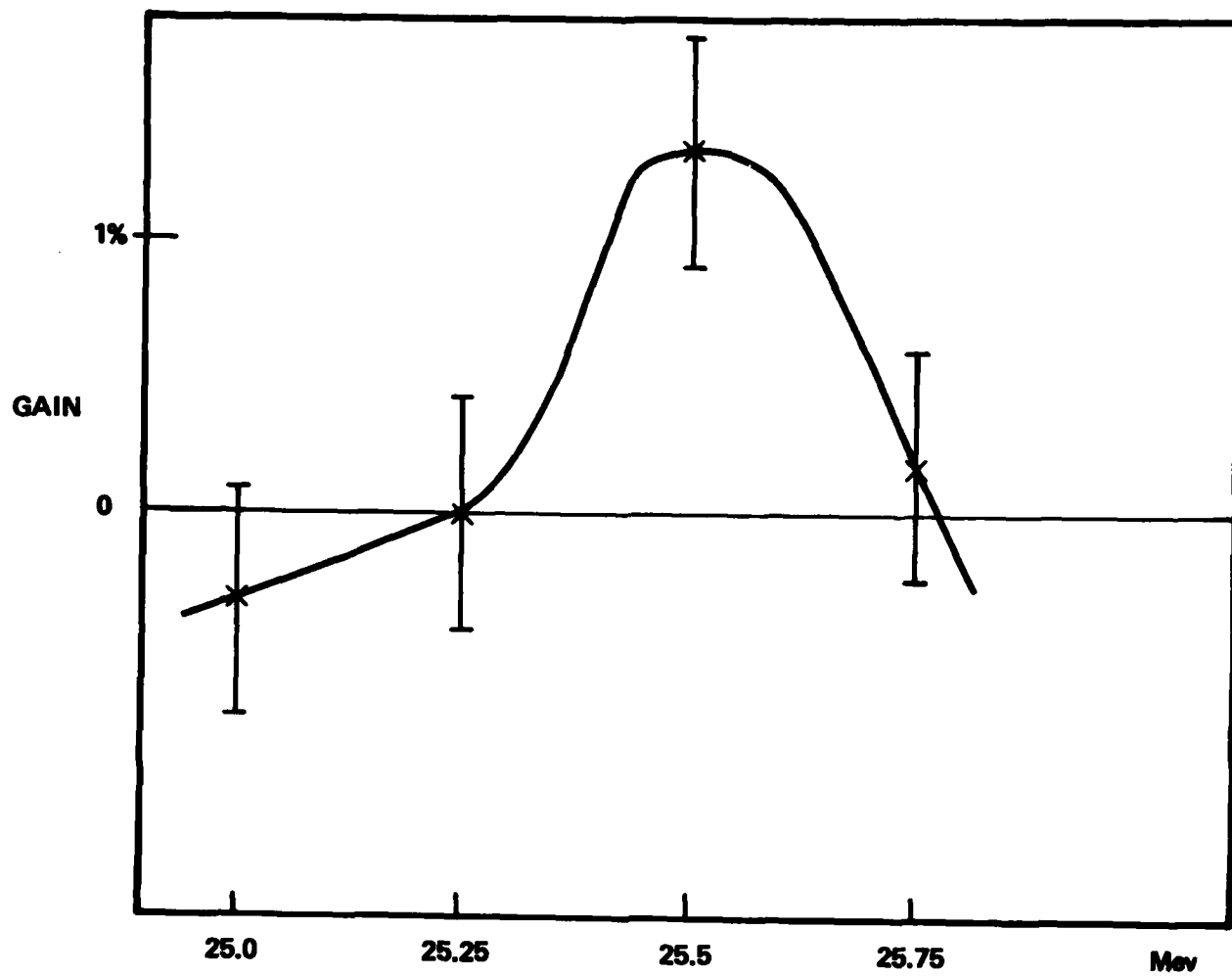


Figure 18. Small Signal Gain versus Electron Energy for an Untapered Wiggler



# Technique To Optimize Linac Energy for Maximum Gain

## Spontaneous Radiation Spectrum

.5" Aperture

• 25.0 Mev }  
 MAGNET SETTING  
 o 25.2 Mev }

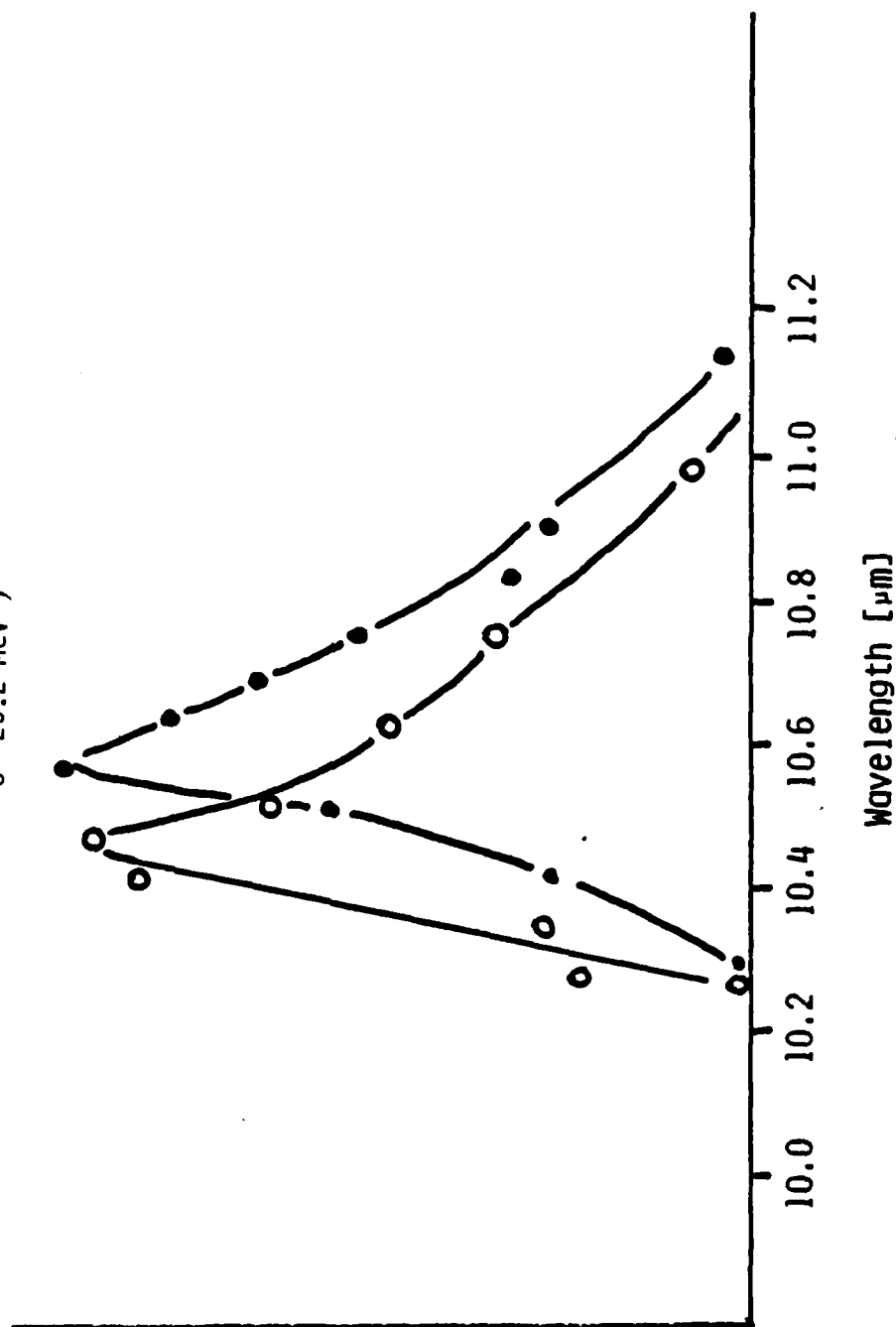


Figure 19. Optimizing the Linac Energy

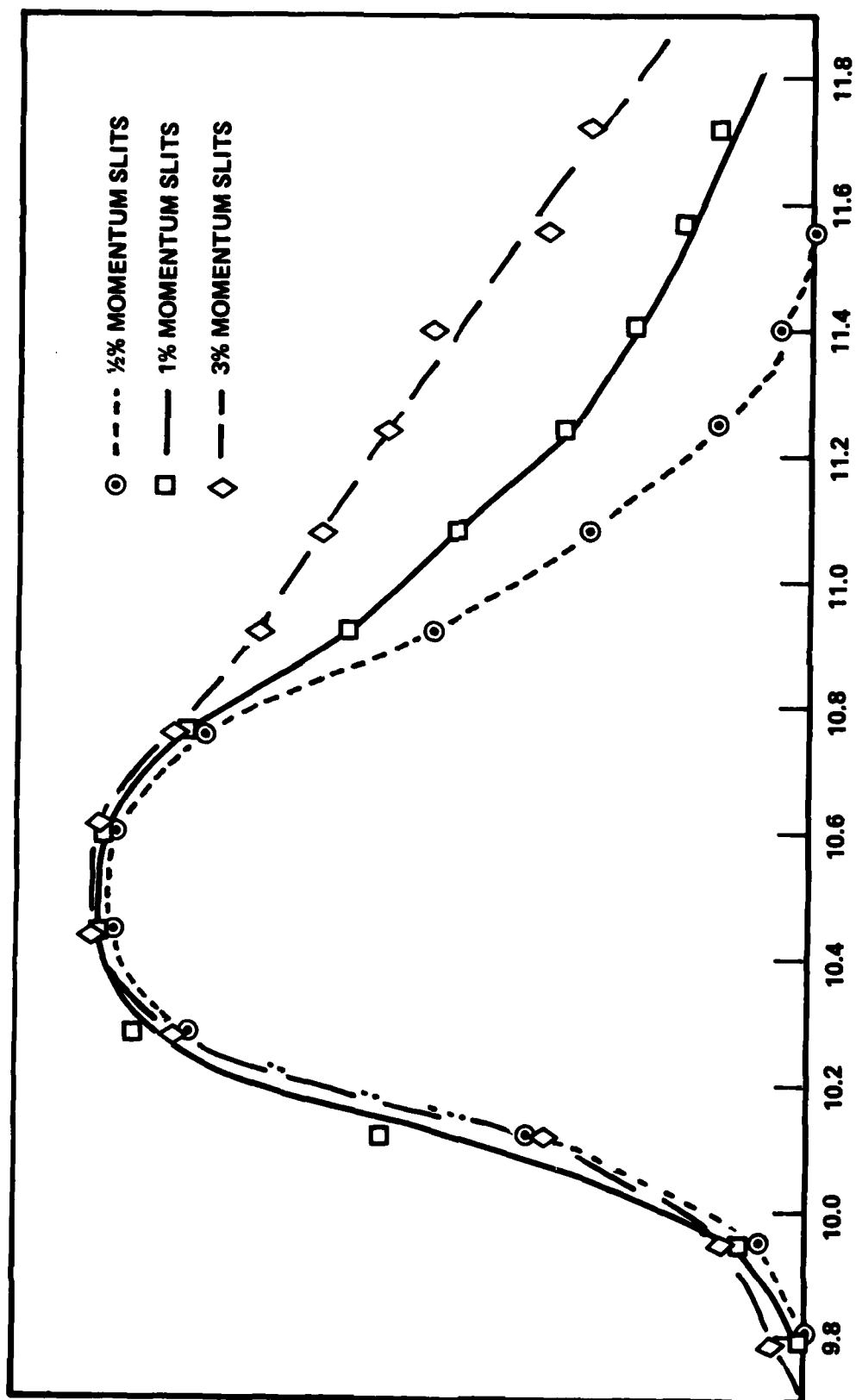


Figure 20. Spontaneous Radiation for Different Energy Spreads

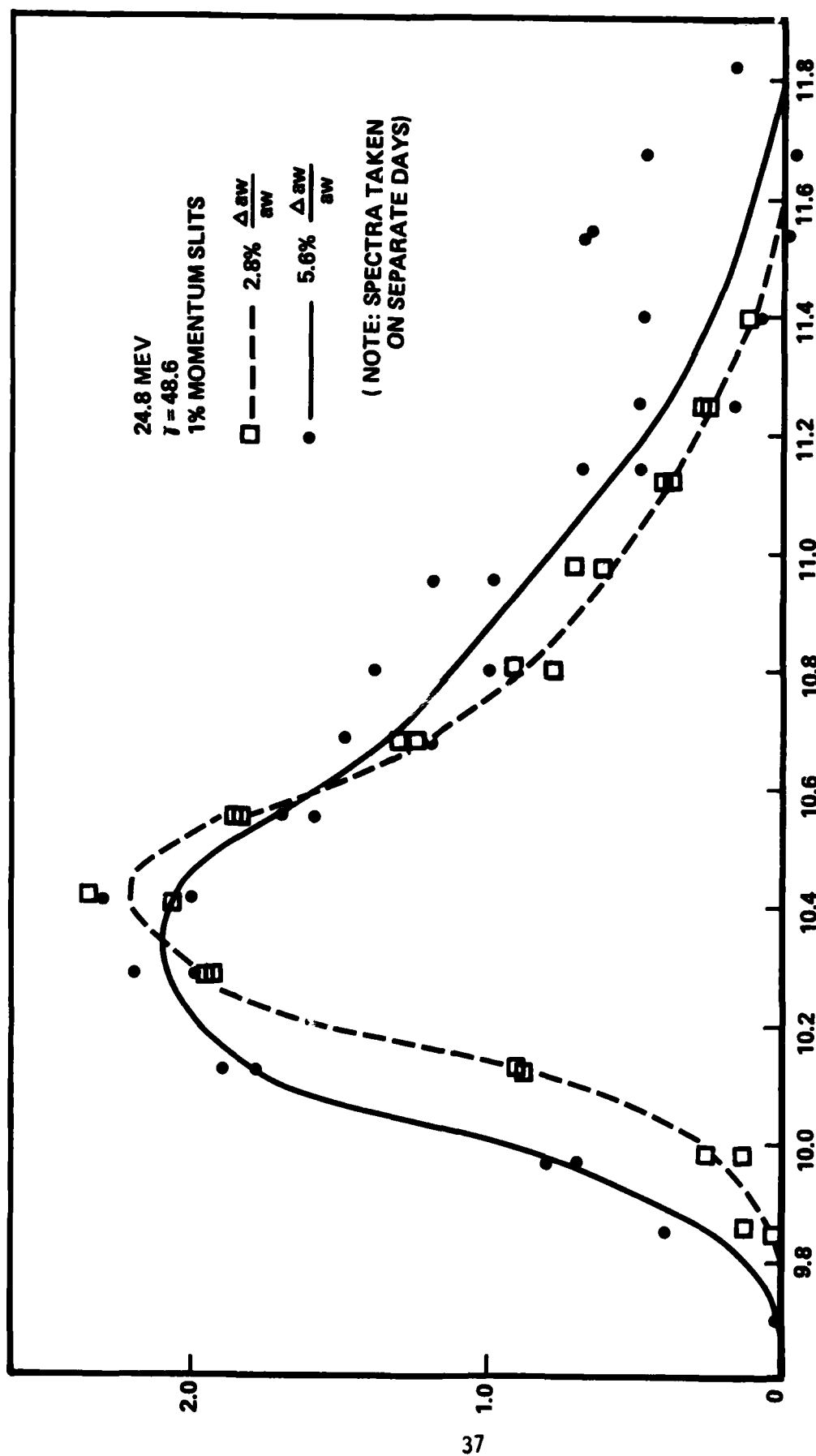


Figure 21. Spontaneous Radiation at Two Different Wiggler Tapers

Figure 22 illustrates the dependence of the spontaneous radiation on the solid angle of the collection optics. The radiation becomes longer wavelength and broadens as the collection aperture increases. The radiation has an opening angle of about 1.5 mrad, very consistent with  $a_w/\gamma = 1.4$  mrad.

Large signal gain measurements with the tapered wiggler were attempted. The input power was 10 MW and an wiggler taper of 1.6% in energy was used. Crossed polarizers and a spatial filter (pin hole) were used with the optical system (minus the etalon) described previously. The calculated and measured sensitivity of this system was 1.5% gain, so at the 95% confidence level the gain was less than 3%. This experiment predated the installation of the emittance diagnostic, but assuming the emittance was  $8 \pi$  mm mrad, then the theoretical gain would have only been .5%. If it had been  $2 \pi$  mm mrad, then the gain should have been 6%. To the threshold sensitivity of the system no gain was measured.

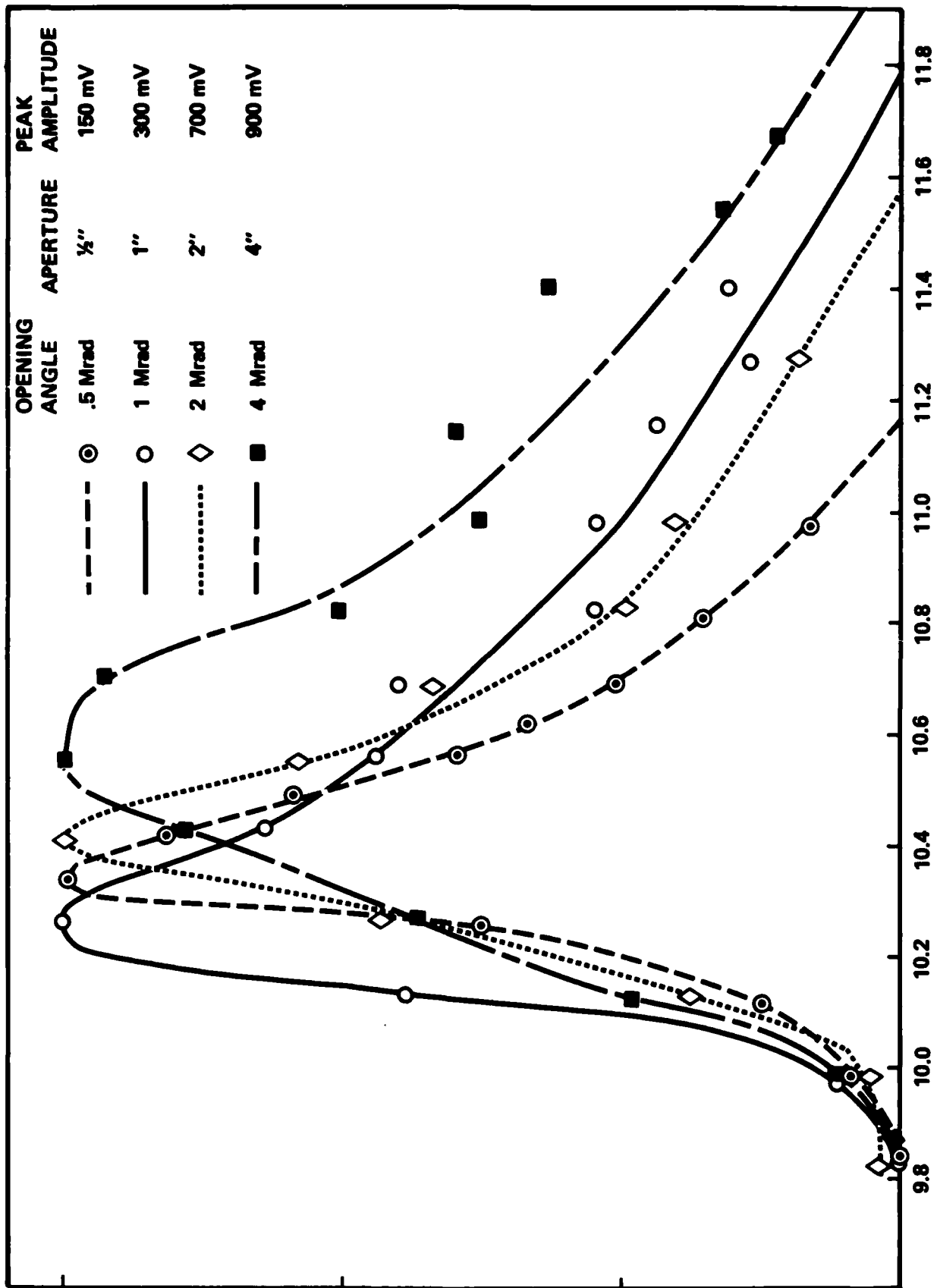


Figure 22 Spontaneous Radiation as Function of Collection Aperture

## V THEORY

In parallel with the experimental program a theoretical effort has been performed to address the issues associated with oscillator start-up. This effort has centered on understanding the principles of operation of multi-component wigglers as opposed to fixed taper wigglers. The high predicted saturation efficiencies of tapered wiggler FEL oscillators has been the impetus behind the high power FEL programs. There are difficulties with this approach. In particular, the gain of a high power FEL with a tapered wiggler peaks at a flux for which the taper is optimum; it decreases at other fluxes.<sup>1</sup> Further, the output radiation frequency at which the gain is maximum as well as the gain spectrum width changes as a function of input power for a given taper.<sup>2</sup> Thus, a tapered wiggler free-electron laser (TWEL) becomes less attractive as an oscillator. Below we discuss how these unwanted oscillator characteristics can be eliminated by substituting a more complex, multi-component wiggler (MCW) configuration for the tapered wiggler.

The MCWEL is based on the physical principles of both the TWEL and the constant (untapered) wiggler free electron laser (CWEL). In a constant wiggler, the electron beam is injected with an energy ( $\gamma_{inj}$ ) above the resonant energy ( $\gamma_R$ ) in order to obtain maximum net deceleration of the electrons.  $\gamma_R$  is the energy associated with the phase velocity of the ponderomotive potential or bucket formed by the wiggler and radiation fields. In a TWEL, the wiggler is tapered following the rate of change in  $\gamma_R$  in such a way that there is a resonant particle whose phase stays stationary through the interaction length and a maximum number of electrons can be trapped in the ponderomotive potential well. The rate of deceleration in  $\gamma_R$  is proportional to the square root of the input power,  $P_S^{1/2}$ ; hence, for a given taper there will be only one radiation power that is optimum ( $P_S^{op}$ ). Further, the optimum  $\gamma_{inj} = \gamma_{inj}^{op}$  at this power is equal to  $\gamma_R$  to maximize the number of trapped electrons. For radiation powers smaller than the optimum, the closed orbits begin to open up and the particles remain untrapped. Energy extraction can occur if the average energy relative to  $\gamma_R$  increases at a slower rate than the decrease in  $\gamma_R$  due to the wiggler taper. This in turn requires  $\gamma_{inj}^{op} < \gamma_R$ . For a practical oscillator  $\gamma_{inj}$  remains fixed and therefore, as the power in the cavity increases, the output frequency shifts in such a way

to "reaccommodate" the resonant energy so that the difference  $\gamma_{inj} - \gamma_R$  has the optimum value for maximum gain. For any taper  $\Delta$  there is an optimum power for maximum gain operation and this power increases with  $\Delta^2$  and decreases with the interaction length.<sup>3</sup> In addition, for any  $\Delta$  the gain spectrum shifts as a function of increasing power with larger shifts occurring for larger tapers.

In the MCWFEL oscillator scheme, a number of wiggler components is utilized in such a way that each component operates at its own optimum power and either is transparent or enhances the performance of other components at other powers. In addition, in order to reduce the gain spectrum width, the various wiggler components are chosen with different wavelengths  $\lambda_w$ , and amplitudes  $B_w$ , and separated by proper amounts of drift space in such a way that  $\gamma_R$  is different for each component and  $\gamma_{inj} = \gamma_{inj}^{op}$  in each section.

The simplest MCW combination is a two component one consisting of a CW followed by, or following, a tapered wiggler (TW). Since  $\gamma_{inj}^{op} > \gamma_R^{CW}$  but  $\gamma_{inj}^{op} \approx \gamma_R^{TW}$ ,  $\lambda_w$  and  $B_w$  are chosen in such a way that  $\gamma_R^{CW} < \gamma_R^{TW}$ . The small signal gain is enhanced by the constant wiggler section and the function of the second section can be affected by the action of the first section on the electron distribution. For example, if the CW is located before the TW, the electrons can be "bunched" in phase space at the end of the CW. The optimum bunch phase depends on the taper<sup>3</sup>. Thus, in order to introduce the electrons into the TW in a proper fashion at high powers, a very small drift space proportional to the difference in optimum phases and to  $\lambda_w$  is required. On the other hand, if the CW is located after the TW, due to the very low small signal gain of the TW, no bunching occurs in the electrons before entering the CW for low input powers and the CW is transparent to high powers.

In addition, the large signal gain can be enhanced by a system similar to an optical klystron.<sup>1</sup> That is, a large drift space where the electrons bunch as they free stream can be added between the CW and TW components to increase the number of trapped electrons for the TW operation. The drift length necessary to achieve bunching is calculated as the length that it takes particles separated in energy by  $\delta\gamma/\gamma$  and in space by half a radiation wavelength to come together. This length is:  $L_D = \lambda_s \gamma^2 / [2 (\delta\gamma/\gamma)]$ ,

where  $(\delta\gamma/\gamma)$  is induced by the synchrotron rotation in the ponderomotive potential. The drift length  $L$  can be replaced by a dispersion magnet which produces an "effective drift distance" proportional to  $L^3$  and, therefore, permits the enhancement of gain with shorter devices.<sup>2</sup>

In order to obtain quantitative confirmation of these ideas, they were numerically investigated utilizing the TRW 1-D code that includes diffraction effects of the input Gaussian optical beam and finite electron beam emittance.<sup>1</sup> The numerical results presented here utilize the optimum parameters of the TRW experiment<sup>4</sup>:  $\gamma_s = 10.6 \mu$ , electron beam energy  $E_b \approx 25$  MeV, electron beam peak current  $I \approx 40$  A, electron beam radius  $\approx 2.25$  mm  $\approx$  photon beam waist, total interaction length  $\leq 4$  m, energy spread  $\Delta\gamma/\gamma = .5\%$  and  $a_w \approx .98$ . Figure 23 shows the gain spectrum obtained for a simple  $L = 4$  m tapered wiggler FEL for different input powers. The large taper ( $\Delta = 35\%$ ) is required to obtain sufficiently high gain ( $> 8\%$ ) at 500 MW. For  $P_s < 1$  MW the gain is below 5% with a wide spectrum,  $\Delta\omega/\omega > 4\%$ . The peak gain frequency shifts more than 2 percent from the "resonant" output frequency.

In order to test the MCW idea, we first simulated a 3 m two component wiggler as illustrated in Figure 24. Case (1) corresponds to a 1 m CW followed by a 2 m TW separated by a 1 cm phase adjustment section; the order of the components is inverted for case (2). The parameters are chosen in such a way that  $\gamma_R^{CW} < \gamma_R^{TW}$  and  $\gamma_{inj} = \gamma_R^{TW}$  is optimum for the whole system. The exact parameters utilized in the simulation are indicated in the figure. The taper utilized,  $\Delta = 20\%$ , would correspond to an optimum power of 500 MW for a simple TW with  $L = 2$  m and of 100 MW if  $L = 3$  m. The gain curve (gain vs power, at fixed  $\gamma$ ) for the simple TW FEL is also shown in Figure 24. The effect of the 1 m CW section in case (1) is to increase the small signal gain over that of a simple 3 m TW FEL by a factor larger than 10. At very high powers ( $P > 500$  MW) the system behaves as a simple 3 m TW of  $\Delta = 20\%$ . The gain at 100 MW is enhanced by a factor of almost 2 and the optimum power now occurs at 50 MW. For case (2), the small signal gain is also increased by almost a factor of 10; however, for very high powers the system behaves as a simple 2 m TW FEL.



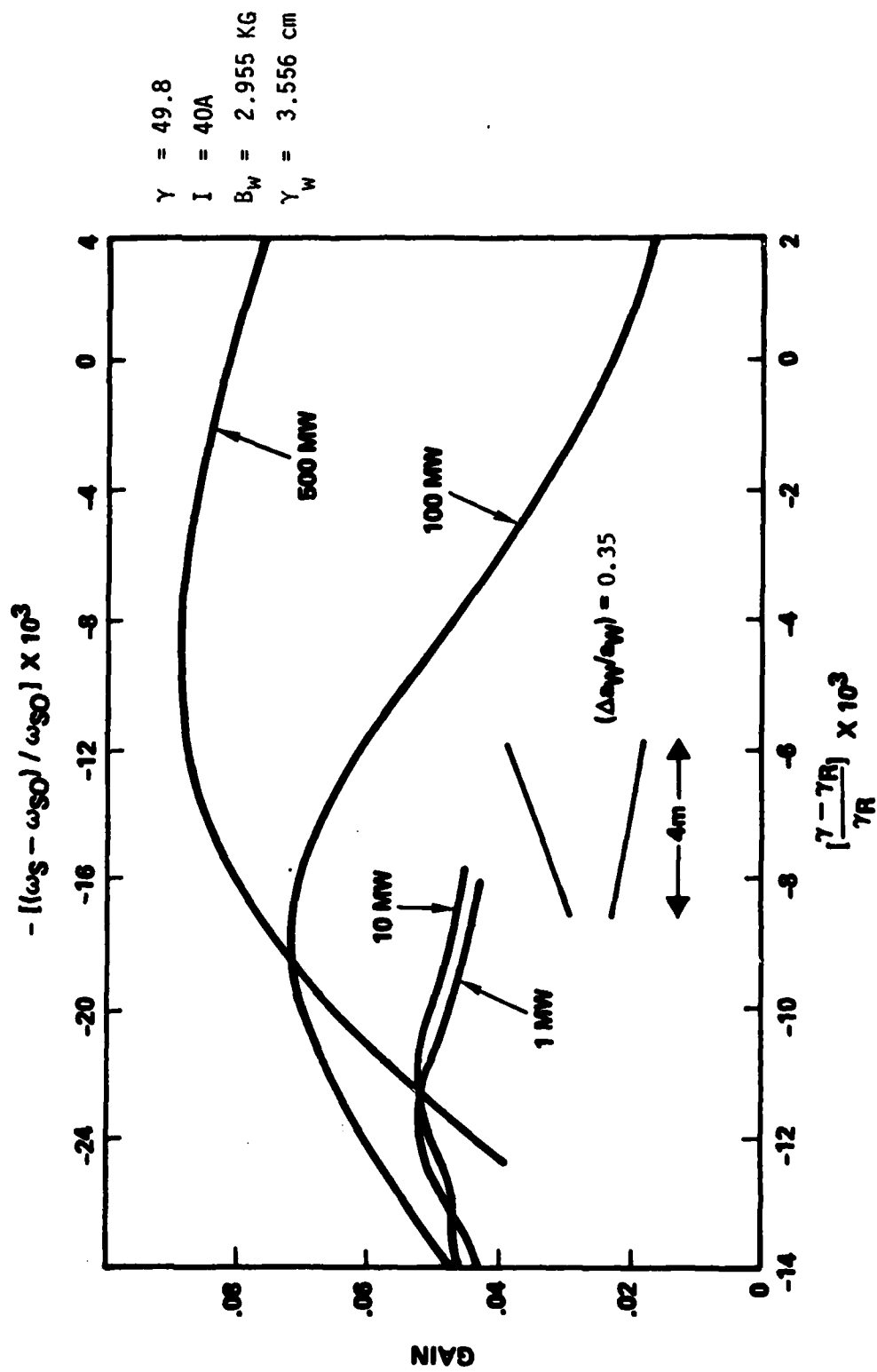
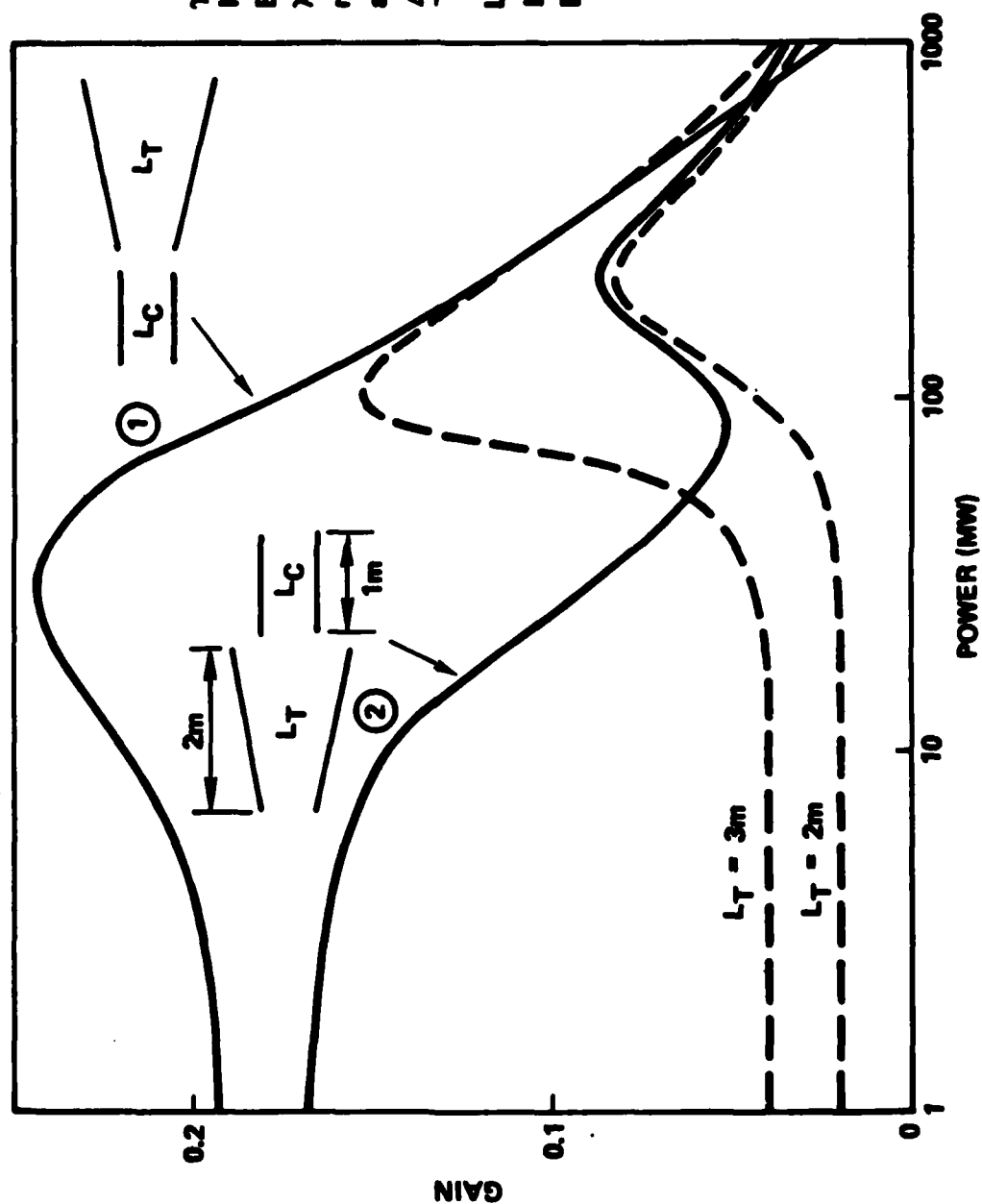


Figure 23: Gain Spectrum for Different Input Powers - TWFEEL



$\gamma = 49.8 = \gamma_R (L_T)$   
 $I = 40A$   
 $B_W = 2.955 KG$   
 $\lambda_W = 3.556 cm$   
 $r_0 = r_p = 2.25 mm$   
 $\eta_W = 0.98$   
 $\frac{\Delta \eta_W}{\eta_W} = 0.2$   
 $L_T = 2m$   
 $L_C = 1m$   
 $B_{WC} = 2.86 KG$

Figure 24: Multicomponent FEL (MCFEL) Gain vs. Input Power for a Two-Component Wiggler FEL - Dashed Lines are Gain Curves for Simple TWFE's.

In case (1), the initial CW acts as a buncher section of the TW and the whole system is equivalent to a TW of length  $> 3$  m for high powers. Hence, the optimum power of this device is smaller than that of a 3 m TW for the same taper  $\Delta$ . For very high powers, the bucket size is sufficiently large that the increase in bunching does not play an important role and the whole system behaves as a 3 m TWFE. For case (2), the CW is practically transparent to high powers and all the gain is determined by the 2 m TW. The dip in the curve is due to the fact that this system essentially behaves like two separate components and the optimum power of the 2 m TR is at those high powers for which the CW gain curve is already very small. Obviously, several possibilities can be suggested to obtain a monotonically decreasing gain curve with sufficient gain at high powers. For example, a system similar to (2) with a very small taper ( $\Delta \sim 1\%$  or so) for the first section will decrease by a very small amount the small signal gain but will increase the gain at the dip. Another possibility is to consider the effect of drift sections in the high signal gain.

In order to test the optical klystron idea for a TWFE, a three component wiggler: (CW, drift space, TW) was simulated as shown in Figure 25. In this figure the results obtained for a short prebuncher CW section ( $L_C = 15$  cm) followed by  $L_D = 1$  m drift section and by a 2 m and a 3 m TW sections, respectively, are compared with those of simple 3 m and 2 m TWFE's. The lengths  $L_C$  and  $L_D$  were chosen to maximize the bunching at high power. The gain and efficiency are enhanced at  $P_S^{OP}$  by a factor of almost 2. This enhancement will not be effective if the electron beam has a large effective energy spread. In this case the potential well will be full from the beginning and the particles bunched in phase space will spread in energy beyond the well.

As a final demonstration of the possibilities of a MCW system for FEL oscillators, a four component system was simulated as illustrated in Figure 26. Essentially, a prebuncher (CW plus drift section) was added to the case (2), of Figure 24. In addition, the taper was decreased to 13% corresponding to an optimum power of the simple 2 m TW near 100 MW, coincident with the optimum power of a simple 3 m TW with  $\Delta = .20$ . In this system the small signal gain is further enhanced by utilizing now the whole initial 3 m as a prebuncher and drift space for the final

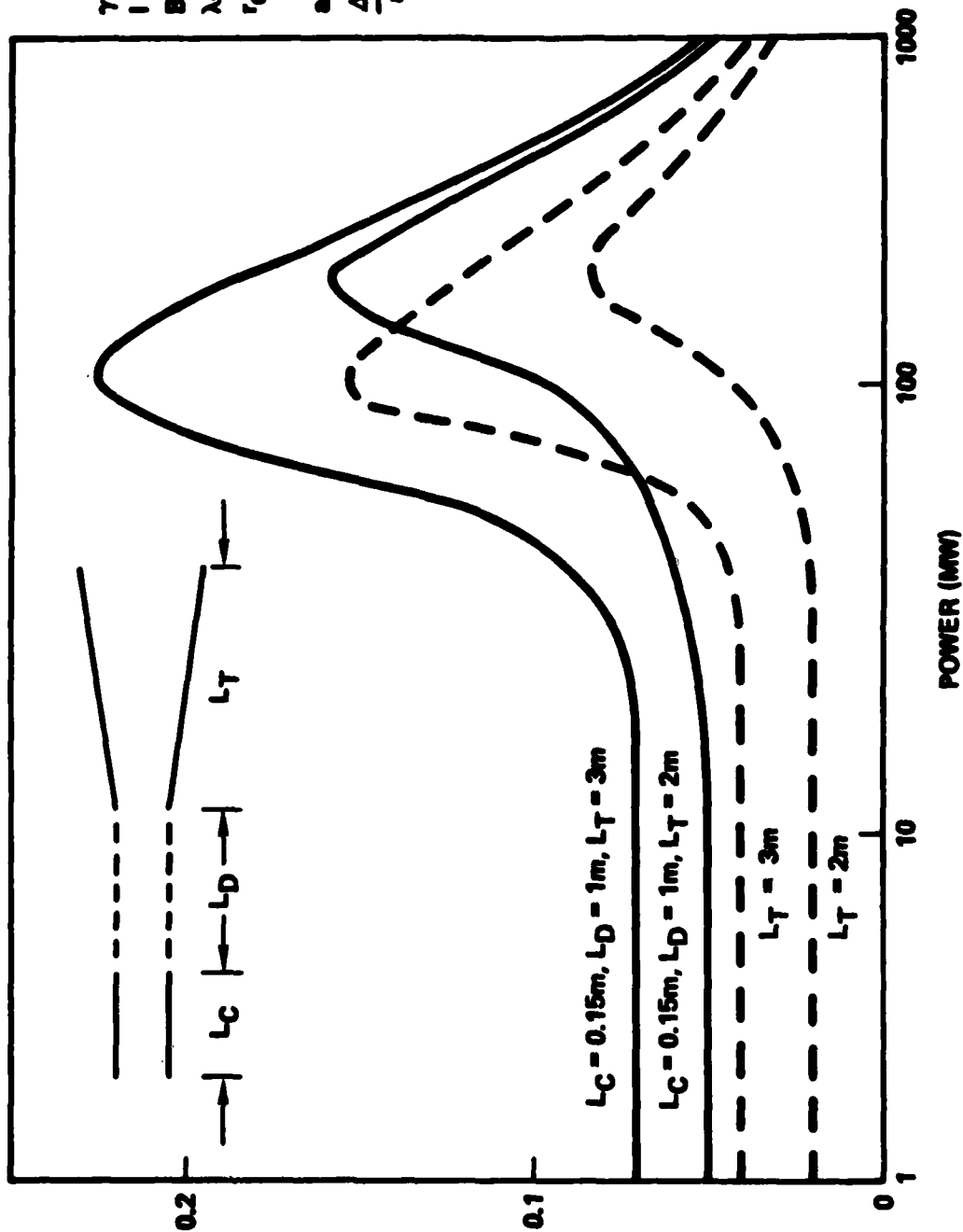


Figure 25: Multicomponent FEL GAIN vs Input Power for a TW with Prebuncher (Two Components with Drift Space) - Dashed Lines are Gain Curves for Simple TWEL's.

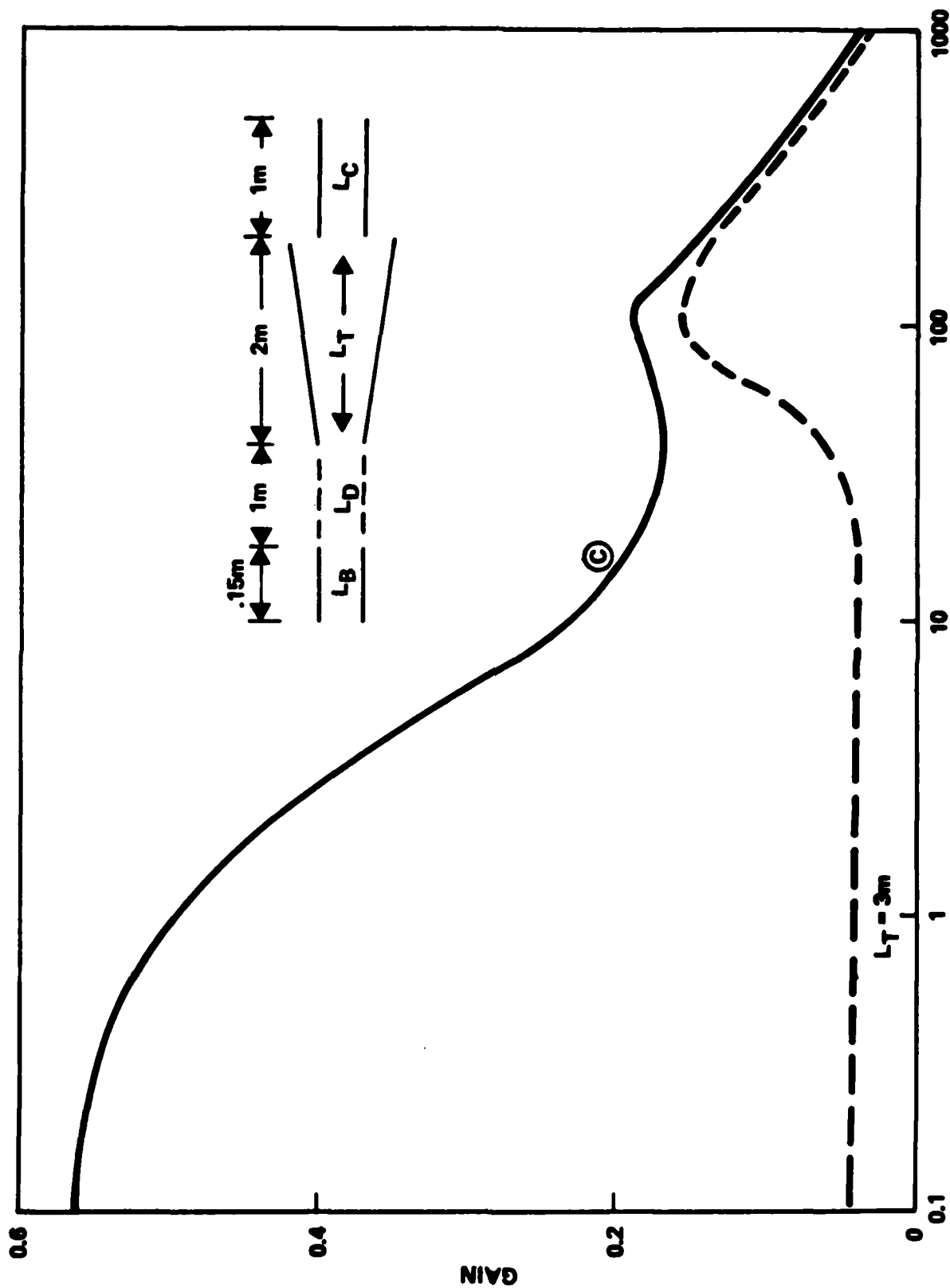


Figure 26: Multicomponent FEL Gain vs. Input Power for Three-Component Wiggler with Drift Space - Same Parameters as Figure 25 Except  $\Delta = .133$ ,  $\gamma = \gamma_R(L_B) = \gamma_R(L_T)$  - Dashed Line is Gain Curve for a Simple TW with  $L_T = 3m$ .

1 m CW section. Note that the small signal gain is 60% compared to 20% in Figure 24 and less than 3% for the single 3 m TW. The large signal gain is increased over that of a 3 m taper due to the prebuncher, however, this increase is less than a factor 2 due to the initial energy spread (.5%) of the electron beam. In addition, the whole gain curve has an almost (except for the small bump at a 100 MW) monotonically decreasing characteristic. The case shown in Figure 26 has a total single pass efficiency  $\eta \approx 3\%$  at  $P \approx 600$  MW which is assumed to be the saturation power for a cavity loss of 5%.

More important than to show gain enhancement at a given output frequency is to look at the improvement in the gain spectrum curve. Figure 27 shows the decrease in the spectrum width for small signals, an increase of the maximum gain peak and an negligible shift in the peak. This is due to the flexibility of choosing different  $\gamma_R$  for the different sections of the MCW. These results can be optimized further by utilizing a very small tapered wiggler instead of the CW. The number of photon passes calculated to obtain saturation at 600 MW assuming an injected power of 1 MW was 90 for the case shown in Figure 26. Further, the number of passes increases only by 6 for each order of magnitude that we wish to decrease in the injected power.

In conclusion, we have analyzed the main characteristics that determine the gain and gain spectrum vs power curves for different tapers. From those characteristics we have developed a scheme that permits the operation of the FEL as an oscillator, at very high powers. The scheme, MCWFEL, increases the small signal gain by a factor larger than 10, provides a smooth gain curve and decreases or eliminates the possibility of frequency chirp due to nonoptimum electron beam energy injection.

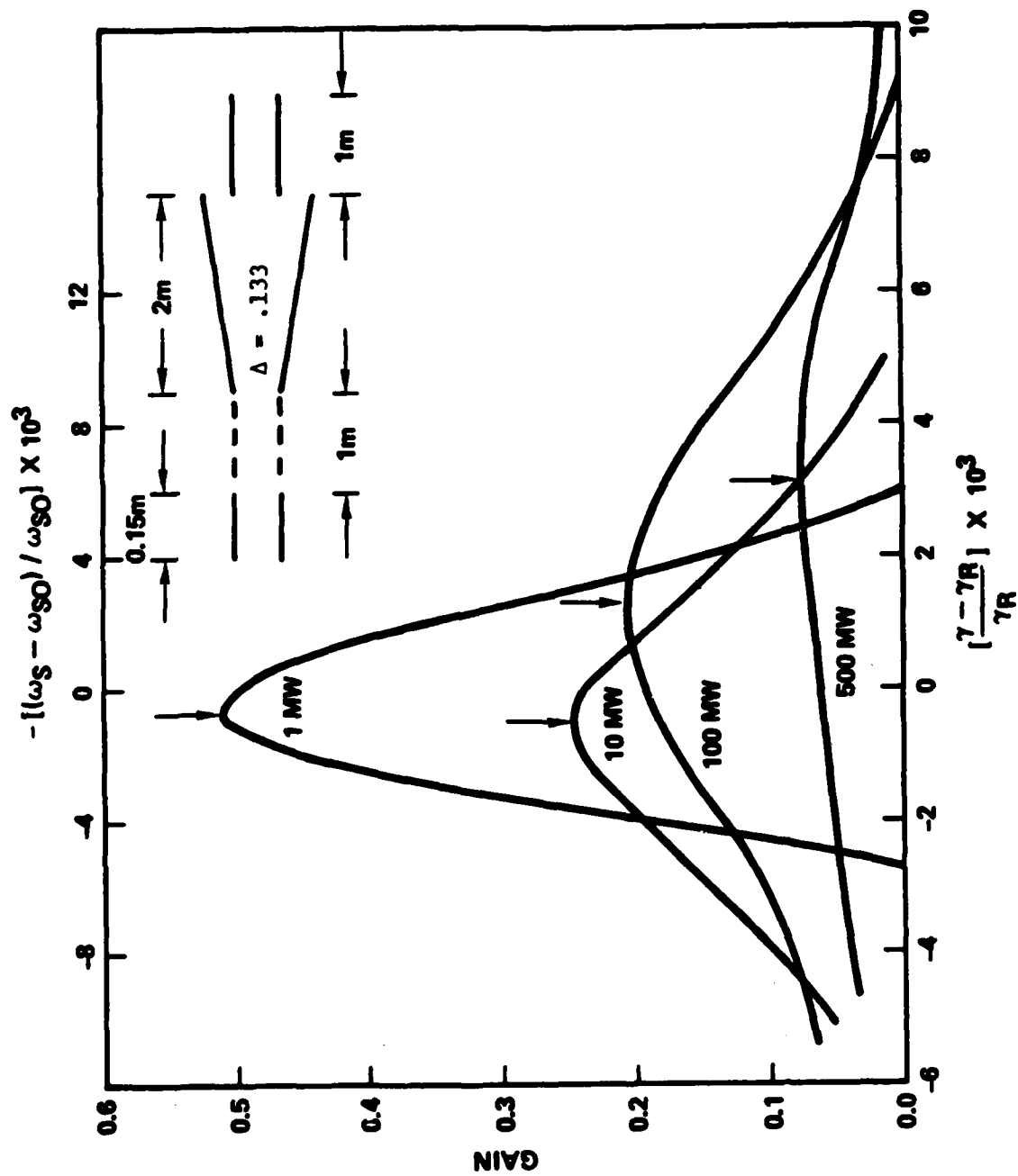


Figure 27: Multicomponent FEL Gain Spectrum for Different Input Powers.

## VI SUMMARY

To summarize the previous sections, we have developed under the contract a set of advanced diagnostics for free electron laser use. The diagnostics have been utilized to compare FEL performance with theory. This diagnostic system included the use of spontaneous emission to absolutely calibrate the energy of the accelerator. The electron current was monitored with Faraday cups. The relative positions of the electron and photon beams were determined by the use of insertable screens. Inventions were necessary to measure emittance and gain. To measure the emittance, beam profile as a function of focusing quadrupole current was determined using a fiber optic array system. This system provides both multiple single shot and time averaged emittance. To measure the optical gain, sufficient discrimination between the input pulse and the gain signal was achieved by the use of an etalon in the reflective mode. This was coupled with time averaging electronics to form the most sensitive gain measurement system developed under any of the tapered wiggler FEL programs.

Use of these diagnostics uncovered large changes in the day-to-day emittance of the linac. Moreover, sensitivity of the FEL to emittance changes appeared to be large (in agreement with theory). Small signal gain of the FEL with a constant wiggler was measured to be 1.5%. Large signal gain with a tapered wiggler was found to be less than 3%.

The key result of this effort is not any one measurement but the conclusion of the ensemble: for all measurements to date FELs work according to theory. To further parameterize the FEL and perhaps uncover any subtle discrepancies it will be necessary to get a more reproducible accelerator particularly as regards emittance. If necessary, this can be achieved by use of an emittance filter. The goal of FEL development can be addressed through a limited set of technology issues such as:

- Linac development (smaller emittance, higher currents)
- Wavelength scaling
- Optical beam quality and power handling
- Multicomponent wiggler optimization



As regards the last issue, modeling results have been very encouraging but still await experimental verification. The other issues will require a more extended development program but are expected to yield to a reasonable effort. In conclusion, while more definitive data would be advantageous, all results to date are very encouraging for FELs as a high power tunable source of visible radiation.

#### ACKNOWLEDGEMENT

The TRW FEL team would like to express its appreciation to Neil Norris, the scientists, and the linac operators of E. G. & G, Santa Barbara, for their dedicated efforts in making this program a success. We would further like to thank R. Miller for his help in the beamline design and emittance diagnostic and K. Halbach for his suggestion of the SmCo wiggler design.

## REFERENCES

1. H. Boehmer, M. Z. Caponi, J. Edighoffer, S. Fornaca, J. Munch, G. R. Neil, B. Saur, and C. C. Shih, Phys. Rev. Lett., 48, 140 (1982)
2. TRW HERALD Progress Report, ONR Contract No. N00014-80-C-0580, October, 1981.
3. Halbach, K., presented at International Conference on Charged Particle Optics, Giessen, West Germany, September 8-12, 1980.
4. Miller, R., SLAC Pub-91-Revision 1, 1981.
5. M. Z. Caponi and C. Shih, Proceedings of IEEE Int. Conf. in Plasma Sci., Santa Fe, NM, May 18-21, 1981, and Bull. APS, 26, 919 (1981).
6. C. Shih and M. Z. Caponi, Accepted for publication in Phys. Rev. A., 1982.
7. N. Kroll, P. Morton, and M. Rosenbluth, Physics of Quantum Electronics, Vol. 7, edited by S. F. Jacobs, et al., (Addison-Wesley, Reading, MA) 1980.
8. The possibility of simultaneously enhancing the TWFEL large signal and small signal gain was first suggested by J. Edighoffer.

## APPENDIX I

### Time Structure of FEL Output

The free electron laser output is derived from the contributions of the input laser and the radiation of the electrons. These contributions have different time structures as calculated below.

If the laser input pulse is a Gaussian in time with length  $\sigma_L$  and the electron pulse is Gaussian in time with length  $\sigma_e$ , then,

$$P_L \sim e^{-t^2/\sigma_L^2} \quad (\text{Input Laser Power})$$

$$i_e \sim e^{-t^2/\sigma_e^2} \quad (\text{Electron Beam Current}).$$

In the small signal input case, the optical gain signal is proportional to the input laser power and is given by

$$S \sim P_L i_e \propto e^{-t^2 \left[ \frac{1}{\sigma_L^2} + \frac{1}{\sigma_e^2} \right]} = e^{-t^2 \left[ \frac{\sigma_e^2 + \sigma_L^2}{\sigma_e^2 \sigma_L^2} \right]}.$$

If  $\sigma_L = 100 \sigma_e$ , as it is in this experiment, then

$$S \sim e^{-t^2 \left[ \frac{1 + 10^{-4}}{\sigma_e^2} \right]}.$$

This implies that  $\sigma_s$ , the length of the optical gain signal, is smaller than  $\sigma_e$  by 5 parts in  $10^5$ . In the large signal input case, the optical gain signal is proportional to the square root of the input laser power and is given by

$$S \sim \sqrt{P_L} i_e e^{-t^2 \left[ \frac{\sigma_e^2 + 2\sigma_L^2}{2\sigma_e^2 \sigma_L^2} \right]}.$$

This implies for  $\sigma_L = 100 \sigma_e$  that  $\sigma_s$  is smaller than  $\sigma_e$  by 10 parts in  $10^5$ .

The radiation due to bunched electrons is proportional to the current squared [third term in Appendix II], so it is proportional to

$$i_e^2 \propto e^{-t^2 \left[ \frac{2}{\sigma_e^2} \right]} = e^{-t^2 / (\sigma_e / \sqrt{2})^2}.$$

Therefore, its length in time is a square root of 2 shorter. This though makes little difference experimentally as pulses shorter than the electron pulse can not be distinguished. Thus, in all cases, all pulses, except the input laser pulse, can be considered equal in length to the electron pulse.

## APPENDIX II

### Definition of Gain and Power Out of FEL

The calculation of the optical field after the interaction with the free electron laser is shown here. The electric field of the input laser is written as  $E_L e^{i\phi}$ . The radiation field radiated by the electrons is written in two terms: one for the spontaneous unbunched radiation present with or without the input laser ( $e'_s e^{i\phi'}$ ), and the second for the "spontaneous" radiation emitted by the bunched electrons  $e_s e^{i(\phi+\psi)}$ , where the bunching is induced by the input laser field.  $\psi$  is the average phase of the bunched electrons relative to the optical field and is closely approximated by the standard  $\psi$  for a taper wiggler. Adding these fields together, squaring and averaging over random phases gives the power after the interaction in the free electron laser. That is

$$P_{out} = \frac{1}{(2\pi)^2} \int_0^{2\pi} d\phi \int_0^{2\pi} d\phi' \left[ E_L e^{i\phi} + e'_s e^{i\phi'} + e_s e^{i(\phi+\psi)} \right]^2$$

$$= E_L^2 + 2 E_L e_s \cos \psi + e_s^2 + e'^2_s .$$

The first term is the input laser power; the second term is the work done by the electrons on the optical field and is generally called gain in most modeling, the third term is the power radiated by the bunched electrons as they pass through the wiggler; and the last term is the spontaneous radiation from randomly phased electrons. The input laser bunches a fraction of the electrons, the amount of bunching in the small signal limit being proportional to the square root of the input power. The power radiated by the third term is proportional to the square of the amount of average bunching. In the standard free electron laser, the electrons enter the laser with random phase and are bunched by the optical field as mentioned above. Thus the third term is proportional to the input laser field. It has the same dependence on the input field as the second term and the same time structure. It can be distinguished by polarization techniques and because it is proportional to the electron current squared. All the other terms are linearly proportional to current. If the gain is defined as power out minus power in divided by power in, then this term will be included in what is called gain.

Gain measurement experiments are not capable of distinguishing term two from term three except by the dependence on input current and perhaps by polarization measurements. Our measurements included both terms. The results presented include both terms although calculations indicate that the third term is two orders of magnitude smaller than the second.

## APPENDIX III

### A Fully Time Resolved High Resolution Optical Fiber Profile Monitor

The profile monitor consists of a single plastic clad polysilicate optical fiber, wound on a mandrill to form a ribbon of sixty tightly packed loops (see Figure III-1 and III-2). One section of the circumference of this ribbon is placed to intercept the electron beam, with the rest of the ribbon bent out of the way. This section of the ribbon is oriented at the Cherenkov angle with respect to the electron beam. In this way, the Cherenkov radiation produced by the passage of the electrons through the fibers is launched in an efficient and highly directional manner. If the electron pulse is short compared to the optical transit time through one loop of the ribbon, then the ribbon acts as a multi-tapped delay line, converting position to time of arrival. Since Cherenkov radiation is a linear function of the electron current, there is no saturation problem with this interaction. The emitted light is guided along the fiber to a fast photomultiplier outside the noise environment of the accelerator. The dispersion of the optical fiber over short distances is not a problem as long as the dispersion is less than the transit time of a single loop. The output of the photomultiplier gives a signal as a function of time which is proportional to the electron current as a function of position.

The optical fibers are prone to radiation damage by the passage of the electron beam through them. To a large extent, this damage can be controlled by heating the fibers so that they anneal as the damage is done. This was done by placing a heat lamp near the fibers.

### DESCRIPTION AND RESULTS

The optical fiber has an inner diameter of 125  $\mu\text{m}$  of polysilicate surrounded by a plastic cladding with an overall diameter of .016". It has an index of refraction of 1.47, giving a Cherenkov angle of  $39^\circ$ . The fiber was wound on a 6" diameter mandrill giving a 2.35 ns channel separation. The electron pulse from the EG&G linac is approximately 50 psec, much shorter than the channel separation. There were 60 turns on the mandrill for a total width of 1.15" or .48 mm per channel. Thirty feet of fiber were left at one end to prevent the possibility of reflection from interfering with the desired signal. The other end has a 200' run to the photomultiplier tube. The output gives a very clean, low noise,



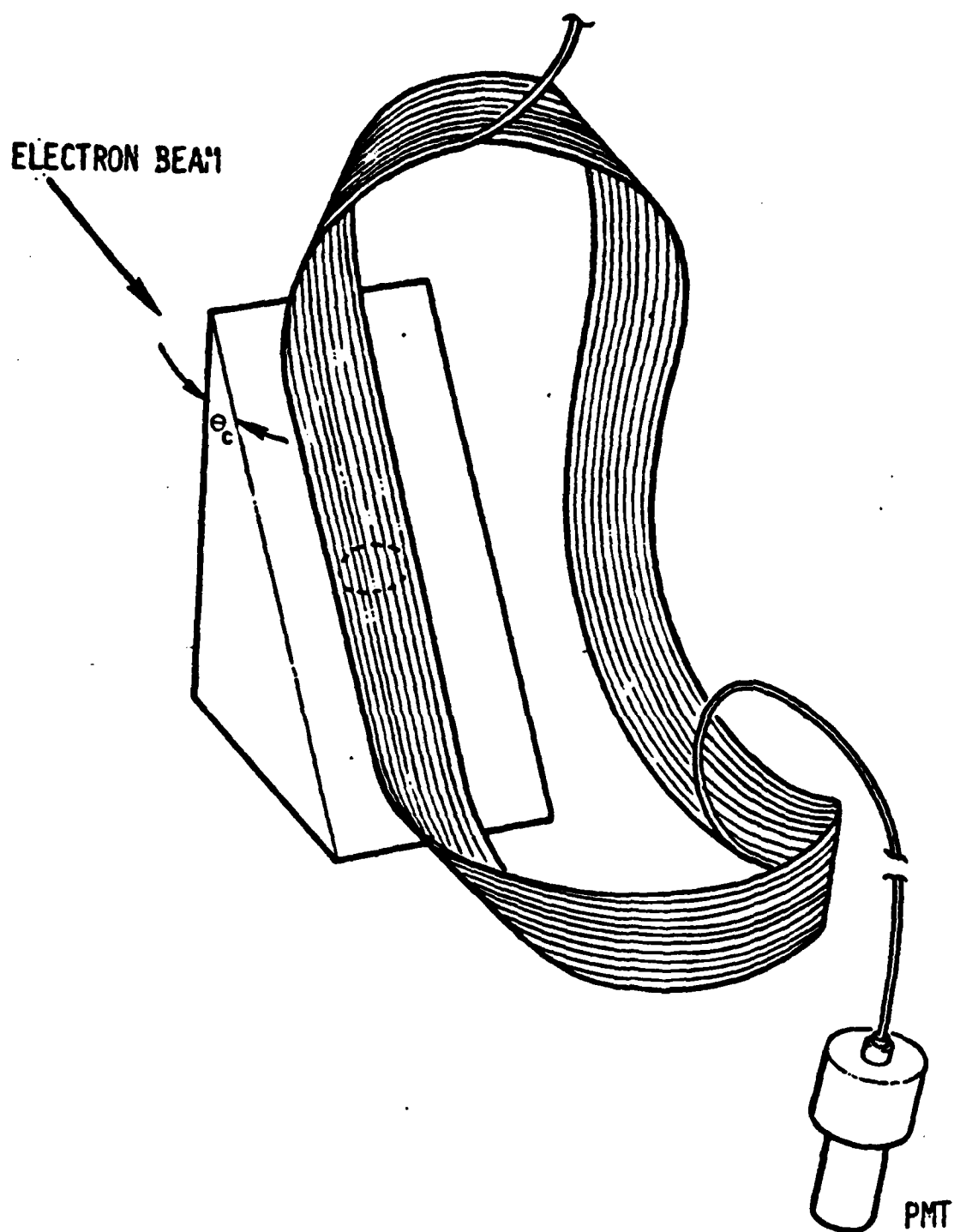


Figure III-1. Schematic of the Optical Fiber Array

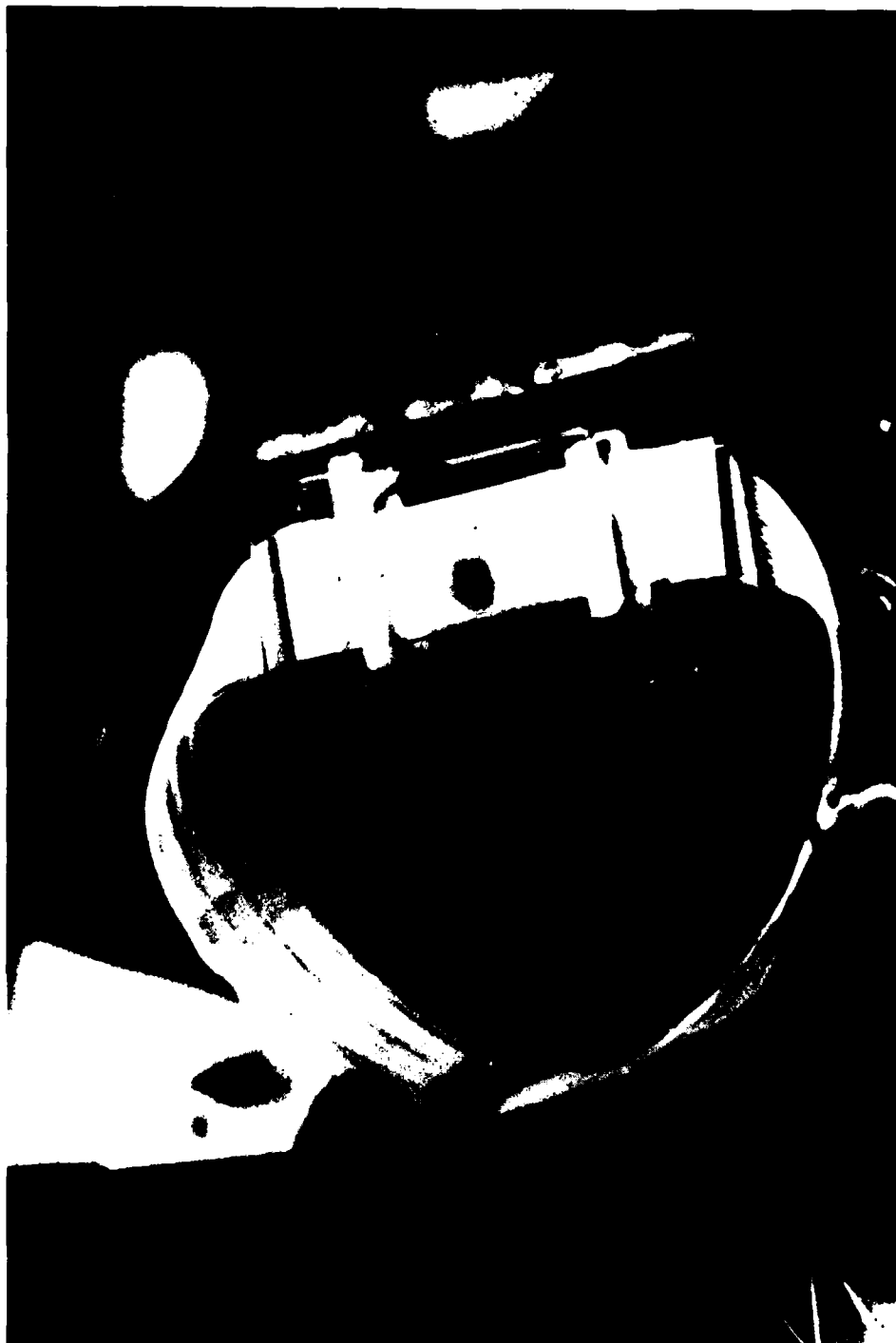


Figure III-2. Photograph of the Fiber Array

reproducible signal. A single shot output is shown in Figure III-3. This shows a full width at half maximum of 35 ns which corresponds to 7.1 mm or 14 channels. The edge of the detector array is evident by the shoulder. Figure III-4 shows the result of averaging over 10 shots and Figure III-5 shows the result of averaging over 10 shots and eliminating the high frequency ripple. The spectrometer magnet used with this detector has a momentum dispersion of 7.67 mm/% ( $\Delta P/P$ ) and a resolution of .19%. That resolution of the position detector is three times better than necessary for this spectrometer.

The linac was operated at 0.75 nanocoulombs/pulse and 60 pulses/sec or 450 nAmp average current at 25 MeV. With the use of a heat lamp, the attenuation from one end of the fibers to the other end was kept below 30%. This was measured by observing the peak electron amplitude as the spectrometer magnet current was varied (see Figure III-6). It is easy to plot this attenuation function, so that the data can be properly corrected for it.

#### CONCLUSION

A very inexpensive high resolution single shot position monitor has been built and is been used as an integral part of the TRW free electron laser program. The resolution can be further increased by using smaller diameter fibers. If the average beam current is higher so that the damage to the fibers is more severe, then multiple fibers layed side by side of different lengths could be used instead.



Figure III-3. Repetitive Single Shot Traces from the Fiber Array

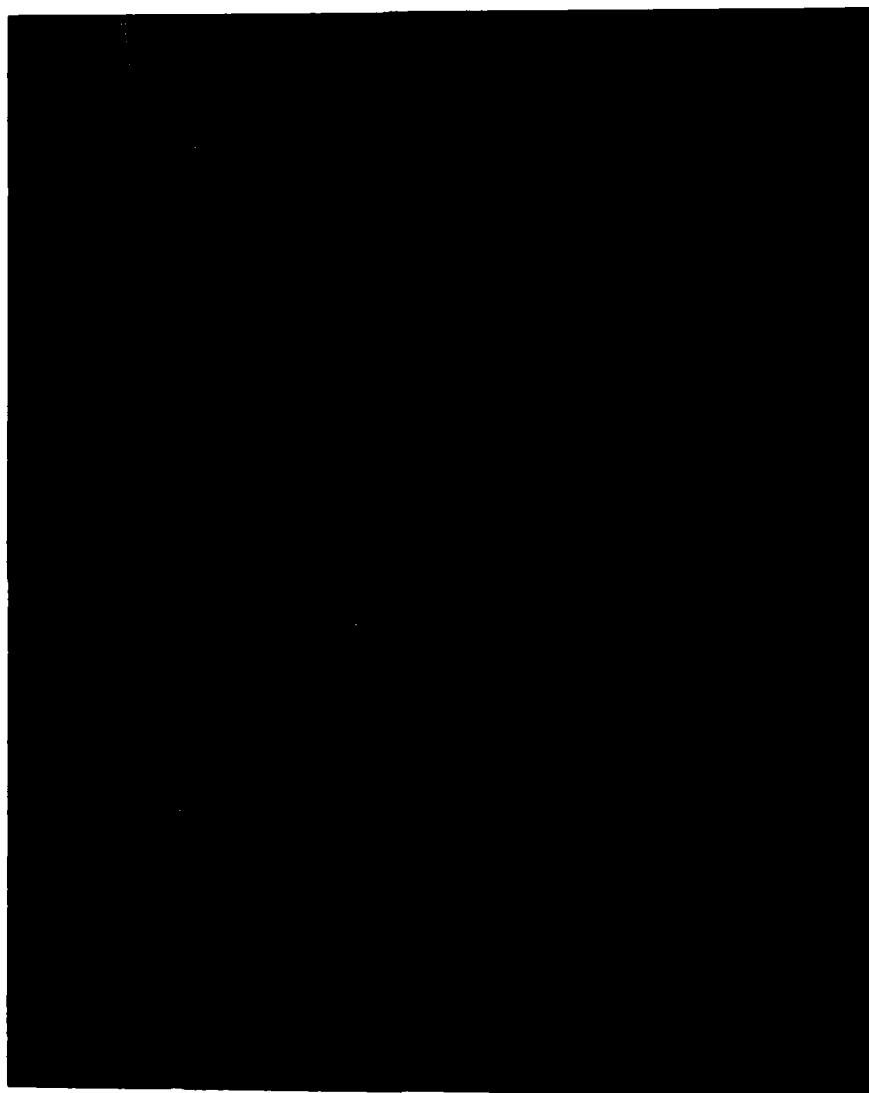


Figure III-4. Ten Shot Average of the Electron Spectrum

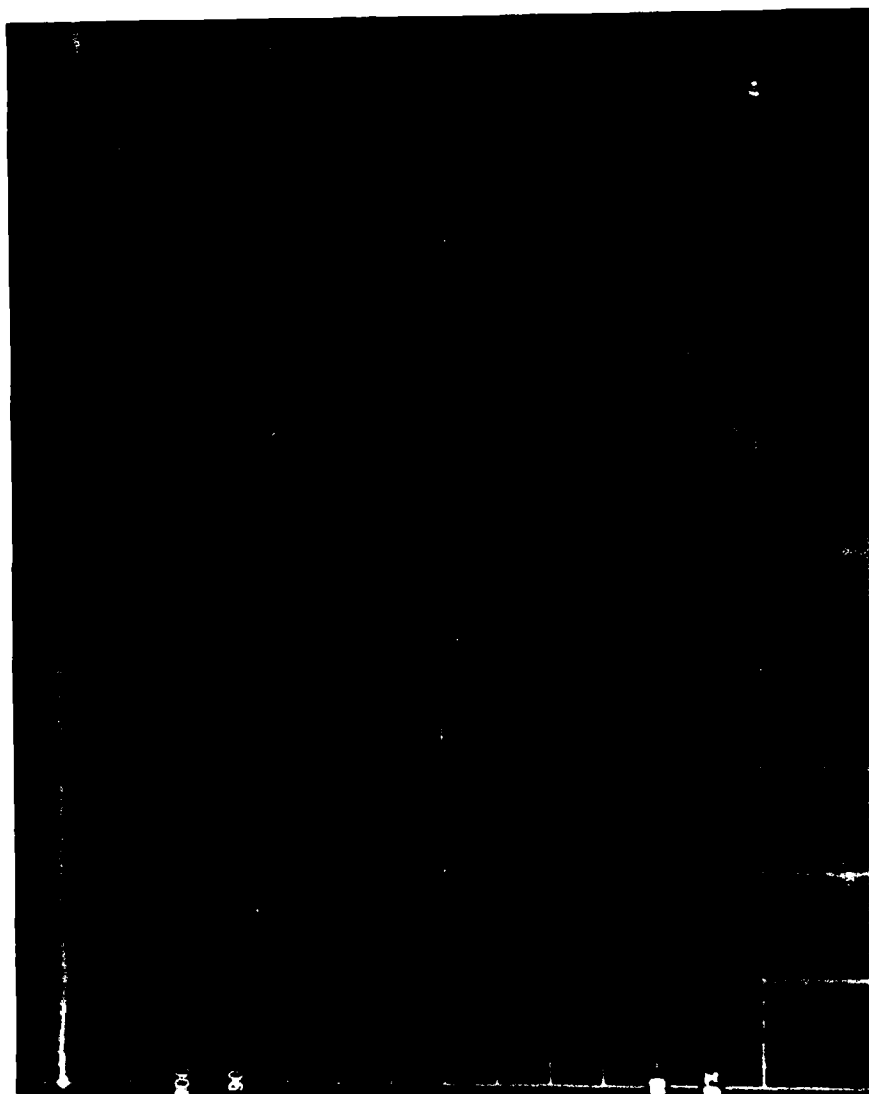
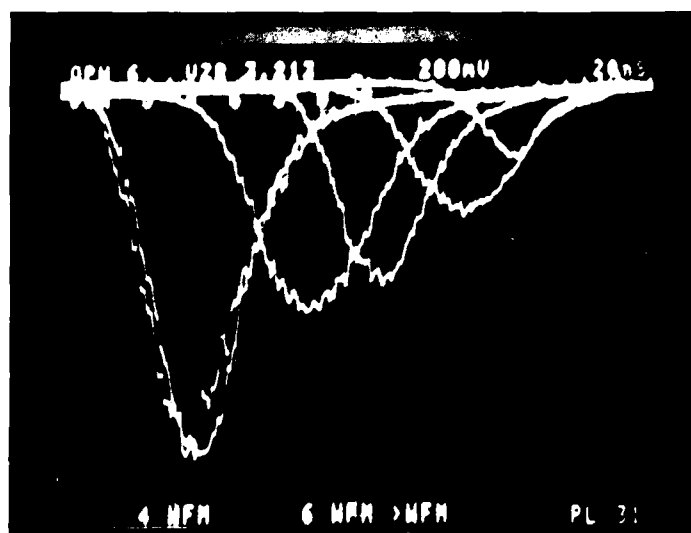
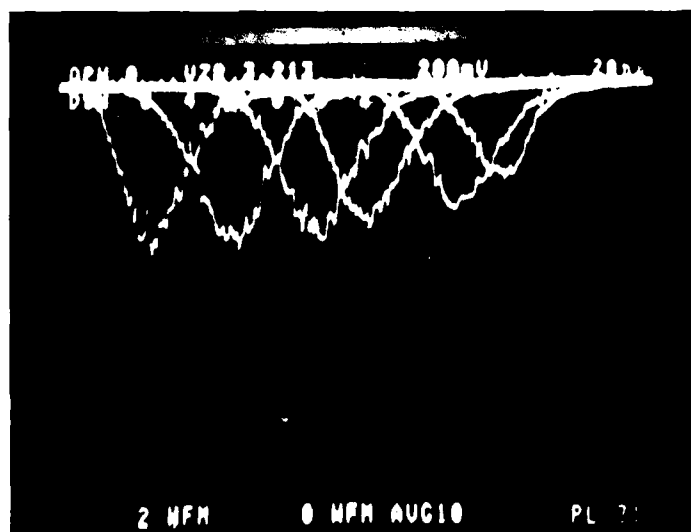


Figure III-5. The Electron Spectrum Smoothed to Eliminate the High Frequency Ripple

# ATTENUATION OF OPTICAL FIBER ARRAY



WITHOUT HEAT LAMP



WITH HEAT LAMP

FIGURE III-6: Signal vs Position of the fiber array showing attenuation due to fiber damage and repair by annealing.

## APPENDIX IV

### Emittance Measurement Technique

An Emittance Measurement using one Quadrupole, a Drift and a Profile Monitor.\*

The emittance measurement relies on the fact that the width of the profile is a function on the strength of the quadrupole, and that this function depends on emittance. So by measuring the functional dependence of the profile on the quadrupole current, the emittance can be determined. Using simple first order electron beam transport equations will show how to extract this information. Refer to SLAC PUB-91-Revision 1 for a description of electron beam transport. This matrix formulation allows one to take a vector representing the electron's transverse position and angle at the beginning of a transport section, multiply it by a transport matrix to get the electron's final position and angle. The transport matrix for a drift region is

$$\begin{bmatrix} 1 & L \\ 0 & 1 \end{bmatrix}, \quad \text{where } L \text{ is the drift length.}$$

The transport matrix for a quadrupole magnet is

$$\begin{bmatrix} \cos k_q L' & \frac{1}{k_q} \sin k_q L' \\ k_q \sin k_q L' & \cos k_q L' \end{bmatrix}, \quad \text{where } L' \text{ is the length of the quadrupole,}$$

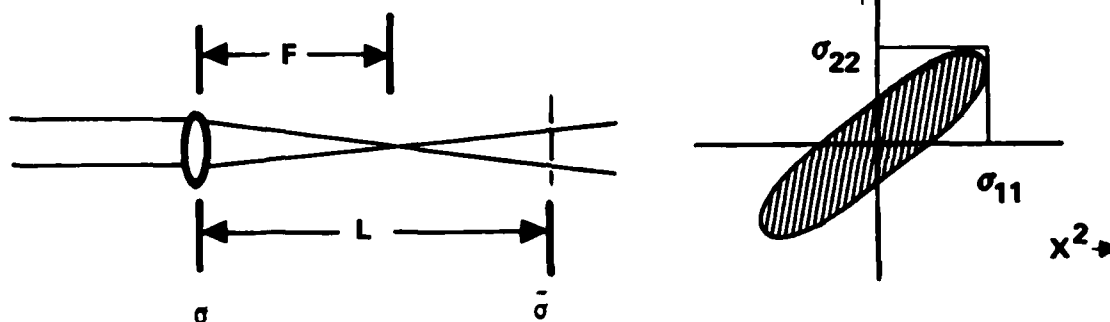
$k_q^2 L' = 1/f$ , where  $f$  is the focal length of the quadrupole. If the length of the quadrupole is short compared with the focal length, then the thin lens approximation can be used where  $k_q L' \rightarrow 0$ . That is the transport for quadrupole matrix becomes

$$\begin{bmatrix} 1 & 0 \\ 1/f & 1 \end{bmatrix}.$$

\*The idea was obtained from Roger Miller at SLAC.



The system looks like this



If the profile of the beam is a Gaussian phase ellipse which is represented by a  $\sigma$  matrix at the center of the quadrupole, then the phase ellipse at the position of the profile monitor,  $\bar{\sigma}$ , can be determined by beam transport. The variance matrix is

$$\sigma = \begin{vmatrix} \sigma_{11} & \sigma_{12} \\ \sigma_{21} & \sigma_{22} \end{vmatrix}$$

$\sigma_{11}$  is the variance of the width,  $\sigma_{22}$  is the variance of the divergence, and  $\sigma_{21} = \sigma_{12}$  is the covariance of the width with the divergence. Note the square root of the area of this phase ellipse is the emittance, by definition. Back to calculating  $\bar{\sigma}$  as a function of  $1/f$ , where  $1/f$  is proportioned to the current in the quadrupole. Substituting  $K$  for  $1/f$  and standard transport matrix formulation

$$\begin{aligned} \bar{\sigma} &= \begin{vmatrix} 1 & L \\ 0 & 1 \end{vmatrix} \begin{vmatrix} 1 & 0 \\ K & 1 \end{vmatrix} \sigma \begin{vmatrix} 1 & K \\ 0 & 1 \end{vmatrix} \begin{vmatrix} 1 & 0 \\ L & 1 \end{vmatrix} \\ &= \begin{vmatrix} 1 + LK & L \\ K & 1 \end{vmatrix} \sigma \begin{vmatrix} 1 + LK & K \\ L & 1 \end{vmatrix} \end{aligned}$$

Finishing multiplying through:

$$\begin{aligned} \bar{\sigma}(1/f) &= \begin{vmatrix} (1 + LK)^2 \sigma_{11} + L(1 + LK)(\sigma_{12} + \sigma_{21}) + L^2 \sigma_{22} & (1 + LK) 1/f \sigma_{11} + (1 + LK) \sigma_{12} + LK \sigma_{21} + L \sigma_{22} \\ (1 + LK) K \sigma_{11} + LK \sigma_{12} + (1 + LK) \sigma_{21} + L \sigma_{22} & K^2 \sigma_{11} + K(\sigma_{12} + \sigma_{21}) + \sigma_{22} \end{vmatrix} \end{aligned}$$

The first element of  $\bar{\sigma}$  is

$$\begin{aligned}\bar{\sigma}_{11} &= (1 + KL)^2 \sigma_{11} + L (1 + KL) 2 \sigma_{12} + L^2 \sigma_{22} \\ &= K^2 L^2 \sigma_{11} + K (2L \sigma_{11} + 2L^2 \sigma_{12}) + (\sigma_{11} + 2L \sigma_{12} + L^2 \sigma_{22})\end{aligned}$$

Experimentally,

$$\bar{\sigma}_{11} = A K^2 + BK + C, \quad \text{where } A, B \text{ and } C \text{ are determined experimentally}$$

by measuring  $\sqrt{\sigma_{11}}$  as a function of current (K) in the quadrupole. The emittance is the square root of the area of the ellipse,  $\epsilon = \sqrt{(\sigma_{11} \sigma_{22} - \sigma_{21}^2)}$ . Therefore,  $\sigma_{11}$ ,  $\sigma_{22}$  and  $\sigma_{21}$  must be determined from A, B and C in order to calculate the emittance from the measured profiles. This is accomplished by noting the different functional dependence of  $\bar{\sigma}_{11}$  on different elements of the  $\sigma$  matrix, (i.e. the quadratic dependence depends only on  $\sigma_{11}$ ). Comparing the above equations it is obvious that  $A = L^2 \sigma_{11}$  or  $\sigma_{11} = A/L^2$ .

Also  $B = 2L \sigma_{11} + 2L^2 \sigma_{12}$ , (noting that  $\sigma_{12} = \sigma_{21}$ )

Therefore  $\sigma_{12} = B/2L^2 - A/L^3$

Finally  $C = \sigma_{11} + 2L \sigma_{12} + L^2 \sigma_{22}$ ,

so solving for  $\sigma_{22}$  gives

$$\sigma_{22} = C/L^2 - B/L^3 + A/L^4$$

Now we are ready to solve for the emittance\*

$$\epsilon = \sqrt{\sigma_{11} \sigma_{22} - \sigma_{12}^2}$$

Substituting for  $\sigma_{11}$ ,  $\sigma_{22}$  and  $\sigma_{12}$  and reducing, yields.

$$\epsilon = \frac{1}{2L^2} \sqrt{4AC - B^2}$$

In conclusion, by fitting a parabola to the variance of the profile width as a function of current in the quadrupole, the simple formula above gives the emittance. It takes but a few minutes to measure the width of the profile at four or five current settings and then calculating the emittance using a programmable calculator.

\* Note the complete phase ellipse, including the angle is determined at the position of the quadrupole.

## APPENDIX V ACCELERATOR DEVELOPMENT

This section describes a six-month program performed by the Boeing Aerospace Company to develop accelerator technology for short wavelength free electron laser research. The major program objective was to design critical linear accelerator system components to produce a long pulse, high current beam with the optical quality and stability necessary for submicron FEL oscillator demonstration experiments.

The major accelerator technology tasks performed during this program were:

- 1) High current injector design; space charge dominated magnetic optics, subharmonic prebunching design,
- 2) Long pulse RF power modulator design, and
- 3) Design, fabrication and installation of electron beam diagnostics and transportation system.

### 1.1 HIGH CURRENT INJECTOR

To achieve electron beams with the optical quality necessary for FEL demonstration experiments several improvements to the BAC LINAC injector have been proposed. As part of the completed program a reconfigured injector was designed and is illustrated in Figure 1.1-1. These completed design modifications include:

- Gun extraction magnetic optics and full Helmholtz field for injector (described in Section 1.1.1).
- Addition of a 119 MHz (24th subharmonic) prebunching cavity and relocation of the 476 MHz (sixth harmonic) cavity (described in Section 1.1.2).

#### 1.1.1 Injector Magnetic Optics

Axial magnetic field is used to maintain equilibrium Brillouin flow in the injector. Care must be taken in three areas:

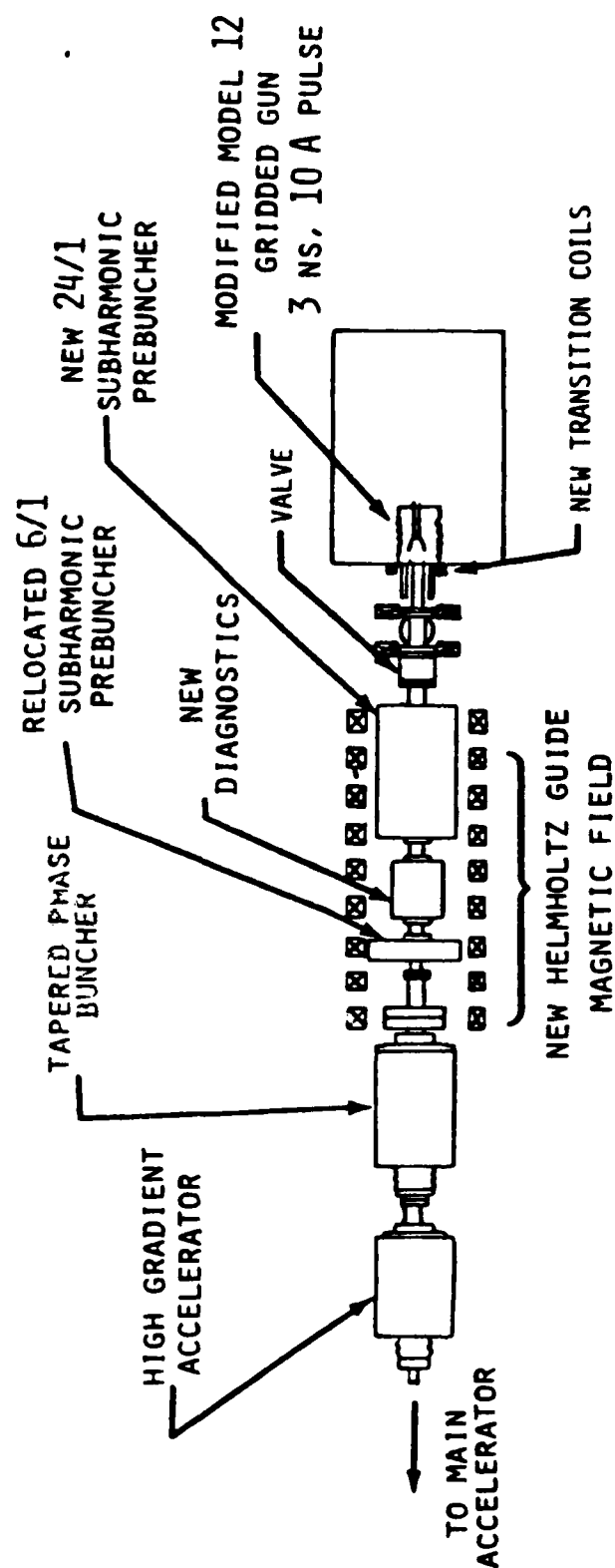


Figure 1.1-1 High Current Injector Design

- Control of beam space charge during transition from the field-free gun to the uniform field region,
- Suppression of radial oscillations by matching beam bunching with axial field increases, and
- Radial compression of the bunched beam at the entry to the S-band buncher to minimize emittance growth due to transverse cavity fields.

The transition between the gun and the first prebuncher cavity is customarily accomplished with a steel jacketed Glazer lens. In the present injector an 8-cm aperture lens 23 cm from the gun is used to form a waist at the subharmonic buncher gap. The ETP code was used to model flow from the proposed small cathode Model 12 through the lens and into the buncher. The results are shown in Figure 1.1-2. The lens action is principally on the outside rays in the buncher since these rays experience the strong radial gradient near the lens body. The outer rays crossover as the beams forms a waist and substantial beam heating occurs. The calculated emittance growth is from  $4.7\pi$  mr-cm ( $\epsilon_N = 0.01$  cm rad) to  $70.7\pi$  mr-cm ( $\epsilon_N = 0.15$  cm-rad). Note that although in this run, the large number of trajectory crossovers may have caused a simulation problem, the results clearly indicate excessive emittance growth.

As an alternative to the discrete lens approach, a quick transition to a uniform solenoid field was postulated. ETP was used to model flow in a 3-cm radius solenoid placed 6 cm from the gun anode. A reverse current loop was placed between the anode and the solenoid to buck out axial field in the anode-cathode gap. The trajectory plot is shown in Figure 1.1-3. The flow remains relatively laminar although the radial compression in the last 10 cm probably should be avoided. The calculated final emittance was  $19.3$  mr-cm ( $\epsilon_N = 0.04$  cm rad).

The hardware design for this type of transition is shown in Figure 1.1-4. The solenoid coil is designed to slip over the first short vacuum section. The coil will be fabricated in water-cooled, hollow copper tubing to handle the  $\sim 100$ A current. The coil will be somewhat adjustable in axial position for fine tuning of the optics. Two small Helmholtz coils straddle the vacuum tee. These coils form a transition to the main Helmholtz field that begins at the 119 MHz prebuncher cavity.

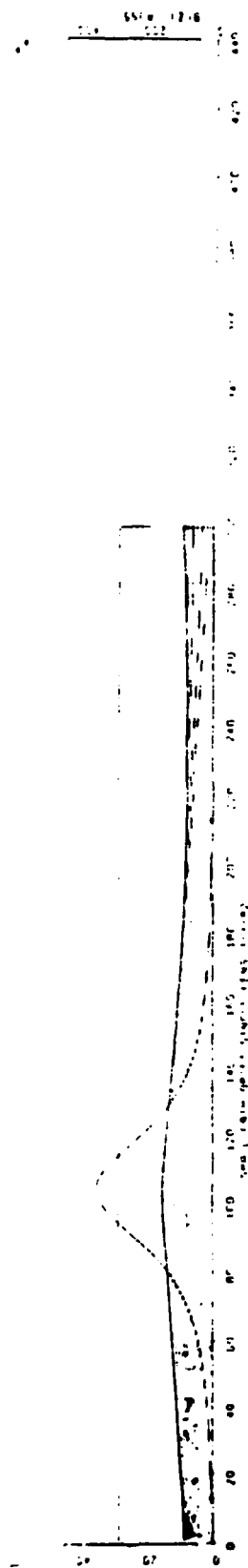


Figure 1.1-2. ETP Plot for Modified Gun with Single Lens

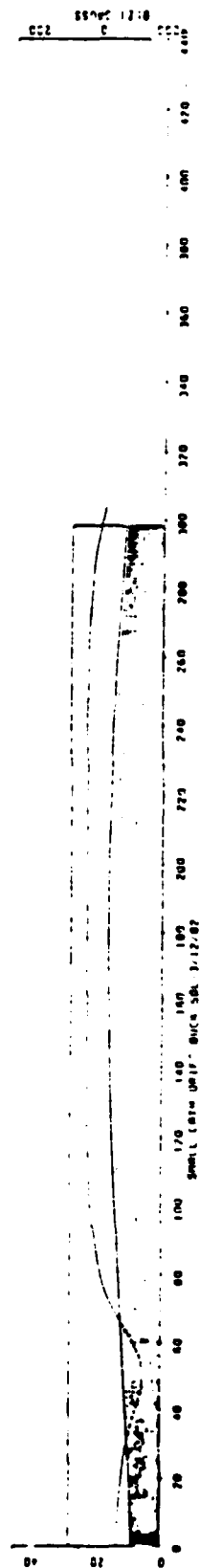


Figure 1.1-3. ETP Plot for Modified Gun with Solenoid

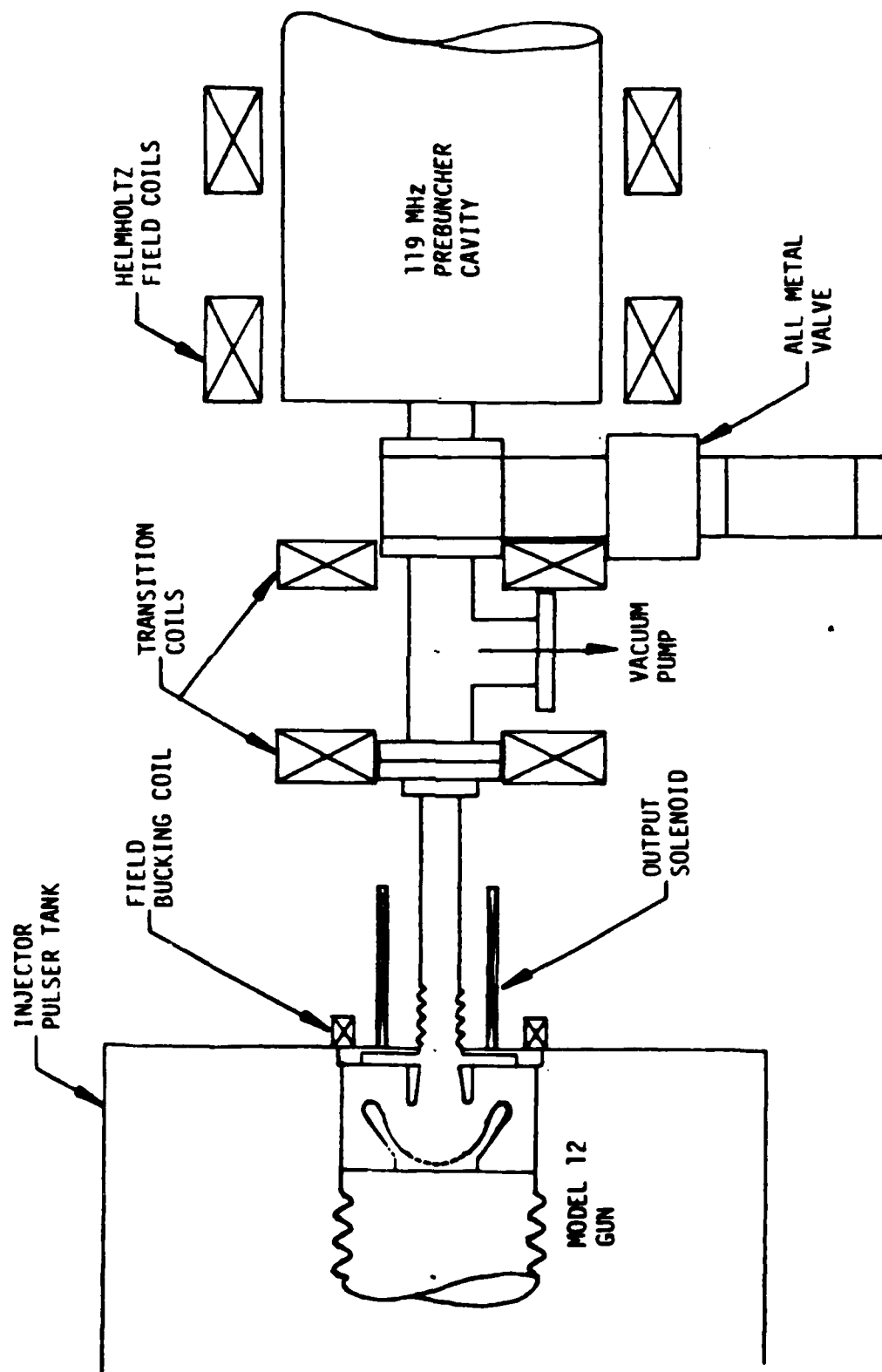


Figure 1.1-4. Magnetic Optics at Gun Output

Optimization of the magnetic field design is performed with a Boeing-developed microcomputer code. This code also performs a paraxial ray analysis to calculate beam envelopes in the injector. Beam current ramping by the bunchers is included. This code has been directly compared with ETP for the case shown in Figure 1.1-2, agreement in calculation of beam radii was within 10% throughout the full axial distance. This code was used to tune the magnetics in the design, Figure 1.1-3. A plot of the magnetic field from the gun cathode to the 24/1 buncher is shown in Figure 1.1-5. The corresponding beam envelope plot is shown in Figure 1.1-6. The field in the cathode-anode gap can be held comparable with the earth's field. The beam assumes an equilibrium radius of  $\sim 1.2$  cm with a minimum of scalloping.

Magnetic optics in the remainder of the injector are relatively straightforward. Magnetic field variation in the Helmholtz field is available to equilibrate with current increases developed by the prebunching cavities. Tuneability will be built in to allow experimental optimization. Beam spot size and radial motion monitors incorporated in the injection diagnostics will assist the tuning process. Linear accelerators are notorious for not optimizing at the design axial field.

The magnetic field capability will range from 500 gauss at the 119 MHz prebuncher to 2K gauss at the entrance to the tapered phase velocity buncher. An example of the field profile through the injector is shown in Figure 1.1-7 with the envelope plot shown in Figure 1.1-8. The beam radius is held large through the main portion of the injector then compressed to 0.5 cm radius at the entrance to the S-band section. Off axis particles experience time varying transverse fields in the coupler and first cavity of this section. The effect is similar to a lens with focal length varying with particle phase. This area has been identified as a potential problem for emittance growth for high charge micropulses in the SLAC collider injector, Reference 1.1.1. Two-dimensional trajectory analysis tasks outlined in the technology support task will address this problem in detail.

#### 1.1.2 Injection Bunching Design

The injector design utilizes multiple subharmonic gaps similar to high current single bunch designs at Argonne, Reference 1.1.2 and SLAC, Reference 1.1.3.



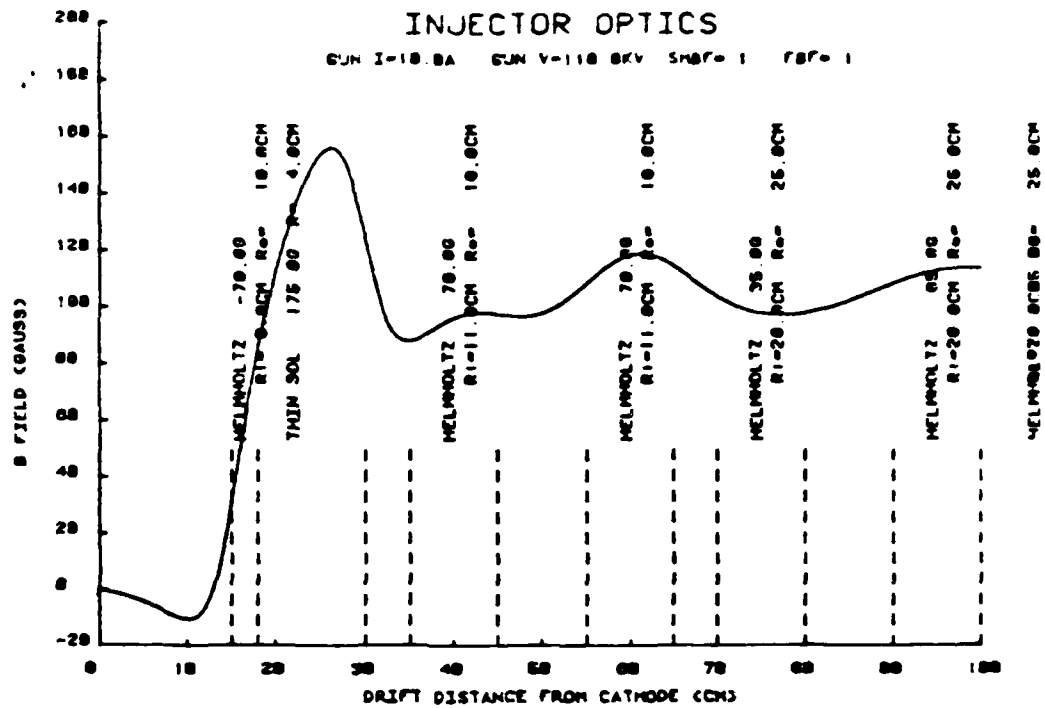


Figure 1.1-5 . Magnetic Field Bridging Gun Cathode and 24/1 SHB

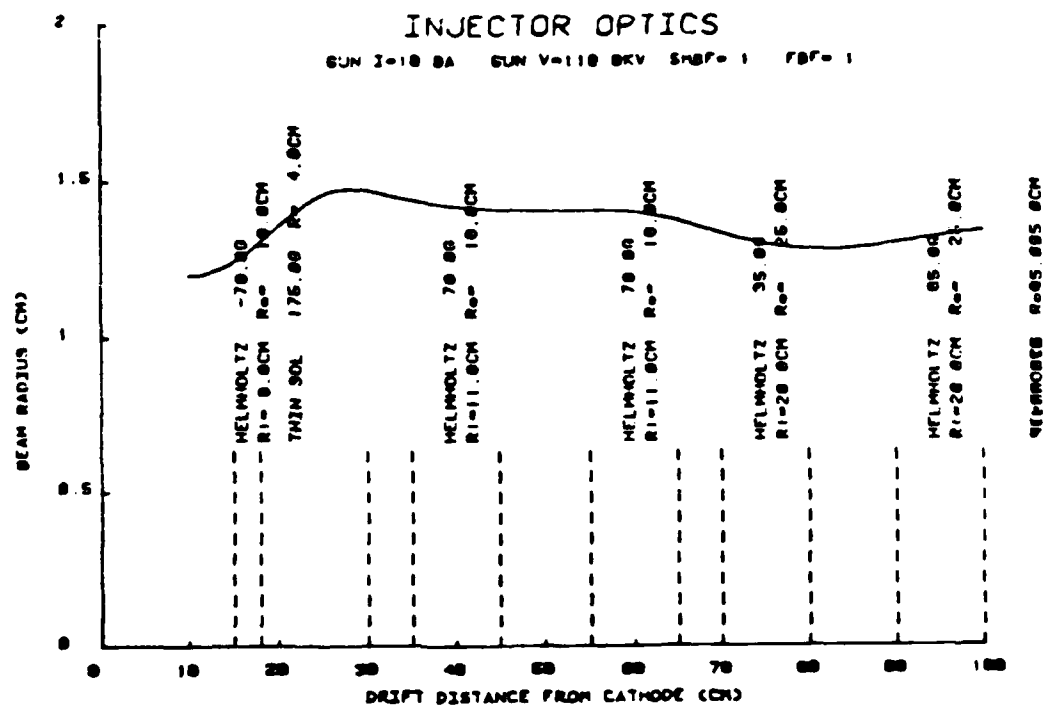


Figure 1.1-6 . Beam Radius Between Gun Cathode and 24/1 SHB

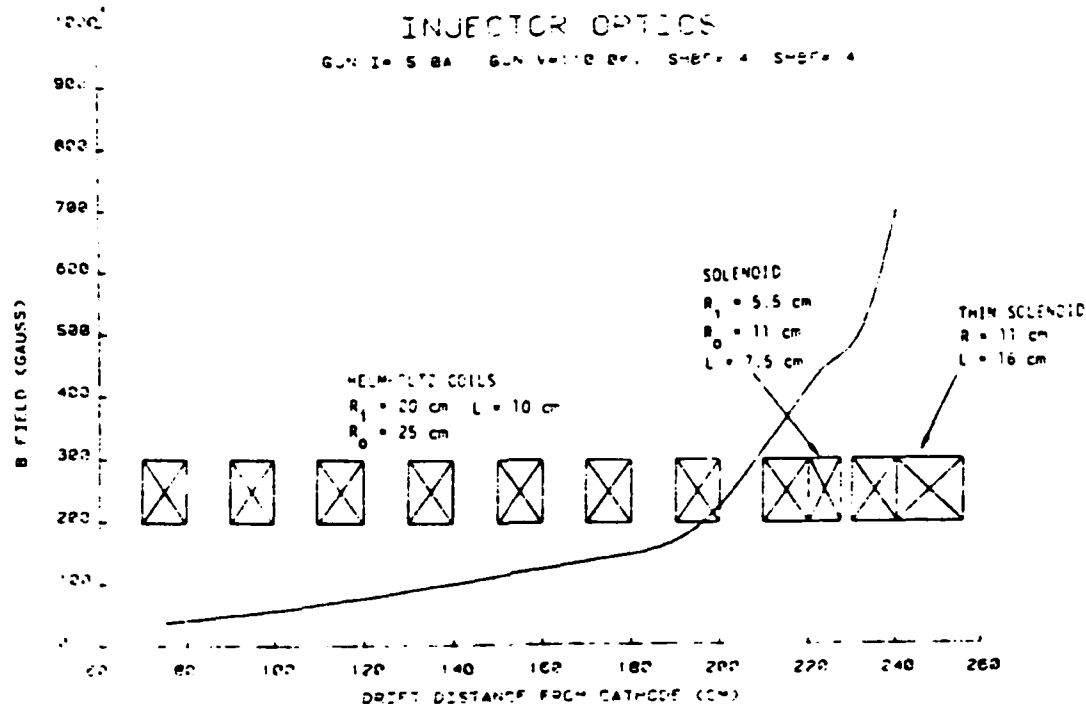


Figure 1.1-7. Magnetic Field Profile Between the 24/1 SHB and the TPV Buncher

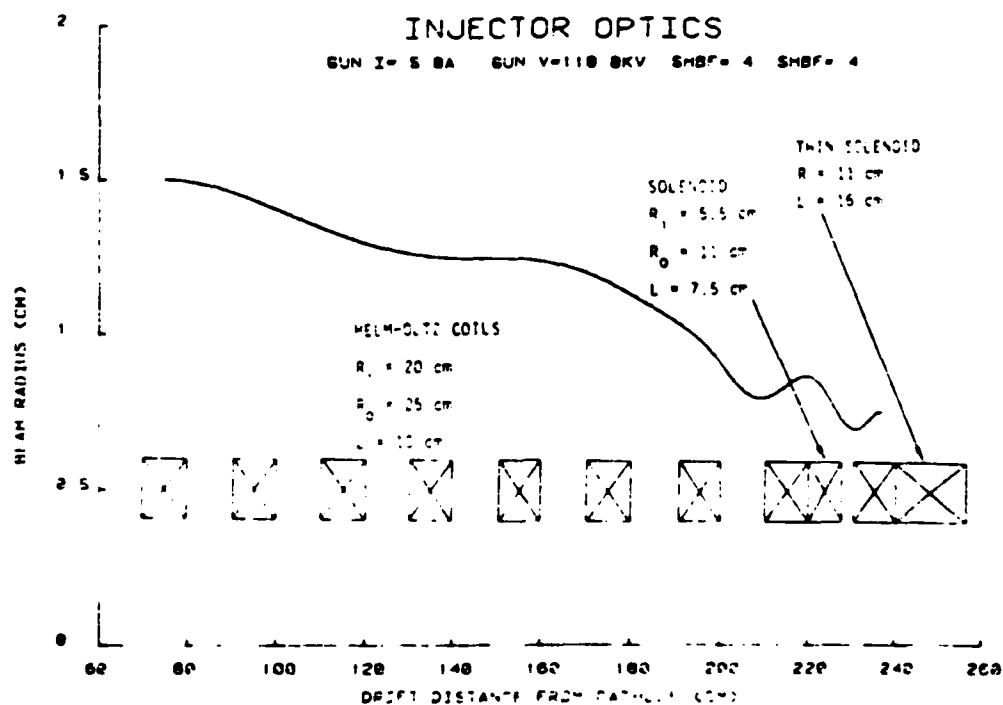


Figure 1.1-8 Beam Radius Profile Between the 24/1 SHB and the TPV Buncher

The design objective is to bunch 2.5 nanocoulombs into a single S-band bunch without measureable satellite current. The input gun pulse is assumed to be 3 ns full width and adjustable in current to 10A. Two subharmonic prebunchers are used. The first operates at the twenty-fourth subharmonic 119 MHz, and the second at the sixth subharmonic 476 MHz.

The interaction of gated gun pulses and standing wave cavity bunchers has been analyzed using the code ORBIT developed by W. J. Gallagher. The beam model used is that described by Tein (Ref. 1.1.4). The derivation of the equation of motion appropriate to prebunching is given in Ref. 1.1.5. The approach is to consider the beam as a series of charged discs, ascribing all the beam charge to N discs per wavelength. The potential inside a cylinder may be obtained, which conveniently eliminates infinities which would otherwise occur as discs approach each other infinitesimally close. The force on any disc may then be determined by summing over all other discs, and its motion calculated. This model, which permits crossovers, is considered realistic, since the discs are, in fact, "porous" from the electronic standpoint.

The code was used to parameterize the cavities individually. The longitudinal bunch width is plotted as a function of drift distance for several gap voltages in the 119 MHz cavity in Figure 1.1-9. Also shown is a sample of the code output. The input current is divided into 21 discs, each disc is assigned a current so that the assembly represents a gaussian waveform containing the total charge noted (5 nanocoulombs). The disc positions are plotted in units of accelerator fundamental phase. The parametric calculations show that, for high charge, small bunchers are obtained with short drift distances and high gap voltage. The target phase width for the first prebuncher is  $4\pi$  of the fundamental. This width is the acceptance of the sixth subharmonic cavity. From the graph, gap voltage of ~40 kV and drift distances of 100-140 cm are required. The sixth subharmonic cavity is placed at this location. A graph of bunching performance for this cavity is shown in Figure 1.1-10. These calculations are shown for both 5 nanocoulombs and 2.5 nanocoulombs. The target phase width in this calculation is  $\pi/2$  of the fundamental since this width will assure 1% energy spread in the accelerator.

The lower charge beam is clearly preferred. Some additional form of bunching may be required for the high charge bunch. Multiple cavity traveling wave prebunchers have been used at Argonne to develop single microbunches of 40 nanocoulombs. Beam emittance has

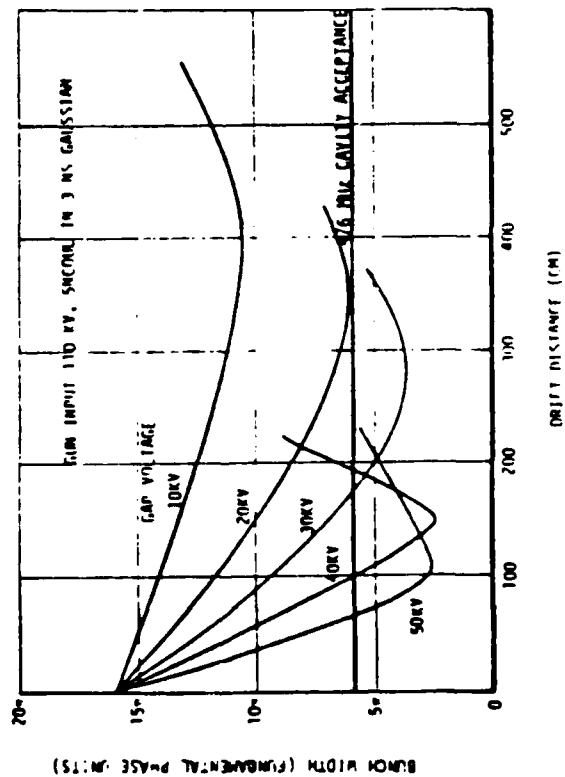
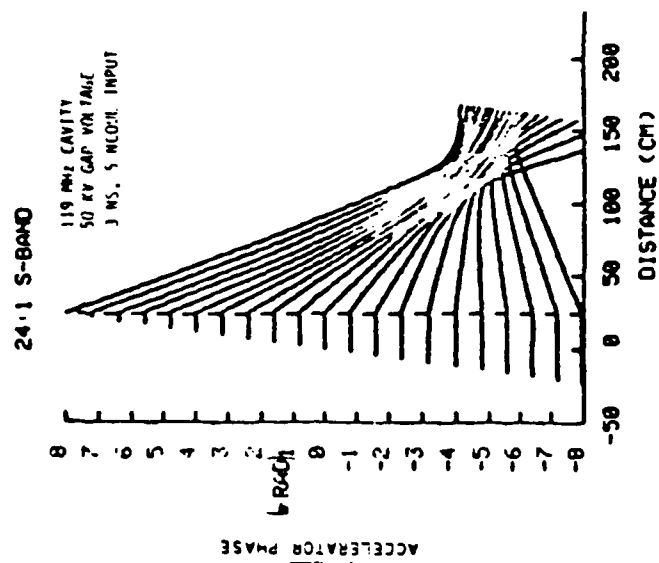


Figure 1.1-9 . 119 MHz Cavity Bunching Plots

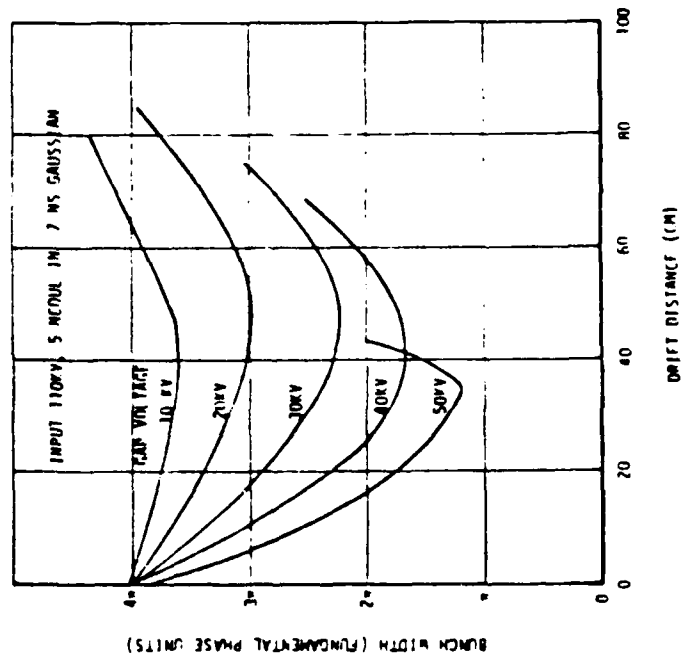
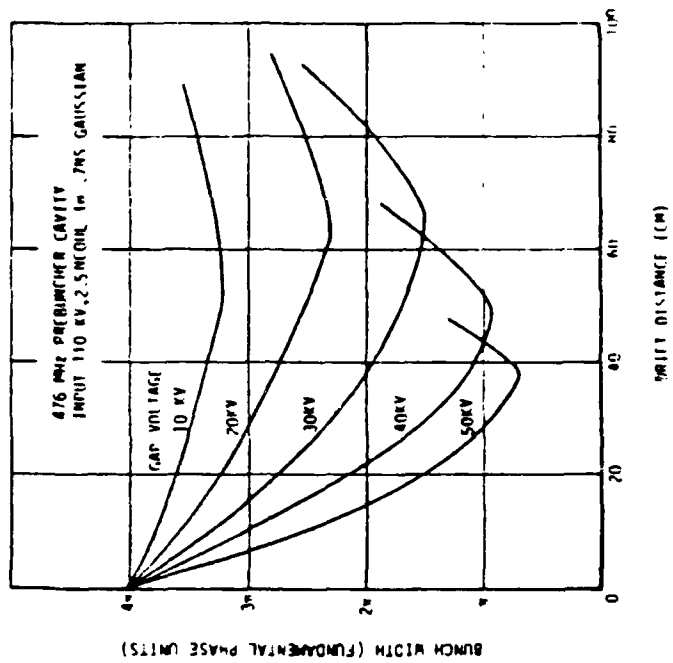


Figure 1.1-10. 476 MHz Cavity Bunching Plots

been large, however, with the high charge bunchers. Our approach has been to look for designs that allow the bunch to form quickly at the entrance to the high gradient accelerator so that space charge heating is minimized. One rather simple way to specify such bunching is to run the Orbit code backwards. An ideal width beam is assembled at the input to the accelerator. In Figure 1.1-11, the beam is "injected" into the code and allowed to freely expand due to its own space charge. The distance to  $4\pi$  phase width becomes the 476 MHz cavity location and the phase and Y encoding of the particles becomes the prescription for the cavity voltage. The prescription is not too far from a phase shifted sine wave at 50-70 kV amplitude.

The prebuncher cavities are combined in a design shown in Figure 1.1-12. A 2.5 nanocoulomb, 3 nanosecond gaussian pulse is injected at 110 kV. The 119 MHz cavity is operated at 30 KV and the 476 MHz cavity at 20 kV. Ninety percent of the charge appears in a fundamental phase width of  $\pi/2$  at the accelerator entrance. This charge will be further bunched by the accelerator to 15-18 degrees of phase, Ref. 1.1.6. The equivalent peak micropulse current is 150-170 amperes.

## 1.2 LONG PULSE RF MODULATOR

To provide the pulse length ( $>50$  ns) and the RF phase ( $<3$  pS spacing error) and amplitude ( $<1\%$  unflatness) stability required to support proposed FEL experiments several modifications must be made to the BAC modulator. These modifications include:

- Additional PFN stages for a 50  $\mu$ sec pulse length and optimized design parameters for flatness
- Upgrade switch thyratrons for long pulse reliability
- Replace pulse transformer and associated equipment with long pulse rated hardware.

Upon consideration of the RF stability necessary to achieve the energy spectrum requirement for FEL application it appears that phase modulation and output power variation of the klystron is one of the principal causes of deterioration of the beam quality.

Thus, to ensure RF phase and amplitude stability

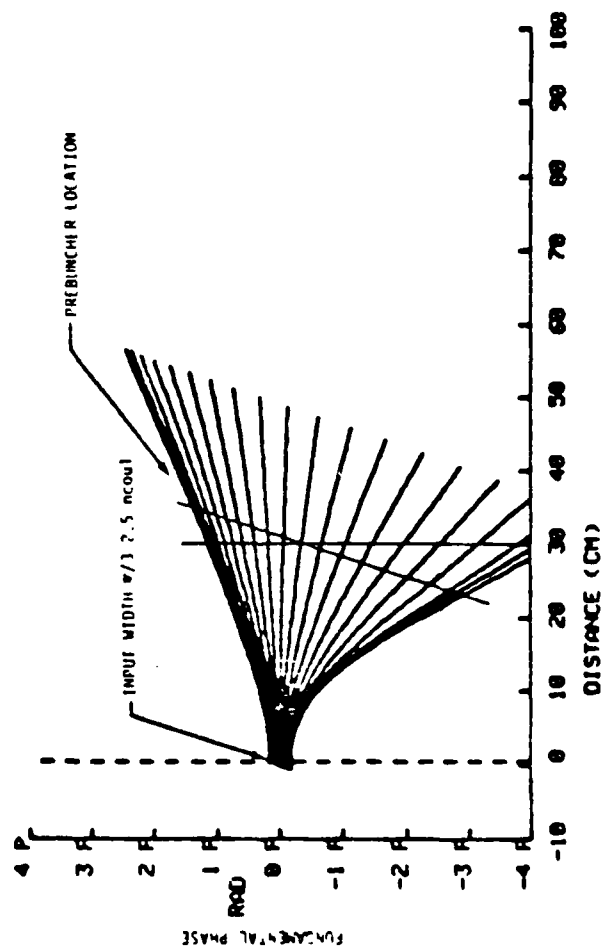
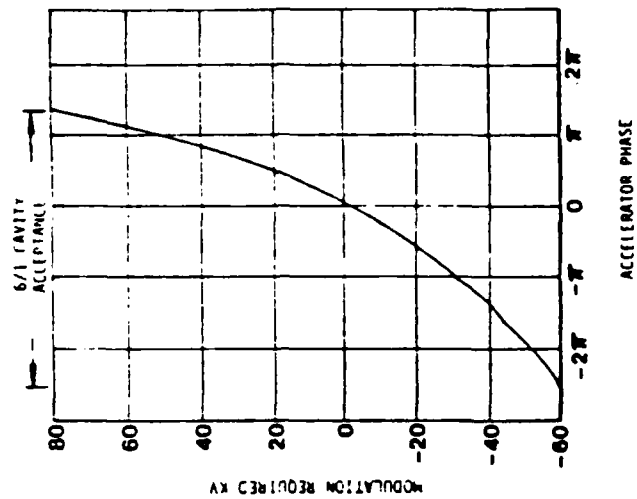


Figure 1.1-11. SPACE CHARGE EXPANSION OF 2.5 N.C. BUNCH

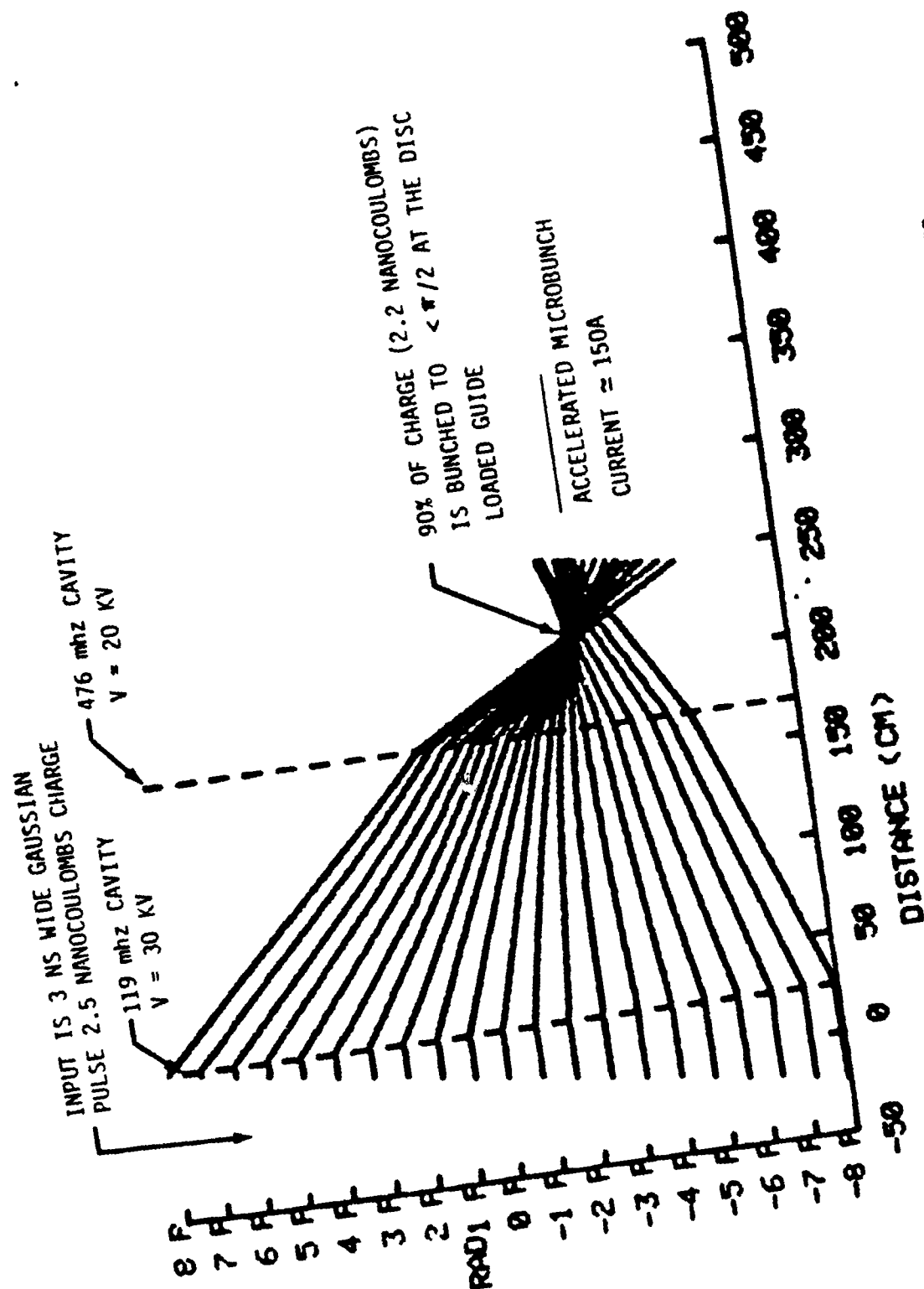


Figure 1.1-12. MULTIPLE SUBHARMONIC CAVITY PREBUNCHER



- Additional active amplitude and phase control circuitry will be added to the klystron drive.

This task involves participation of the LANL RF and magnet design group AT-5 as a subcontractor. The LANL staff has unique capabilities in long pulse klystron modulators and in the development of fast response active control circuits.

In addition to the assistance from LANL (contracted for on the basis of their experience in the design of the PIGMI modulator), a separate study was undertaken on the discharge pulse from the pulse forming network (PFN).

The design of the PFN was based on the following considerations. The switching thyatron voltage rating and the intended high voltage klystron pulse establishes the pulse transformer (PT) turns ratio (N) and the primary circuit voltage. The energy per pulse to be delivered to the klystron therefore determines the PFN network capacity ( $C_T$ ) taking into account the voltage doubling due to resonant charging through the charging choke. The PT turns ratio and klystron impedance also determines the network characteristic impedance ( $\sqrt{L_T/C_T}$ ) and thereby the total network inductance. Since it is desirable to use all capacitors of the same value, the number of sections (n) can be determined on the basis of the pulse rise time ( $t_R$ )

$$t_R = n^{1/3} \sqrt{L_T C_T} \quad (1)$$

The thirty section PFN designed on the above basis, (with  $C = 0.12 \mu f$   $L = 8.4 \mu h$ ) was analyzed. The voltage pulse as a function of time across an 8.4 ohm load is shown in Figure 1.2-1. This computation was performed on a computer. The program used was a Boeing-developed transient circuit analysis program (Ref. 1.2.1). The network analysis showed that a pulse of 55  $\mu s$  duration (with 45  $\mu s$  having a quarter percent regulation) would be obtained. Initial overshoot was eight percent and fall-time 4  $\mu s$ . Post-pulse ripple amplitude was 4 kV maximum. The design is considered acceptable although further studies on the effect of component tolerances are planned..

As part of their subcontract, LANL has completed the initial modulator design and submitted it for review. Several of the critical system component (thyatron, driver,

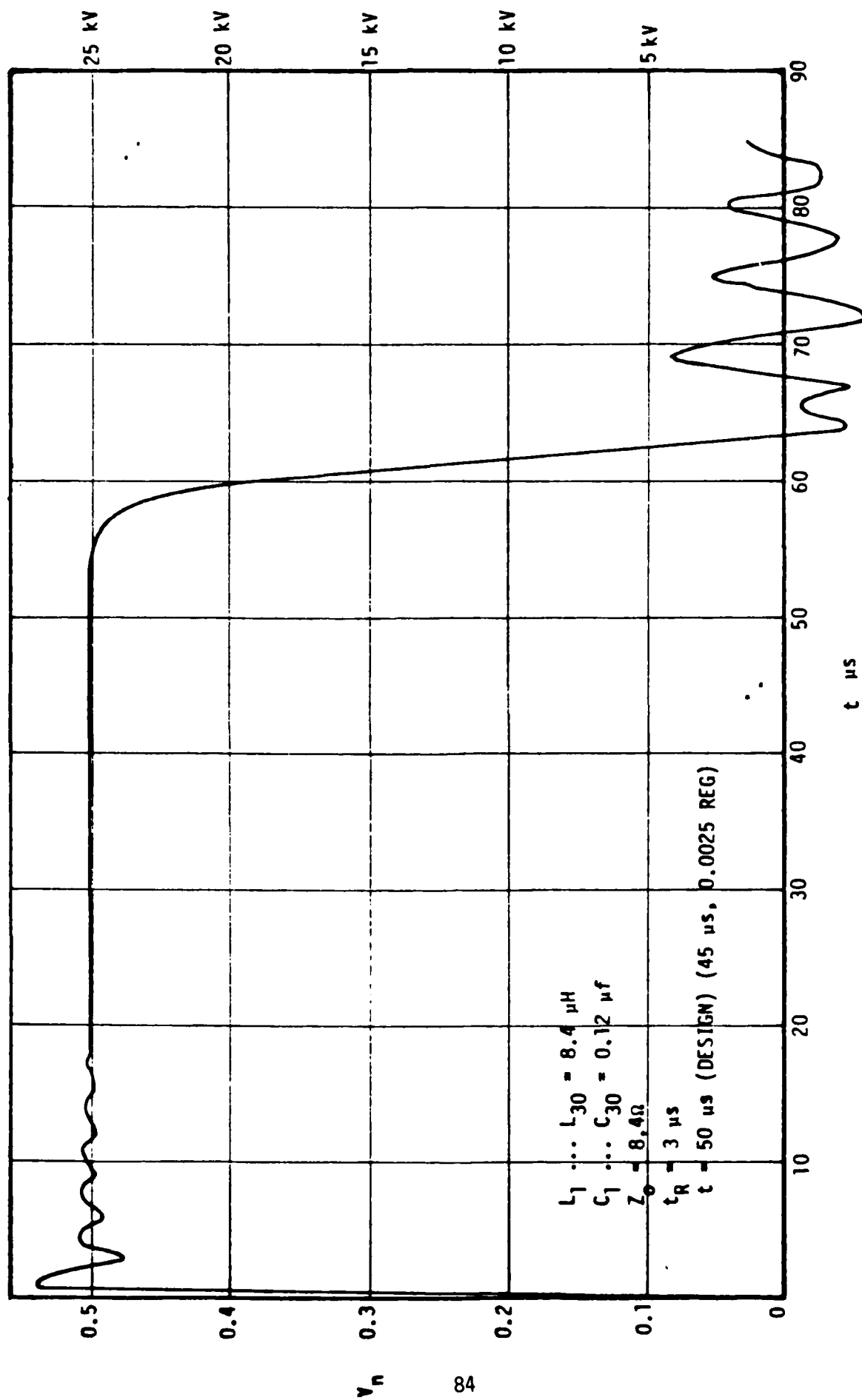


Figure 1.2-1. Voltage Pulse Versus Time

pulse transformer, charging choke and capacitors) specifications have been finalized. Orders have been placed for the following equipment:

- Switching Thyatron, 50 kV, 5 kA, 8A average anode current, 100 sec pulse 50 PPS (ITT 8479)
- Thyatron Drive, including bias supplies for grid and auxillary grid, and cathode heater supply (Impulse Electronics TA-4K)
- Thyatron Drive board, fiber optic coupler (Impulse Electronics TD-3K)
- Pulse transformer assembly compatible with Thomson-CSF 2015B Klystron, 11:1 ratio, 250 kV at 240 amp output, 100  $\mu$ sec pulse at <1% droop, 50 pps continuous duty (Stangenes).
- Charging Choke, 3.4 h  $\pm$  10% at RMS current 13A, average current 7.6A, peak current 27A, 20,000 hours life cycle. Charging duty 200 pps at 10  $\mu$ s, 100 pps at 50  $\mu$ s for a 3.6  $\mu$ f capacitor bank to 50 kV, DC supply side 24 kV (Stangenes)
- Oil Tank for 20 MW, 20- kW, TV 2015B klystron and pulse transformer assembly, top plate machined to accept klystron socket, high voltage 50 kV, 2.5 kA bushing for pulse input, feed throughs for current and voltage monitors and cone reset power supply.

### 1.3 BEAMLINE AND FEL DIAGNOSTICS

The beamline instrumentaton was upgraded during this program with the addition of four fluorescent tuning screens and position monitors. The location of these instrumentation stations (shown in Figure 1.3-1) were chosen to coincide with waist locations in the beam optics. A long drift leg has been added straight ahead of the LINAC to measure beam emittance. A digital system was installed for displaying the beam position in real-time.

The beam handling system leg immediately upstream of the FEL wiggler has been shortened to decrease the sensitivity of electron beam waist location on magnetic quadrupole setting.

#### 1.3.1 Electron Beam Transport

The success of FEL experiments depends on proper preparation of the electron beam before it enters the wiggler. Among the parameters controlled by the beamline are the entrance conditions (position, orientation) to the wiggler and the phase space

## 8 ACCELERATOR DIAGNOSTIC UPGRADE



**Figure 1.3-1 . Layout of Boeing LINAC Diagnostics**

configurations. The entrance conditions are important to maintain overlap with the laser beam through the wiggler, and phase space control is important to minimize the equivalent energy spread of the electron beam.

The beamline is taken to be that transport region from the exit of the Linac to the entrance of the FEL wiggler. The arrangement of the experimental hall strongly influenced the layout depicted in Figure 1.3-1. From the end of the Linac (A-leg) the beam is translated through an achromatic dogleg (B-leg) to a direction parallel to the Linac centerline (C-leg) into the FEL interaction region.

Experience with FEL experiments shows that electron beamline tuning is a time consuming process and may not always be successful. To eliminate these tuning problems the beamline configuration has been re-examined and modified. The A- and B-legs have been left intact. The major change in the transport system is shortening the C-leg. Calibrations showed that phase space control was more sensitive to quadrupole settings the longer the C-leg was. Shortening this part of the beamline will aid the tuning process by reducing their sensitivity.

Several beam monitoring stations have been inserted into the beamline. These stations contain beam viewing fluorescent screens and beam position indicators. These devices will enable the linac operator to 'walk' the beam down the beamline while controlling phase space orientations by viewing the screens.

An important feature of the A-leg is that it will be used to measure the emittance of the beam as it exits from the linac. An algorithm for this measurement has been derived which involves measuring the beam size on the first viewing screen as a function of an upstream quadrupole setting.

The beamline calculations were performed using the computer code TRANSPORT (Ref. 1.3.1). The fitting capabilities of this code were extensively employed to locate magnet beam handling elements along with their settings to achieve the various beamline features. After the beamline was established, the TURTLE (Ref. 1.3.2) code was used to ray-trace the entire system. The results provide beam profiles and scatter plots of the beam at each of the monitor stations in the beamline. In this way a comparison of the predicted and observed beam characteristics can be made in order to aid in the beam turning procedure.

### 1.3.2 FEL Diagnostics

The electron beam position is monitored at four locations along the beamline (Figure 1.3-1). Two different measuring techniques are employed to determine beam position and size:

- Fluorescent screens, and
- Ferrite-loaded Stripelines

A drawing of the vacuum chamber and the beamline position monitor and viewing screens is shown in Figure 1.3-2. The viewing screens are moved into and out of the electron beam by means of an air actuated vacuum feed-through translator. The targets are oriented at a 45-degree angle relative to the beam centerline. Separate TV cameras monitor each viewing target through a quartz window.

The fluorescent screens can thus be used to walk the beam through the transport optics to set focal lengths, position and size at the FEL entrance. The precision of these screens for measuring beam spot size and position is  $\leq 0.5$  mm.

Non-interrupting position monitors at the same locations as the viewing targets are used to assure centering of the beam in the magnetic optics. These finite loaded stripline monitors have a time resolved sensitivity to measure beam position with 0.5 mm. Each monitor is made up of four electrodes, two each along the horizontal and vertical axis of the plane perpendicular to the beam pipe centerline. These electrodes straddle the beam along each axis and are located equidistant from the drift centerline. The signal in each electrode is proportional to the beam current and inversely proportional to the distance of separation from the beam. The measured signal can be made to contain only positional dependence by taking the ratio of the difference and sum of measured magnetic fields along an axis. The signal from each stripline pickup is digitally processed and displayed graphically on a monitor. This real-time position data can be displayed in two formats. The first displays the beam position at a selected location. The graphic display includes a dot to represent the electron beam position and a set of cartesian coordinates are used to reference the beam pipe centerline.

The second display format simultaneously shows the electron beam position at all four diagnostics stations along both the horizontal and vertical axes.

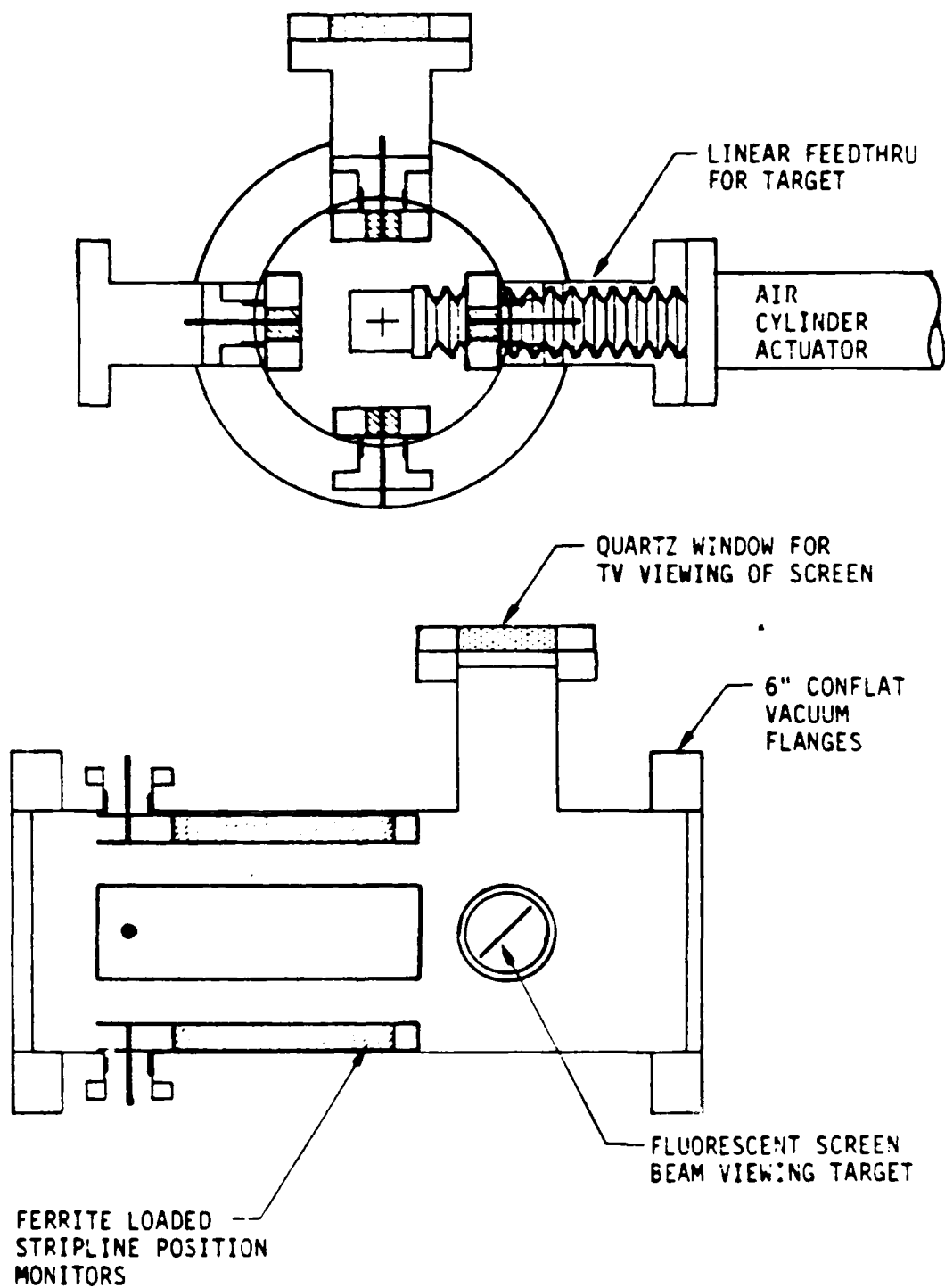


Figure 1.3-2  
BEAMLINE POSITION MONITOR AND VIEWSCREEN

## REFERENCES

- 1.1.1 M. B. James and R. H. Miller, A High Current Injector for The Proposed SLAC Linear Collider, 1981 Particle Accelerator Conference, Wash., D.C., March 11-13, 1981, p. 3461.
- 1.1.2 G. Mavrogenes, et al., "Subnanosecond High Intensity Beam Pulse," IEEE Trans. Nuc. Sci. NS-20, 919 (1973).
- 1.1.3 J. E. Clendinin, et al., Beam Parameter Measurements for the SLAC Linear Collider, SLAC Pub 2828, 1981 Linac Conf, Santa Fe, Oct. 1981.
- 1.1.4 P. K. Tein et al., Proc. IRE 43, 260 (1955).
- 1.1.5 M. MacGregor and C. B. Williams, IEEE Trans. Nuc. Sci. NS-14, 581, (1967), G W. Peterson & W. J. Gallagher, IEEE Trans. Nuc. Sci. NS-16, 214 (1969).
- 1.1.6 J. Haimson, High Current Traveling Wave Electron Linear Accelerators, IEEE Trans. Nuc. Sc. June 1965 p. 996.
- 1.2.1 CIRCUS-2: A Digital Computer Program for Transient Analysis of Electronic Circuits. B. Dembart and L. Millman, Boeing Report 0062-1 (1973).
- 1.3.1 K. L. Brown, F. Rothacker, D. C. Carby, Ch. Iselin, TRANSPORT: A computer program for Designing Charged Particle Beam Transport Systems, SLAC-91 RBX-2 (May 1977).
- 1.3.2 D. C. Carby, TURBLE: A Computer Program for Simulating Charged Particle Beam Transport Systems, NAL-64 (May 1978).



**END**

**FILMED**

**1-83**

**DTIC**